6-2018

Efficient Organic Photovoltaic Cells Employing Squaraines and Their Aggregates: Experiment and Theory

Chenyu Zheng
cxz9423@rit.edu

R·I·T

Efficient Organic Photovoltaic Cells Employing Squaraines and Their Aggregates: Experiment and Theory

by

Chenyu Zheng

A dissertation submitted in partial fulfillment of the requirements
for the degree of Doctorate of Philosophy in Microsystems Engineering

Microsystems Engineering Program
Kate Gleason College of Engineering

Rochester Institute of Technology
Rochester, New York
June 2018

Efficient Organic Photovoltaic Cells Employing Squaraines and Their Aggregates: Experiment and Theory
by
Chenyu Zheng

Committee Approval:

We, the undersigned committee members, certify that we have advised and/or supervised the candidate on the work described in this dissertation. We further certify that we have reviewed the dissertation manuscript and approve it in partial fulfillment of the requirements of the degree of Doctor of Philosophy in Microsystems Engineering.

_____

Dr. Christopher J. Collison (Thesis advisor) Date
Professor, School of Chemistry and Materials Science, RIT

_____

Dr. Jeremy A. Cody Date
Associate Professor, School of Chemistry and Materials Science, RIT

_____

Dr. Jiandi Wan Date
Assistant Professor, Microsystems Engineering, RIT

_____

Dr. David W. McCamant Date
Associate Professor, Department of Chemistry, University of Rochester

Certified by:

_____

Dr. Bruce Smith Date
Director, Microsystems Engineering Program

ABSTRACT

Kate Gleason College of Engineering
Rochester Institute of Technology

Degree: Doctor of Philosophy **Program**: Microsystems Engineering

Authors Name: Chenyu Zheng

Advisors Name: Christopher J. Collison

Dissertation Title: Efficient Organic Photovoltaic Cells Employing Squaraines and Their Aggregates: Experiment and Theory

Organic photovoltaics (OPVs) have continued to attract attention over the past two decades, promising solution processable and aesthetically pleasing solar energy harvesting devices. The power conversion efficiency of OPV has improved rapidly owing to the development of novel conjugated polymers and functional molecules. Recently, donor-acceptor push-pull type materials have been investigated ubiquitously for OPV applications due to their high extinction coefficients in the near-infrared region of the solar spectrum. At RIT, a series of donor-acceptor-donor type squaraine (SQ) materials have been systematically synthesized and investigated for their potential in bulk heterojunction (BHJ) OPV devices. This dissertation presents both experimental and theoretical work associated with these squaraines.

In the first part, the dependence of solar cell performance on BHJ morphology is discussed, with the emphasis on how SQ aggregation dominates the morphological behavior of the BHJ upon spin coating and post annealing treatments. SQ aggregates in the BHJ films represents crystalline domains which should benefit the charge transport toward the electrodes. At the same time, SQ aggregation induces phase separation and leads to

formation of large SQ or PCBM domains. Domain size is a critical factor determining the solar cell efficiency as the exciton diffusion length in SQ films is believed to be small. The extent of phase separation can be controlled through varying SQ:PCBM weight ratio; a more homogeneously mixed BHJ morphology is obtained when PCBM content is high, leading to an improved solar cell efficiency. Film crystallinity and SQ aggregation is disrupted at high PCBM weight ratio but can be recovered via thermal annealing. Controlling the tradeoff between crystallinity and phase separation of the BHJ is identified as critical for device optimization of SQ-based solar cells. In addition, different SQ molecules have been comparatively investigated to reveal the correlation between the molecular structure and the aggregation properties. In this way, this dissertation connects SQ structure to aggregation properties, then to BHJ morphology and finally to OPV performance.

The second half of this dissertation focuses on using an essential state model to fully understand the intermolecular interactions within the SQ aggregates. The model has been constructed based on three main charge resonant structures associated with the zwitterionic nature of the SQ conjugation backbone. Molecular aggregates of the SQ chromophores were built based on the experimentally obtained single crystal structures. Specifically, we found that, in as-cast BHJ films, the SQ-SQ interaction is dominated by Coulombic coupling (CC) while in annealed BHJ films the intermolecular charge transfer (ICT) strongly influences the electronic properties. The type of aggregation is shown to greatly influence the solar cell performance. Specifically, CC-aggregates formed in the as cast films yield better solar cell efficiency as compared to ICT-coupled aggregates (which is of higher ordered and more crystalline).

Finally, the sub-picosecond transient absorption spectroscopy results reveal how the excitons in the CC-aggregates are highly mobile, which rationalizes the high solar cell efficiency obtained from such aggregates.

ACKNOWLEDGEMENTS

This dissertation would not have been possible without the enormous supports from my collaborators, colleagues, family and friends. First, I would like to thank my advisor, Dr. Christopher Collison, for his continuous enthusiasm, encouragement, guidance and supports during my PhD researches at RIT. His critical questions always stimulated me towards deeper understanding and encouraged me to hold high standards and expectations of myself. I also thank my committee members, Dr. Jeremy Cody, Dr. David McCamant and Dr. Jiandi Wan for their investments in my academic development. I am very fortunate to work and collaborate with each of them in different projects.

I would like to thank my collaborators: Dr. Frank Spano, Dr. Nicholas Hestand and Chuwei Zhong at Temple University, Michael Mark at University of Rochester, and Dr. Rafael Verduzco and Zhiqi Hu at Rice University for many positive and fruitful interactions which helped move this dissertation forward. I would also like to acknowledge Dr. Scott Misture at Alfred University, Dr. Michael Pierce, Dr. Richard Hailstone, Dr. Matthew Lynn, Dr. Anju Gupta and Dr. Seth Hubbard at RIT for their help on various experiments presented in my dissertation.

I would like to acknowledge the former and current group members of the Collison OPV group at RIT: Dr. Susan Spencer, Anirudh Raju Penmatcha, Guy Wolfe II, Ishita Jalan, James Sinka, Daniel Saviola, Kenny Baptise, Elias Oakes, Jean Li, Yaxin Zhang, Zhila Hooshangi, and Soumya Gupta. I thank my friends at RIT: Dr. Yuanhao Zhang, Xinye Chen, Sitong Zhou, Cheng Liu and Dr. Xiang Li for their joyful company. I also thank Dr. Chu Chang at RIT for her trust in me when I first came to U.S. and many warm and delightful conversations.

Finally, I would like to express my gratitude to my family members: my mom Rongping Han, my dad Qi Zheng, and my wife Jingjing Shu for their whole-heart support during my doctoral studies. In this regard, I would like to express my deepest gratitude to my wife.

TABLE OF CONTENTS

LIST OF TABLES

LIST OF FIGURES

Chapter 1. GENERAL INTRODUCTION

The concept of using organic semiconducting materials in photovoltaics, i.e. organic photovoltaic (OPVs), was first brought up as a less expensive alternative to silicon-based solar cells. The scientific curiosity quickly grew as OPV relies on plastic materials, such as polymers, and with its seemingly unlimited material resources, and easy manufacturing processes. The first efficient organic photovoltaic cells, with 1% efficiency (under simulated AM2 illumination) were demonstrated in 1986 by Ching W. Tang at Eastman Kodak Co. in Rochester, New York.[1] The cell was constructed by bringing two layers of organic semiconductors in contact to form a "bi-layer" heterojunction. Excitons generated in each layer can be efficiently dissociated at the junction interface, leading to a significant increase in photon-to-electron conversion efficiency as compared to solar cells with a single layer. In 1992, Heeger and Wudl *et. al.* reported an observation of photoinduced electron transfer from Poly[2-methoxy-5-(2-ethylhexyloxy)-1,4-phenylenevinylene] (MEH-PPV) to buckminsterfullerene (C_{60}).[2] A year later, they demonstrated that the charge transfer from polymer to fullerene occurs on a femtosecond time scale, faster than any other competing processes.[3] The result of this is a theoretical promise that the photoinduced charge generation can be achieved with up to a 100% quantum efficiency. This discovery has led to the opening of an energetic/enthusiastic research field of OPVs.

Various outstanding properties of OPV have been recognized. For example, large OPV modules can be manufactured through roll-to-roll printing techniques.[4,5] This allows OPV devices to have small CO_2 footprints, fast industrial throughput and cheap manufacturing cost. The flexibility and lightweight of OPVs allow the large solar panels to be easily transported or installed.[6] The transparency of OPV enables the inventions of solar cell

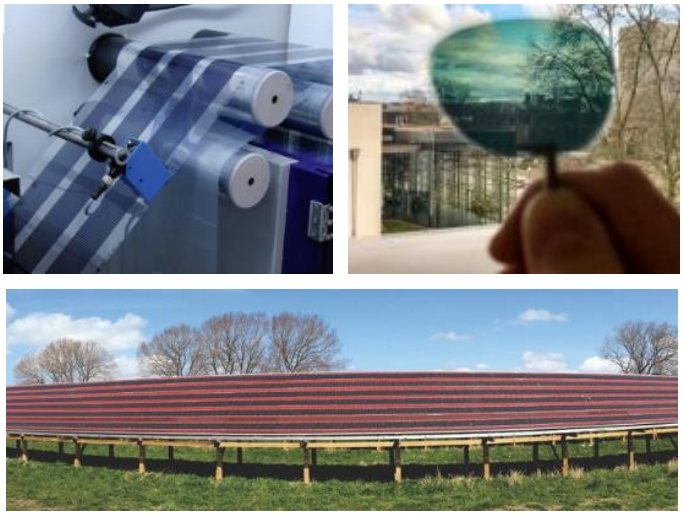

Figure 1.1. Demonstrations of organic photovoltaic (OPV) cells. Flexible OPV cells manufactured by roll-to-roll coating (top left), from reference 4. A solar glasses lens made from OPV cells (top right), from reference 7. A row of 100-meter-long OPV solar panels installed on a wooden frame (bottom), from reference 5.

glasses[7] and windows[8], which selectively convert non-visible light into electricity. In addition, an improved performance of OPV devices has been observed under LED light. As compared to using sunlight as the source, the OPV cells show a large increase in efficiency by up to 350% when shone under the indoor LED light bulb, leading to a power conversion efficiency exceeding that of crystalline silicon cells.[9] This remarkable efficiency improvement is attributed to better spectral overlap between the artificial light source and absorbance of the materials.

The performance of OPV cells has been continually improved by using novel materials[10–12], refining fabrication processes[13–15] and advancing device structures[16]. Nevertheless, the OPV efficiency is still low, rendering a high cost for the power it generates. Thus, improving the efficiency of the OPV devices remains as one of the top interests for many research groups. The lifetime of the solar cell products is also a critical aspect to evaluate the cost-effectiveness of OPV.[17] Longer operating time allows more

power to be generated during the life-cycle of the solar cells. Another important research direction is to enable fabrication of OPV cells through non-toxic ink vehicles. In summary, in order to reach the commercialization requirements, OPV products need to have high efficiencies with practical stability, and can be realized by solution processes in non-toxic ink.[18]

1.1 A Brief Description of the Principles of OPVs

The process of photoinduced charge generation in OPV cells can be separated into five steps; 1) photon absorbance, 2) exciton diffusion, 3) charge dissociation, 4) charge transport and 5) charge collection (Figure 1.2).

Upon absorbance of a photon, an electron in the ground state of the absorbing molecule is excited to a higher unoccupied molecular orbital forming a higher energy state in the molecule. This process is also described as the creation of a bound electron-hole pair, or an *exciton*. Unlike the Wannier-Mott excitons generated in the inorganic semiconductors, the Frenkel exciton produced in organic semiconductors has a binding energy that is significantly larger than the thermal energy at room temperature, in the range of 0.2 ~ 1 eV.[19] Thus, without a proper separation strategy, these excitons will eventually decay back via radiative or non-radiative pathways. To overcome this binding energy, two types of organic material with different highest occupied molecular orbitals (HOMO) and different lowest unoccupied molecular orbitals (LUMO) are mixed to form donor-acceptor heterojunctions. At the interface of these materials, the electron in the LUMO of the donor (in the excited state) can "hop" to the LUMO of the acceptor due to an energy offset, while the hole remains at the highest occupied molecular orbital (HOMO) of the donor. Hence,

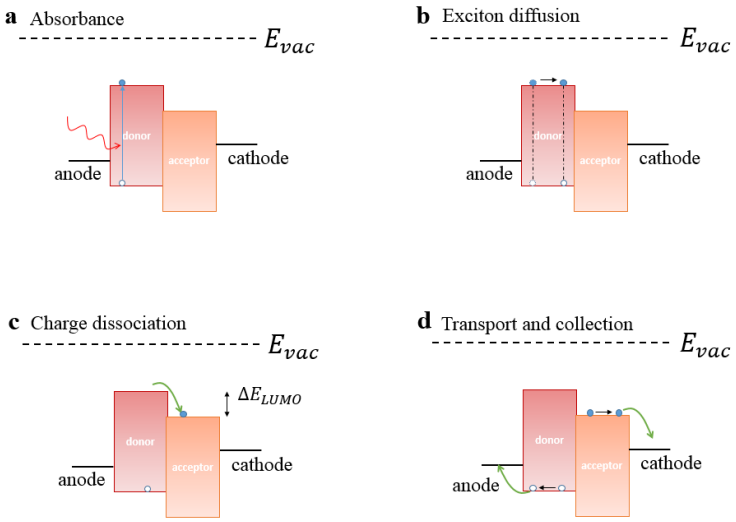

Figure 1.2 Schematic diagram illustrating the five main steps for photo-charge generation mechanisms in an organic photovoltaic cell. a) Step 1, absorbance of a photon and generation of an exciton, b) step 2, exciton diffusion to the heterojunction, c) step 3, charge dissociation at the interface, d) step 4, charge transport in the pure domains and step 5, charge collection by the electrodes.

the originally bound electron and hole are now spatially separated. Then, the electrons (and holes) transport through the continuous phases/domains of acceptors (and donors) and are eventually collected by the corresponding electrode.

The external quantum efficiency (EQE) – a ratio between the number of electrons produced by and the number of photons incident on the solar cell device at the steady state of the organic solar cells is determined by the product of the individual efficiencies for each step:

$$\eta_{EQE} = \eta_{ABS} \cdot \eta_{ED} \cdot \eta_{CD} \cdot \eta_{CT} \cdot \eta_{CC} \tag{1.1}$$

The absorbance efficiency, η_{ABS}, represents the number of photons that the solar cell can absorb versus the total number of photons that it received from the solar irradiation. It is influenced by two factors: absorbance bandwidth and absorptivity. The former can be

expressed as the wavelength range over which the active materials can absorb, and the latter indicates the probability of absorbance of a photon by the molecule at each wavelength. Organic dye materials normally have a high absorptivity (typically 10^4~10^5 cm^{-1}), so it only needs a small amount of material to absorb most photons in the active wavelength range. For efficient OPV devices, the organic layer can be as thin as ~100 nm. However, these materials typically have a narrow absorbance bandwidth. For widely investigated Poly(3-hexylthiophene-2,5-diyl) (P3HT) and [6,6]-phenyl-C61 butyric acid methyl ester (PCBM) bulk heterojunction solar cells, the absorbance of the materials covers a spectrum roughly from 300 nm to 650 nm. Thus, most of the photons emitted from the sun are lost.[20,21] Many efforts, therefore, have been directed to stacking multiple layers (i.e. organic tandem solar cell) or blend more than two types of functional materials with complementary absorbance spectra (i.e. organic ternary or quaternary solar cells) for more efficient photon harvesting.

The exciton diffusion quantum efficiency, η_{ED}, represents the efficiency for the exciton to successfully diffuse to the heterojunction interface before it decays back to the ground state. Exciton diffusion length (L_D), is a contributing factor for η_{ED} of organic semiconductors. L_D is defined as the average distance that the exciton can move in a neat bulk material before it is spontaneously deactivated. The relationship between L_D and η_{ED} can be expressed by:[20]

$$\eta_{ED} = e^{-d/L_D} \tag{1.2}$$

where d is the distance between the exciton and the nearest interface. Equation (1.2) holds under the assumption that the exciton movement is a random walk with a constant step size (equal to the distance between molecules) and is not affected by the electric field (we

consider the exciton to be charge-neutral). Thus, the exciton diffusion quantum efficiency, η_{ED}, depends exponentially on the ratio of d/L_D. A general equation calculating the exciton diffusion length, L_D, is given as:[22]

$$L_D = \sqrt{2aD\tau} \tag{1.3}$$

where a represents the dimensionality of the diffusion, $a = 3$ for three-dimensional exciton diffusion; D is the diffusion coefficient of the exciton; τ is the exciton lifetime. The exciton lifetime of organic semiconductors is generally short, typically on a pico-to-nanosecond scale and the L_D for organic semiconductors is typically measured to be on the order of 1~10 nm.[23–25] For the exciton diffusion coefficient, one would expect it to be larger in a crystalline material than in that same material's amorphous state. This is true for several materials, such as 3,4,9,10-perylenetetracarboxylic dianhydride (PTCDA),[24,26] perylene derivatives[27] and diketopyrrolopyrrole (DPP)-based molecules[23]. However, the exciton diffusion mechanism could be more complicated. For example, Siebbeles *et al.* have found that the molecular orientation in the crystal structure strongly influences the exciton diffusion length for phthalocyanine and porphyrin derivatives.[28] Hestand *et al.* reported that the exciton diffusion dynamics can be significantly altered in 7,8,15,16-tetraazaterrylene (TAT) nanopillars if the slip stack distance is only shifted by 0.5 Å.[29] Holmes *et. al.* reported, quite counterintuitively, an enhanced exciton diffusion in boron subphthalocyanine chloride (SubPc) by diluting this material with an inert host molecule to break the formation of SubPc crystallites.[30] These studies imply that the exciton diffusion dynamics does not only relate to the crystallinity of the material, but also is strongly dictated by the molecular orientation and packing geometries, which might be specific to each individual molecule and structure.

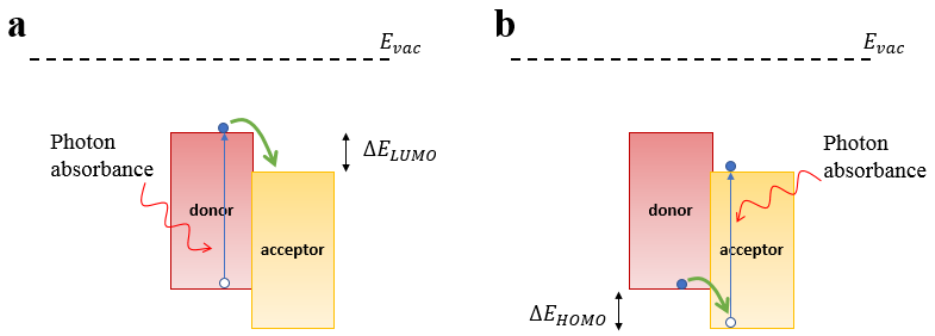

Figure 1.3 illustration of charge dissociation mechanisms at the donor-acceptor interface when exciton is located on a) donor and b) acceptor. When donor is excited, the electron is transferred between LUMO levels; when acceptor is excited, the electron is transferred between HOMO levels. The energy drives the charge dissociation is ΔE_{LUMO} and ΔE_{HOMO} in **a**) and **b**).

Charge dissociation is the step for solar cells to convert the neutral exciton into free charges. For this step, there are two scenarios, as illustrated in Figure 1.3. When an exciton is formed on the donor molecule, the excited electron on the LUMO of donor can hop over to the LUMO of the acceptor with the aid of the energy offset, ΔE_{LUMO}. When an exciton is generated on the acceptor molecule, a hole is formed on the HOMO of the acceptor, which is then filled by an electron hopping from the donor HOMO, driven by ΔE_{HOMO}. These two cases result in the same outcome; the electron is located on the LUMO of acceptor and the hole is located on the HOMO of the donor. Generally, an energy offset of 0.2-0.5 eV is required to get an efficient charge dissociation.[31] This energy loss is inevitable in order to overcome the electron-hole binding energy of the excitons. Thus, for efficient charge dissociation efficiency, η_{CD}, the LUMOs and HOMOs of the donor and acceptor need to be regulated to the appropriate levels.

In the charge transport step, the dissociated charges move through continuous donor or acceptor domains towards the corresponding electrode. The transport of electrons

(holes) is enabled via the overlap of frontier molecular orbitals between the two adjacent acceptors (donors). Before the charges are collected by the electrode, there are two possible pathways for them to recombine: monomolecular and bimolecular recombination, both of which result in electronic energy loss and deviate η_{CT} from 1.[32]

Monomolecular recombination is a first order process (the order of the process is characterized by the light-intensity-dependent current-voltage tests) and often refers to geminate recombination and Shockley-Read-Hall recombination. Geminate recombination is when the initially generated electron recombines with the hole it was born with. It is not the major recombination loss in efficient solar cells where donor and acceptor are chosen with apposite energy levels.[33–36] For Shockley-Read-Hall recombination, electron and hole recombine through a trap state formed by material impurities or incomplete phase separation (e.g. single donor molecule is surrounded by acceptors). The trap site quickly captures the initial charge, for example a hole, and creates a positive stationary electric field to attract nearby mobile electrons in the active layer. The rate of monomolecular recombination is thus determined by the density of the traps (independent of incident light intensity), n_{trap}, and the density of mobile charges in the active layer (dependent of incident light intensity), $n_{e-/h+}(I)$:[32]

$$k_{mo} \propto n_{trap} \cdot n_{e-/h+}(I) \tag{1.4}$$

Hence, the rate constant of monomolecular recombination is proportional to the light intensity to the first order ($k_{mo} \propto I$).

On the other hand, bimolecular recombination refers to the case when the mobile holes and electrons collide into each other during the charge transport step and eventually recombine before they are able to escape from the coulombic force. The recombination rate

constant is proportional to the density of positive and negative charge carriers (both dependent on light intensity):

$$k_{bi} \propto n_{e-}(I) \cdot n_{h+}(I) \quad (1.5)$$

Therefore, the rate constant of bimolecular recombination is proportional to the light intensity to the second order ($k_{bi} \propto I^2$). To increase the quantum efficiency of charge transport, one would need to minimize the recombination losses. In particular, the loss of monomolecular recombination can be significantly reduced by improving the bulk heterojunction morphology.[37] As mentioned above, unsatisfying morphology, such as an isolated donor surrounded by acceptors, can cause the formation of traps.[33,37]

The last step of the photo-charge generation process is charge collection. The two electrodes collecting charges have different work functions. The electrons generated in the organic bulk move towards the lower work function electrode, such as aluminum or calcium, while the holes move towards the higher work function electrode, such as silver or gold. Indium tin oxide (ITO) is a transparent electrode that does not block the light, and thus is used in conjunction with one of the metal choices mentioned above. This metal oxide material has a moderate work function of 4.4 - 4.5 eV [38], allowing it to be used as either a hole-collecting or an electron-collecting electrode. For better charge extraction/collection efficiency, a buffer layer is often used in between the heterojunction layer and the metal or metal oxide electrode. Tris(8-hydroxyquinolinato) aluminium,[39] Bathocuproine,[40,41] Bathophenanthroline,[42] LiF [43] and ZnO [44,45] are effective cathodic buffer layer materials, and poly(3,4-ethylenedioxythiophene) polystyrene sulfonate (PEDOT:PSS),[11] MoO_3 [46,47] and V_2O_5 [48,49] are often used as the anodic buffer layers. The benefits of these buffer layers includes: 1) providing ohmic contact between the active

layer and the electrode to reduce the charge accumulation at the metal/organic interface; 2) blocking excitons from reaching the electrode to prevent exciton quenching; 3) smoothing the electrode surface to improve the active layer morphology and structure.

Overall PCE will suffer if any one of the five steps is inefficient (Equation (1.1)). Thus, efforts have been driven towards improving the efficiencies of all the steps at the same time to maximize the OPV efficiency.

1.2 Fabrication and Testing of OPVs

Most efficient OPV devices are fabricated in the lab using vacuum thermal evaporation (VTE) or spin cast. The former method is mainly used for small molecule OPV device due to the ease of sublimation of small molecules. In this method, C_{60} and C_{70} are almost exclusively used as the acceptor material for their distinctly high exciton diffusion length and appropriate energy levels. VTE has some advantages; 1) the materials are processed in high vacuum, limiting the exposure to oxygen and moisture, and thus, the material degradation is minimized; 2) the resulting film is generally uniform and of high quality and 3) the growth of the layer can be well controlled in terms of film thickness, material composition, etc., and the interface between each layer is well defined. The VTE method can also be easily tuned to make tandem solar cells because the evaporation of the top-cell material has little effect on the bottom layers.[16,50,51]

For solution processes, the spin cast method is mainly used for polymer-based OPV cells fabricated in the lab. Small molecule active layers can also be processed via spin casting, yielding a uniform film with high device efficiency.[11] PCBM and [6,6]-Phenyl-C71-butyric acid methyl ester ($PC_{71}BM$) are frequently used as acceptors in solution

processed BHJ solar cells. These fullerene derivatives are functionalized C_{60} or C_{70}, to enable a good solubility in common organic solvents without sacrificing exciton and charge mobility in the spin cast films. Recently, many new non-fullerene acceptors have been developed and efficient BHJ solar cells are achieved with such acceptors.[52] The solution process is more relevant to the future of large-scale manufacture of OPV panels. Solution processing can be up-scaled to industrial roll-to-roll techniques, such as doctor blading, ink-jet printing and slot-die coating.[4]

OPV device efficiency can be measured using two techniques, the current-voltage (J-V) test and the spectral response test. The J-V test measures the current-voltage behavior of the device, delivering the power conversion efficiency (PCE) of the solar cell. Ideally, the solar cell should be tested against actual solar irradiation. A more practical method to test devices in the lab employs a solar simulator with an optical filter to mimic the solar spectrum after it penetrates through the air around the globe (air mass 1.5 G). The solar simulator is calibrated to have an intensity of 100 mW cm^{-2} (i.e. a 1-sun illumination intensity). Other irradiation intensities can be used to investigate the device properties, such as recombination, which is proportional to that intensity, as described above. In testing the solar cell, a voltage sweep is applied to the cathode and anode of the solar cell, and the current is sensed and measured by a source meter.

A typical J-V curve of an organic solar cell device is shown in Figure 1.4. The three metrics determining the efficiency are the short circuit current density (J_{sc}), the open circuit voltage (V_{oc}) and the fill factor (FF). J_{sc} is the current density produced by the device at zero external bias under illumination; V_{oc} is the maximum voltage that the solar cell can output, when no current is drawn. The solar cell achieves its highest efficiency at the

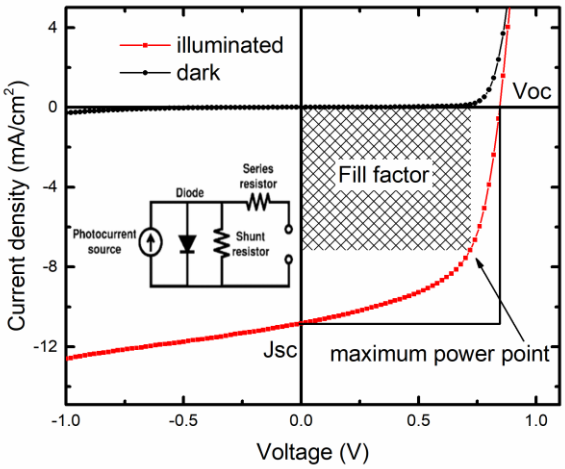

Figure 1.4 A typical current-voltage test result of an organic photovoltaic device when measured without (black) and with (red) illumination. The fill factor is the ratio between the maximum power point and the product of short-circuit current, J_{SC}, and open-circuit voltage, V_{OC}. The inset shows an equivalent circuit of an OPV cell – the current source in parallel with a diode and a shunt resistor; a series resistor is also added to account any loss in current due to the resistance of the devices.

maximum power point (MPP) as shown in the Figure 1.4. The FF is the ratio between maximum power point and the product of J_{sc} and V_{oc}. The power conversion efficiency (PCE) is calculated as:

$$PCE = \frac{J_{sc} \times V_{oc} \times FF}{P_{in}} \tag{1.6}$$

where P_{in} is the power of incident light (100 mW cm^{-2} for 1-sun illumination).

An equivalent circuit diagram for OPV device is drawn in inset of Figure 1.4. The cell acts as a photocurrent source with an ideal diode in parallel, and a series resistor (R_s) and a shunt resistor (R_{sh}).[53,54] For an ideal solar cell, R_s is zero while R_{sh} is approaching infinity. In this case, the photocurrent in the first quadrant in Figure 1.4 should be a "steep" vertical line as the external bias favors the current flowing in a forward direction through the diode (and not through the shunt resistor). The photocurrent in the third quadrant, on

the other hand, should be a "flat" line with the values equal to J_{sc} since the external bias leads to the current flowing through the shunt resistor. Most organic solar cells deviate from the ideal case, with the current curve in the first quadrant taking a slope of V/R_s, and the curve in the third quadrant taking a larger value than J_{sc} by the amount of V/R_{sh}. The overall J-V curve can be a modeled through modified diode equation[53]:

$$J = J_{ph} - J_s \left[\exp\left(\frac{q(V - JR_s)}{nk_BT} - 1 \right) + \frac{V - JR_s}{R_{sh}} \right] \tag{1.7}$$

where J is the current density, V is the external voltage, J_{ph} is the photo-generated current density, J_s is the reverse saturation current density, q is elementary charge, n is the ideality factor of the diode, k_B is the Boltzmann constant, and T is the temperature. For the ideal case ($R_{sh} \to \infty$ and $R_s \approx 0$), Equation (1.7) is reduced to an ideal diode equation plus a photocurrent density, J_{ph}.

Another method to evaluate solar cell performance is the spectral response test, which measures the solar cell photosensitivity at each specific wavelength. This test generates a spectrum of external quantum efficiency (EQE). The number of electrons is calculated from the measured current density, while the number of incident photons is calculated based on the power of the incident beam and the photon energy. For the instrumental set up, a light monochromator is used in between the light source and the solar cell; a beam chopper and a lock-in amplifier is used to optimize the signal-to-noise ratio.

A typical EQE spectrum of a squaraine (SQ)-PCBM organic solar cell is shown in Figure 1.5 along with the absorbance spectra. Since the photoactive materials are generally absorbing at different regions, the EQE spectra can yield information about the

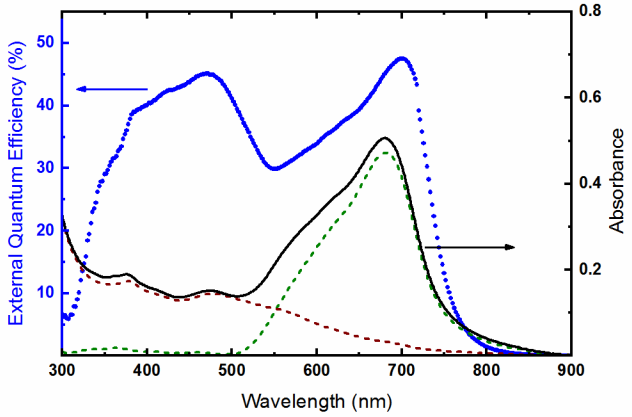

Figure 1.5 A typical external quantum efficiency (EQE) spectrum (blue dots) of a squaraine-PCBM organic solar cell. Also shown is the absorbance spectra of the bulk heterojunction (BHJ) film (black line), of the squaraine (green dashed line) and of the PCBM film (brown dashed line). The absorbance spectra of BHJ film and PCBM neat film are experimentally obtained from the films, while the difference between the two qualitatively produces the absorbance spectra of squaraine. Note that the absorbance spectra of squaraine neat film is different from the real absorbance of squaraine in the BHJ film, in which squaraine molecules are less aggregated.

performance of each individual component. From Figure 1.5 we see that the absorbance of PCBM is lower than that of SQ. The EQE of the PCBM at the region of 300 – 500 nm, nevertheless, is comparable to that of the SQ at the region of 600 – 800 nm. This indicates that PCBM might be more efficient in exciton diffusion (η_{ED}), charge dissociation (η_{CD}) and charge transfer (η_{CT}). For tests measured under the short circuit condition, integration of the EQE over the entire solar electromagnetic spectrum will yield the current density that approximately equals the short circuit current density (Jsc) measured from the J-V characterization.

1.3 Basic Device Physics of OPVs

1.3.1 Guidelines for interpreting the J-V curve of OPVs

The J-V test is the most commonly used method to measure the efficiency of OPV devices. It yields three important parameters: short circuit current density (Jsc), open circuit voltage (Voc) and fill factor (FF). These three parameters cannot be used to draw any mechanistic conclusions by themselves as these parameters are the outcome of many complexities. To investigate the solar cell as a function of a given property, we usually discuss the trend in Jsc, Voc and FF, in comparison to a reference device (to limit the influencing variables) or combine the results from J-V measurements and the results from other characterization techniques.

Short circuit current density. Changes in Jsc can be related to the changes in absorbance of the materials, which might result from the difference in layer thickness, use of additional absorbers or absorbing layers, use of materials with different photoactive spectrum and morphology induced absorbance change. For example, the NIR absorbing materials, such as squaraines, are considered to have higher Jsc than P3HT, given that the solar irradiation spectrum has more photons in the NIR region (600 – 800 nm) than in the 400-600 nm (where P3HT absorbs). Squaraine makes another good example of morphology-induced absorbance change, as its aggregates feature a much broader absorbance spectrum in the films, which is beneficial to achieve higher absorbance efficiency. The material absorbance spectra and EQE spectra are often measured to gain insights into the η_{ABS} of the solar cells.

The Jsc can also be affected by the efficiency of exciton diffusion (η_{ED}) and charge

transport (η_{CT}), which may both be affected by changes in morphology/crystallinity of the film. As mentioned above, the exciton diffusion length is sensitive to the material crystal structure. Generally, larger L_D is expected in crystalline structures as compared to the amorphous, randomly distributed material domains.[23,25] Thus, thin film X-ray diffraction measurements are often used to study the change in the film crystallinity and thus to infer the trend of exciton diffusion efficiency of the solar cell.[40] Another important factor affecting both η_{ED} and η_{CT} is the domain size. When domain size is much larger than the exciton diffusion length, η_{ED} would suffer. η_{CT}, on the other hand, is high since charges transport more directly in pure domains than the tortuous pathway transport for mixed phases. Domains in a BHJ film can be observed under a transmission electron microscope.[55]

Saturation photocurrent density. Saturation photocurrent density is another important parameter which is often used to compare with Jsc. At the reverse external bias (i.e. the third quadrant in Figure 1.4), voltage favors the charge flow direction of the solar cell. In such favorable external field, the charge recombination probability in the BHJ films is reduced, leading to a photocurrent density that is larger than Jsc. As illustrated by the voltage-current curve in Figure 1.4, the photocurrent density at -1 V (i.e. 12.6 mA cm^{-2}) is higher than the Jsc (i.e. 10.8 mA cm^{-2}). This increase in photocurrent will be saturated at a sufficiently high reverse bias (usually at -2 ~ -3 V), and the photocurrent at this voltage is called the saturation photocurrent. On the other hand, a high reverse external bias might break the diode behavior of the solar cell, causing a current leakage (i.e. significant charge injection from the external sources into the solar cell due to the small R_{sh}). Current leakage can make a non-negligible contribution to the saturation photocurrent density. Thus, the

saturation photocurrent is always obtained by subtracting the dark current from the measured solar cell photocurrent.

Open circuit voltage. Voc is the maximum voltage that a solar cell can produce. It can also be viewed as the applied voltage at which all photogenerated charges are recombined within the BHJ. Voc is largely influenced by the interface energy gap between the donor and acceptor (E^{DA}), more specifically, the energy of donor HOMO and the acceptor LUMO. Brabec *et al.* have studied BHJ solar cells with MDMO-PPV as the donor and each of different fullerene derivatives (with various LUMO energy levels) as the acceptor, and they have found a roughly 0.3 eV difference between the Voc and the E^{DA}.[56] This "missing" 0.3 eV has been observed for many other donor acceptor systems.[57–60]

$$V_{OC} = \frac{1}{e}\left(E_{LUMO}^{acceptor} - E_{HOMO}^{donor} - \Delta\right) - \frac{kT}{e}\ln\left(\frac{n_e n_h}{N_c^2}\right) \tag{1.8}$$

where n_e and n_h are electron and hole densities on the acceptor and donor domains respectively, N_c is the density of states at the edge of the bands and Δ represents the energy shift of the HOMOs and LUMOs, which originates from the disorder in the phase separated BHJ. Note that the charge densities, n_e and n_h, are proportional to the intensity of incident light. Thus, Voc depends logarithmically on the power of incident light.[32]

Fill factor. Fill factor (FF) measures the photocurrent loss due to the voltage at the "power generating quadrant", and it is the ratio between the product of current density (J_{mpp}) and voltage (V_{mpp}) at the maximum power point and the product of the short circuit current density and open circuit voltage,

$$FF = \frac{J_{mpp} \times V_{mpp}}{J_{sc} \times V_{oc}} \tag{1.9}$$

It is very sensitive to the charge recombination of the devices. For solar cells with high charge recombination probability, the loss of photocurrent would be aggravated by the unfavorable/forward external voltage at the fourth quadrant (Figure 1.4), leading to a low FF. The low or imbalanced charge mobilities would also reduce FF due to the difficulties extracting and collecting low-mobility charges at forward bias.

1.3.2 Exciton diffusion and Förster resonant energy transfer

The local electronic excited state in organic semiconductors can induce a deformation of the conjugation units, leading to a change in bond length, i.e. stretching of the double bond and shortening of single bonds. This is referred to the electron-phonon coupling. For conjugated polymers, the nuclear rearrangement is at the greatest degree at the center of the exciton and gradually weakens for the units further away from the exciton. Such an exciton can be more accurately named as a Frenkel exciton,[61] but for simplicity, we will keep the term *exciton* as the description of excitation energy in organic materials. For poly(phenylenevinylene) (PPV) polymers, the Frenkel polaron/exciton is reported to spread over around 6 monomer units.[62] Efficient solar cell efficiency relies on the successful diffusion of the exciton to the donor/acceptor interface. It has been reported that when the polymer chain is perfectly conjugated or when small molecules are perfectly crystalized, the exciton can move coherently along the chain or crystallites, which is considered the fastest mechanism for energy transfer in the organic materials.[63] Of course, the local deformations, e.g. bond bending, twisting, etc., of the polymer chains exist ubiquitously in the bulk heterojunction films. These packing defects can terminate the coherent exciton migration along the chain, and therefore exciton diffusion occurs with other transfer mechanisms.

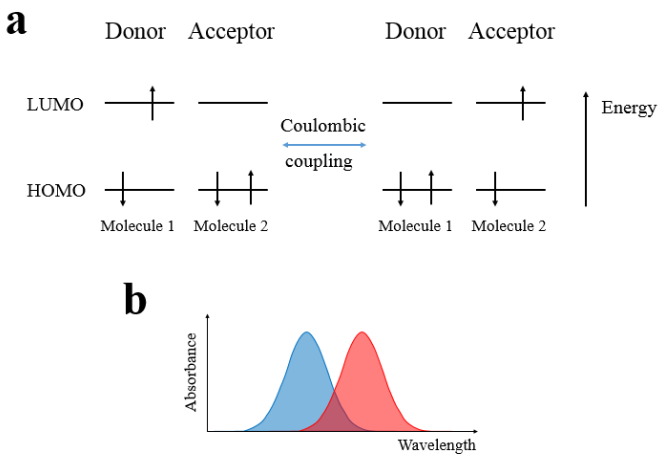

Figure 1.6 Energy level diagram illustrating the Förster resonant energy transfer (FRET) between two identical molecules. (a) Starting with an excitation on molecule 1 (donor), the exciton can transfer to the molecule 2 via Coulombic coupling. (b) The FRET rate constant is proportional to the overlapping area of donor emission and acceptor absorption spectra.

The excitations can diffuse between the polymer chains (or small molecules) through Förster resonant energy transfer (FRET). FRET is a non-radiative transfer process from an energy donor to an energy acceptor via a long-range Coulombic interaction. Note that the "donor" and "acceptor" here refer to the molecules that undergo FRET (and could be the same type of molecules) and should be differentiated from the donor and acceptor materials of BHJ, where charge transfer at the interface between these materials is implied. Although sounding paradoxical, the energy transfer process can be thought of as simultaneous but non-radiative emission of a photon by the donor and subsequent absorbance of that photon by the acceptor (Figure 1.6). The rate of FRET can be calculated as[64]

$$k_{FRET} = \frac{1}{\tau}\left(\frac{R_0}{d}\right)^6 \tag{1.10}$$

where τ is the fluorescence lifetime and d is the distance between the donor and the acceptor. Thus, when $d = R_0$, the rate of FRET equals the radiative rate constant of the

exciton (an equal probability of FRET and exciton relaxation) and R_0 is the Förster radius which is calculated as

$$R_0^6 = \frac{9\eta_{PL}\kappa^2}{128\pi^5 n^4}\int \lambda^4 F_D(\lambda)\sigma_A(\lambda)d\lambda \quad (1.11)$$

Here, κ^2 is the dipole orientation factor, η_{PL} is the photoluminescence quantum yield, and n is the refractive index at the wavelength where the spectral overlap integral is maximized. F_D is the normalized donor fluorescence and σ_A is the normalized acceptor absorbance cross section. Thus the integral represents the spectral overlap between (normalized) donor emission and acceptor absorbance spectra. According to Equation (1.11), FRET cannot take place when the donor is not capable of emitting photons ($\eta_{PL} = 0$). In addition, when dipole orientations are aligned, κ would be increased, and so would the R_0, leading to an efficient FRET.

For molecules or polymer chain units that are sufficiently close to each other in the films, the frontier molecular orbital overlap might be large enough to enable the Dexter energy transfer process.[22] In the Dexter process, the electron on an energy donor LUMO can transfer to the energy acceptor LUMO and the electron on the energy acceptor HOMO can transfer back to the energy donor HOMO. As a result, the excitation energy is transferred from donor to acceptor. Dexter energy transfer can only take place when there is a sufficient molecular orbital overlap. In other words, it only happens when conjugated units are close to each other.

In summary, there are three types of exciton diffusion: migration along the polymer chain (which may involve both Förster and Dexter energy transfer), Förster energy transfer and Dexter energy transfer. The overall diffusion efficiency can be evaluated using Equation (1.2) and Equation (1.3).

1.3.3 Marcus theory for electron transfer at the donor acceptor interface

Charges are generated in organic solar cell devices when the excitons dissociate into electrons and holes at the interface. The dissociation step may occur extremely rapidly, on the order of femtosecond time scale.[3,65] This step can be described by Marcus' theory, as a nonadiabatic electron transfer process.[66]

As shown in Figure 1.7, Marcus theory considers the potential energy surfaces of the initial state, D*/A (where the donor holds an exciton) and the final state D^+/A^- (where the hole is on the donor and the electron is on the acceptor), each as an oscillator parabola in the reaction coordinate, Q. ΔG^0 is defined by the energy difference between the two surfaces' minima. It represents the Gibbs free energy of the electron transfer process. The reorganization energy, λ, describes the energy required to bring the initial state and the surrounding medium to the equilibrium geometry of the final state. The electron transfer happens at the point where the two parabolas intersect, leading to an identification of $\Delta G^\dagger$, which equals the energy difference between the crossing point and the bottom of the initial state free energy parabola. $\Delta G^\dagger$ is also referred to as the *activation energy* that the initial state must acquire (via vibrational motion) in order for the electron transfer to occur. Therefore, the electron transfer rate constant depends on the activation energy via a standard Arrhenius equation,

$$k_{ET} = A\, e^{-\frac{\Delta G^\dagger}{kT}} \tag{1.12}$$

where A is a prefactor and its value should depend on the electronic coupling of the initial and final states. The activation energy, $\Delta G^\dagger$, can be calculated based on the Gibbs free energy, ΔG^0, and the reorganization energy, λ, via

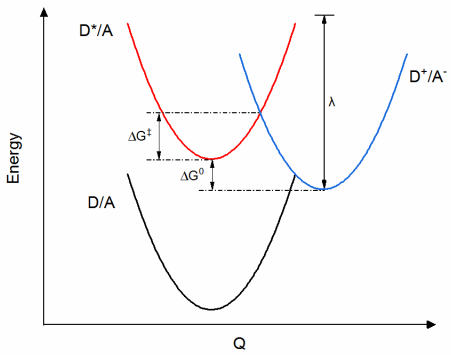

Figure 1.7 Potential energy surfaces for the Marcus theory description of electron transfer process. D/A refers to the ground state donor acceptor, D*/A represents that the donor holds an exciton while D+/A- indicates the generation of an electron on the donor and a hole on the acceptor. $\Delta G^{\dagger}$ is the activation energy, ΔG^{0} is the Gibbs free energy and λ is the reorganization energy.

$$\Delta G^{\dagger} = \frac{(\lambda + \Delta G^{0})^{2}}{4\lambda} \tag{1.13}$$

Thus, the electron transfer rate constant can be further calculated as[67]

$$k_{ET} = \frac{2\pi}{\hbar\sqrt{4\pi\lambda kT}} V_{DA}^{2} e^{-\frac{(\lambda+\Delta G^{0})^{2}}{4\lambda kT}} \tag{1.14}$$

where V_{DA} is the electronic coupling between the initial and final states, and thus depends on the donor and acceptor molecular orbital overlap.[68,69]

For the electron transfer process in organic solar cells, ΔG^{0} is the energy offset between the LUMO (or HOMO) levels of the donor and acceptor at the interface (i.e. ΔE_{LUMO} or ΔE_{HOMO} in Figure 1.3). Equation (1.14) describes that k_{ET} increases as $-\Delta G^{0}$ is increased, until the k_{ET} reaches the maximum at $-\Delta G^{0} = \lambda$. Further increase to $-\Delta G^{0}$ will then actually decrease the electron transfer rate constant. This is referred to the famous *Marcus inverted region*. Recently, Coffey *et al.* have studied the electron transfer rate between a polymer donor and a series of fullerene derivatives with varying energy levels.[31]

They have demonstrated the existence of an optimal energy offset driving the electron transfer at the donor acceptor interface, after which the k_{ET} starts to decrease. This is direct evidence for the applicability of Marcus theory in OPV devices.

1.3.4 Charge mobility and space-charge limited current model

Charge mobility is an important aspect of materials for OPV application. High charge mobility can reduce the probability of bimolecular recombination. It was suggested that a mobility of above 10^{-4} cm^2/Vs is required to achieve high fill factor (>65%) and high photovoltaic performance.[70]

Measurements of charge mobility in neat films or bulk heterojunction films are often done under a space-charge limited condition.[71] In the space-charge limited current (SCLC) regime, the unipolar charges injected from one electrode cannot be sufficiently conducted to the other electrode due to the low charge mobility of the organic materials, leading to a build-up of space charges in the organic bulk which then can diminish the electric field. Then, the amount of charge carrier density saturates and new charges cannot be injected until some charges are extracted from the other electrode. In other words, the current is limited by the transport of charges in the organic film, and the current-voltage characteristics become quadratic. Then the charge mobility can be obtained from the current-voltage measurements via[72]

$$J = \frac{9}{8}\epsilon_0\epsilon_r\mu_{h/e}\frac{(V - V_{bi})^2}{L^3} \tag{1.15}$$

with ϵ_0 the vacuum permittivity, ϵ_r the relative permittivity of the organic material (usually taking a value of ~ 2–4), $\mu_{h/e}$ the mobility of holes/electrons, V_{bi} is the built-in

voltage due to the difference in work functions of the two electrodes and L the thickness of the organic layer.

There are a few conditions that must be achieved in order for the use of SCLC model. First, the device must be unipolar. For measurement of hole mobility, the injection of electrons from any of the electrodes must be blocked. Second, it requires efficient charge injection from the electrode to the organic layer. This is obtained by selecting an electrode material that has a work function aligned well with the HOMO (for hole mobility measurements) or LUMO (for electro mobility measurements) level of the investigated organic material. Third, the current cannot be significantly impacted by the series resistance of the device. In such a case, the current-voltage characteristics would become linear instead of quadratic. Fourth, the difference between the work functions of the two electrodes must be considered. Since the materials of the two electrodes are sometimes different, the difference between their work function can induce a built-in voltage to the devices, which would affect the injection of charges when the applied voltage is small.

1.4 Morphology of The Bulk Heterojunction Layer

Bulk heterojunction (BHJ) solar cell performance is very sensitive to the morphology of the BHJ layer, a solid mixture of donor(s) and acceptor(s) with nanosized morphology formed by phase separation during fabrication processes or post-treatments (see Figure 1.8). The phase separation is mainly driven by the mismatch in surface energy of the two components in the BHJ.[73] Crystallization of some conjugated polymers or small molecules is also responsible for the phase behavior.[74] The morphology of BHJ films is often characterized and expressed in terms of domain size, where domains refer to regions/spaces

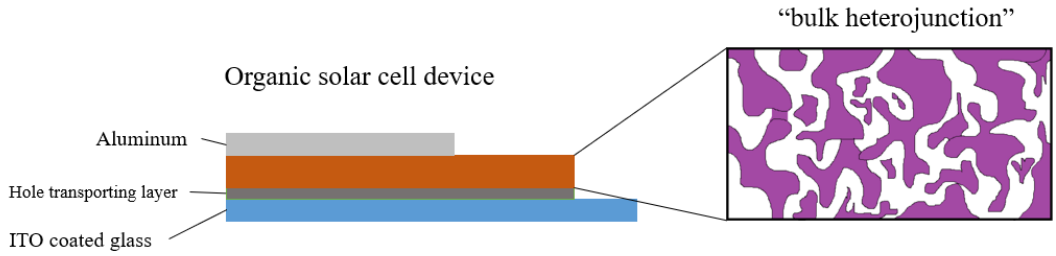

Figure 1.8 A schematic illustration of an organic photovoltaic device and the bulk heterojunction (BHJ) layer morphology. The BHJ layer contains a mixture of donor and acceptor materials, and the domain enriched by each component is represented by the purple or white area. It should be noted that the homogeneous domains (containing both donor and acceptor materials which are intimately mixed) might also exist in the BHJ, but are not drawn in the drawing. The real morphology of the BHJ is still under debate due to the difficulties in imaging the film on sub-nanometer scale.[75]

that are enriched in one of the components of BHJ materials.[75] Even though "good morphology" has been reported for most efficient BHJ solar cells, precise control of the domain size and nanomorphology of the BHJ is still difficult. An optimal BHJ morphology is qualitatively pictured as the interpenetrating network of the donor and acceptor that features a large interfacial area, with the domain size being large enough to support efficient charge transport, and, at the same time, small enough such that the excitons can successfully diffuse to the interface. By considering the typical exciton diffusion length, L_D, of organic materials and the charge recombination lengths predicted by Onsager theory[67], the optimal domain size is predicted to be at the 10-20 nm length scale.[73]

Controlling the BHJ morphology can be achieved with various methods, such as proper solvent usage, use of solvent additives, varying donor acceptor blend ratio, thermal annealing and solvent annealing. In addition, chemical modification of molecular structure is also observed to have a profound impact on the morphology of the BHJ layer.

Solvents. Lee *et al.* demonstrated a dramatic change in domain size when spin casting BHJ materials from solvents with different boiling points.[76] In particular, films spin cast from high boiling point solvents, such as chlorobenzene and xylene, exhibit large domain sizes on the order of 100-200 nm, as compared to the films spin cast from chloroform solution with domain sizes of ca. 27 nm. This is due to the strong demixing behavior observed for the studied materials and the slow evaporation of chlorobenzene and xylene which allows sufficient time for the growing of domains. On the other hand, for P3HT:PCBM BHJ, chlorobenzene is a better solvent choice than chloroform as the phase separation of the two components is not strong enough to form nanosized domains when spin casting from chloroform.

For some small molecule (donor) - fullerene (acceptor) systems, the device performance can be significantly improved by adding a small amount of solvent additive, such as diiodooctane (DIO).[11,77] This solvent additive has a high boiling point of 167 ^{0}C which evaporates slowly during spin casting. As a result, the extent of phase separation in BHJ films can be controlled by changing the volume ratio between the processing solvent and solvent additive.[78]

D:A blend ratio. Donor acceptor blend ratio can also impact the morphology of the BHJ films. For many crystalline polymer donors, spin casting the solution containing both polymers and fullerenes produces amorphous films with a uniformly mixed morphology. This occurs because the fullerenes remain well mixed and diffuse into the polymer chains during the solvent evaporation, thus disturbing the polymer crystallization. Kozub *et al.* have demonstrated that the P3HT and PCBM, even after extensive annealing, are miscible to some extent, which suppresses the fullerene crystallization.[79] Thus the desired

morphology is only achieved when fullerene content exceeds the miscibility limit. Controlling donor acceptor blend ratio is often the first step to optimize the BHJ morphology and the solar cell efficiency. The optimal D:A ratio can vary between 1:5 and 7:3 depending on the materials that are used.[11,41,80]

Thermal and solvent annealing. After spin casting the BHJ film, post treatments are often applied to the films in order to further control the phase separation and crystallization of the blend components. For example, a thermal post treatment is usually done on a hotplate (thermal annealing) or solvent annealing post treatments occur when subjecting the films to a solvent vapor environment. The thermal energy or solvent vapor allows the rearrangement of the polymer chains or molecules. Ultimately, it is the chemical incompatibility that drives the separation of the two components. However, it is much easier to control the phase separation extent by post treatments (by, e.g., changing the annealing temperature or time, or solvent vapor pressure) than by relying on changes during the spin casting process.

Molecular modification. Molecular structure also has a huge impact on BHJ morphology.[81–83] For example, by changing the alkyl chain length for P3HT, Gadisa *et al.* showed dramatic change in morphology and charge transport properties, resulting in different photovoltaic performances.[82] A similar effect has also been reported by Min *et al.* for small molecule donors.[83] So far, the studies on the impact of the molecular structure on morphology have been mainly focused on changing the solubilizing alkyl chains as such a modification of alkyl groups does not significantly alter the optical and electrical properties of the materials.

1.5 Small Molecule and Molecular Aggregates

1.5.1 Impact of molecular aggregates on OPV performance

Reliable and efficient BHJ solar cells have been well demonstrated with poly (3-hexylthiophene) (P3HT) and PCBM bulk heterojunctions, with reported power conversion efficiencies ranging from 3.5% to 5%.[84–86] Working with such benchmark materials, the research field has been focused on developing a fundamental understanding of photoinduced charge generation process in the OPV devices.[57,87–90] In the meantime, new materials with better chemical, optical, electrical and mechanical properties have been designed and synthesized,[91,92] along with novel device architectures[93,94] and improved processing conditions,[95,96] to push the power conversion efficiency toward 15%. Even though conjugated polymers continuously attract attention, small conjugated molecules have recently been demonstrated to exhibit comparable power conversion efficiencies.[97,98] Small molecules have several advantages over their polymer counterparts, such as well-defined molecular weight and structure (while polymer synthesis suffers from batch-to-batch variation), high solubility in solvents and easy synthetic and purification methods. Instead of conventional thermal deposition methods, solution processable small molecules for use in OPV devices have been recently discussed in detail.[99–101]

Traditionally, most conjugated dye molecules have been studied and used in solution (as isolated "monomers") but behave quite differently in the solid state, the expected geometry for OPV application. The intermolecular Coulombic interactions cause photophysical and transport properties of molecular aggregates to deviate from those of monomers. Aggregates are generally categorized into two types, H- and J-types, depending

on the alignment of the transition dipole moments. Typically, the H-aggregates exhibit a blue-shifted absorbance spectrum as compared to monomers, while the red-shifted absorbance is often associated with J-aggregation. The detailed descriptions of each type of aggregate can be found in section 1.5.2. Here we review the literature for the impact of molecular aggregates on solar cell performance. Meerholz and Würthner *et al*. have studied the impact of squaraine (SQ) H- and J-aggregates on solar cell performance.[102] Specifically, they have found that the H-aggregates seem to increase the open circuit voltage and J-aggregates appear to increase the short circuit current. However, the exact mechanism for such observations is still vague. Recently, the same group have reported bulk heterojunction solar cells employing a series of dipolar merocyanine dyes and their aggregates.[103] These dipolar dyes have a high tendency to aggregate, as reflected by the film absorbance spectra and X-ray diffraction measurements. Nevertheless, the impact of aggregates, as compared to molecular amorphous states (monomer), on solar cell performance is not discussed in detail.

In fact, the impact of molecular aggregates on solar cell performance has been under great debate. For example, Chen *et al*. have demonstrated a method to selectively control H- or J-aggregate formation of a SQ molecule by different processing solvents.[104] In particular, when spin cast from chloroform solution, the SQ preferentially forms J-aggregates in the films, while H-aggregate formation is dominated when ortho-dichlorobenzene is used. The solar cells made from the two different solvents showed that the J-aggregate formation has a large advantage over the H-aggregates, with higher Voc. This is inconsistent with the report from Meerholz and Würthner that the H-aggregate showed higher Voc in their SQ-based solar cells.[102] Previously, it was generally believed

that the J-aggregate is beneficial for exciton diffusion because of its large radiative rate constant, while the H-aggregate typically does not fluoresce, leading to an inefficient exciton diffusion via FRET. Recent theoretical work has demonstrated that exciton mobility can be very high in H-aggregates as well.[29]

Special care must be taken when studying the impact of molecular aggregation on OPV performance. First, the aggregation of small molecules in the neat films might be strongly inhibited in donor acceptor bulk heterojunction blends. For example, Chen *et al*. have studied a series of SQ dyes that can form H- or J-aggregates in neat films.[59] However, when blending SQ donors with a fullerene acceptor, $PC_{71}BM$, the absorbance spectra showed that the SQ aggregation is completely disrupted and the films are essentially amorphous. Thus, comparison between the contributions of H- or J-type aggregates to OPV efficiency is less valid as there is no evidence to quantitatively describe the relative populations of each aggregate type in the OPV-relevant films. Second, assigning the types of aggregate solely based on the peak shift of absorbance spectra is dangerous, as there are many other factors that could distort the absorbance peak, such as gas-to-crystal shift. Incorrect assignment of aggregation might lead to misleading conclusions about their contributions to solar cell performance. As we will show later, a proper interpretation of the photophysical properties of aggregates requires deep understanding of the intermolecular interactions which is often achieved with theoretical modeling.

1.5.2 The Exciton models for molecular aggregates

As introduced above, H- and J-aggregation has been identified for various chromophores. The intermolecular interactions in aggregates depend strongly on the orientation of the molecular transition dipole moments (TDM). As shown in Figure 1.9,

the TDM-TDM interaction leads to splitting of excited states, each higher or lower than the original monomeric excited state. This is often referred to as *exciton splitting*. According to Kasha's Exciton model,[105] the "face-to-face" dipole arrangement leads to an allowed transition from the ground state to the higher excited state (while the transition to the lower excited state is forbidden), resulting in a hypsochromically shifted absorbance peak. After excitation, the electrons in the higher excited state quickly relax to the lower excited state, from where the radiative transition to the ground state is suppressed. This type of aggregate is called an *H-aggregate*. When the molecules (and hence the TDM) are described as packing in a "head-to-tail" geometry, the transition from ground state to lower excited states is allowed, resulting in a bathochromically shifted absorbance peak and an enhanced emission rate. This class of aggregates is called the *J-aggregates*. As Kasha stated in his paper, this "head-to-tail" J-aggregate is more likely to be formed when the long geometrical molecular axis packed parallelly while the transition dipole moment is along the molecular short axis. The optically allowed state as often referred to as the "bright" state, and the forbidden state as the "dark" state. For slip stacking geometry as shown in the inset of Figure 1.9, the ordering of the bright and dark states is dependent on θ, an angle between the transition dipole moment and the line of the molecular centers. When $\theta = 54.7^0$, the bright and dark states are degenerate, and the exciton splitting is zero (the optical transition is independent of intermolecular distance and the strength of the interaction coupling).

The exciton model has been proven to be very successful in rationalizing the absorbance and emission behavior of the molecular aggregates. The model links the intermolecular Coulombic interactions to the molecular (and transition dipole moment)

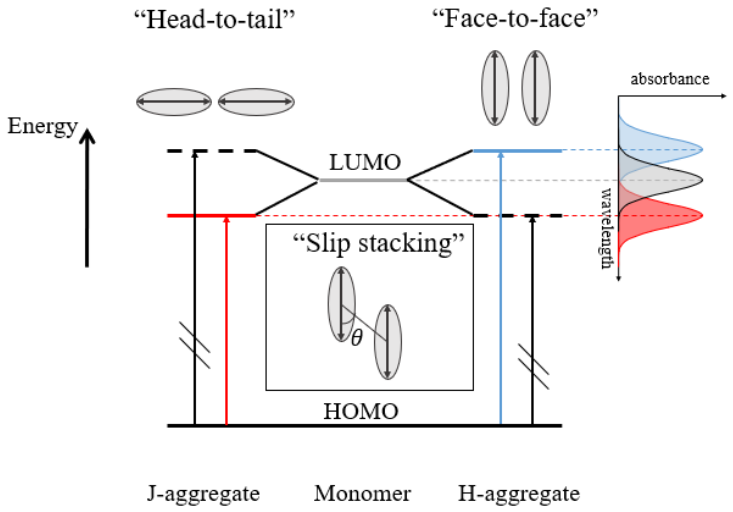

Figure 1.9 Energy level diagram for the Exciton model with ideal aggregates. The molecules are symbolized by the oval shapes with the double arrow representing the transition dipole moment. The intermolecular interaction in the dimer causes the splitting of the LUMO level. For the J-aggregate with the transition dipole moments aligned, the lower state is optically allowed, while the higher state is forbidden. On the other hand, the transition from the ground state to the higher state is allowed for the H-aggregate with a parallel transition dipole moment arrangement. For slip stacking geometry shown in the inset, the allowed transition depends on the slip angle, θ.

geometry, which has profound influence on design and synthesis of macromolecular assemblies with specific photophysical properties. However, there are some limitations associated with this model. For example, the energy levels are subjected to the gas-to-crystal shift due to the changing electric field of the environments (i.e. solvents, surrounding materials, etc.). This can disturb the interpretation of spectral shift of aggregates. In addition, the vibronic peaks (i.e. 0-v transitions, $v = 1,2,3$ ...) for organic materials can spread over 0.4 - 0.7 eV in the absorbance and emission spectra. These broad vibronic bands can further complicate the spectral behaviors of the aggregates.

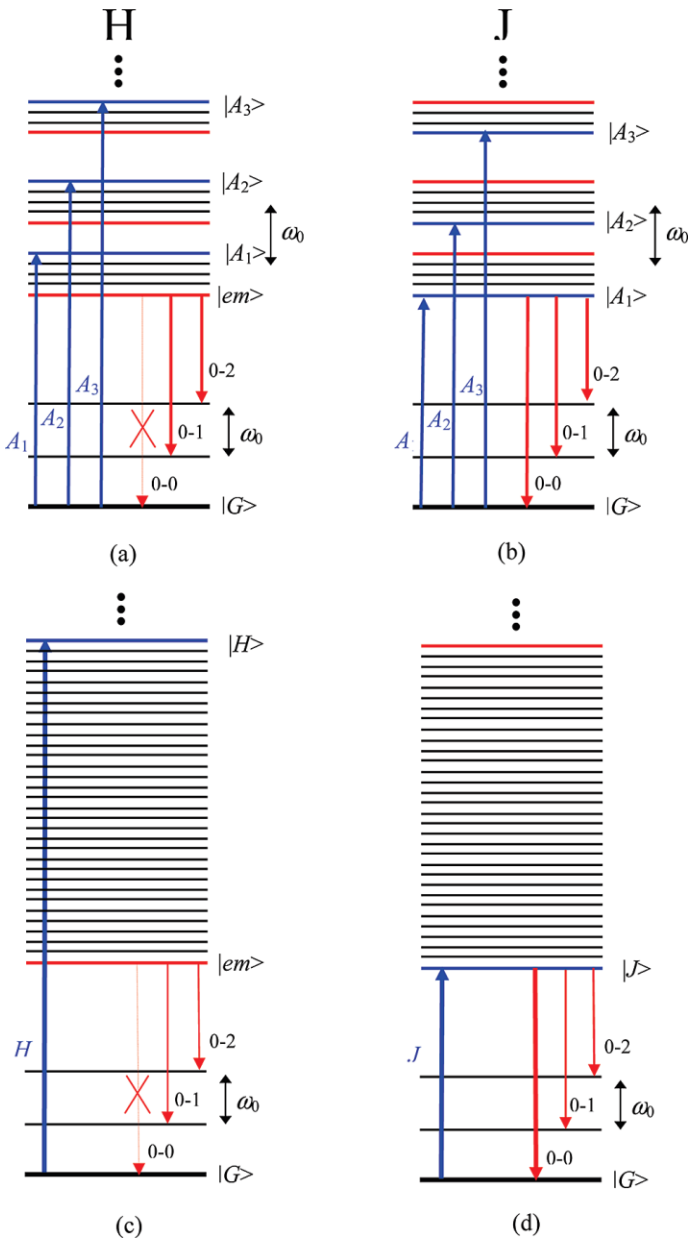

Figure 1.10 Energy level diagram of the Exciton model in ideal H- and J-aggregates with consideration of vibrational states. (a) and (b) represent the situations when the coulombic coupling is weak compared to the vibrational energy, ω_0, while (c) and (d) correspond to the strong coupling regime. For weakly coupled aggregates, the original vibrational states split into many sub-states where the ones on the top (bottom) of the package $|A_n\rangle$ are optically allowed for H-(J-) aggregate. When the coupling is strong, the splitting in vibrational states leads to a continuous distribution of vibrational states and the optically allowed state is located on the top (bottom) of the band for the H- (J-) aggregate. This figure is taken from reference 54.

In order to properly understand the photophysical properties of the aggregates, Spano has expanded Kasha's model to account for the effects of intermolecular coupling, vibronic coupling and disorder in crystals on an equal footing.[61,106] A detailed energy level diagram is drawn in Figure 1.10. Specifically, the absorbance line shape consists of all the transitions from the ground state (with no vibrational excitations) to the vibronically excited states based on the Franck-Condon principle. Each transition peak can be expressed as 0-0, 0-1, 0-2 … transitions, with the first and second number denoting the vibrational excitation in the ground and the excited state respectively. When the Coulombic coupling is weak as compared to the energy of a vibrational quanta (ω_0 = 1400 cm^{-1} for typical organic conjugated molecules), the vibrational states of aggregates are split into many sub-states within an energy package ($|A_1\rangle$, $|A_2\rangle$, etc. as shown in Figure 1.10). The optically allowed state is located on the top (bottom) of each vibrational package for H- (J-) aggregate. In addition, Spano has showen that the first two vibronic peak intensities are dependent on the Coulombic coupling strength, V,

$$\frac{I^{A1}}{I^{A2}} = \frac{\left(1 - 0.96\frac{V}{\omega_0}\right)^2}{\lambda^2\left(1 + 0.29\frac{V}{\omega_0}\right)^2} \tag{1.16}$$

where V is the Coulombic coupling term and λ^2 is the Huang-Rhys factor. Therefore, the ratio of first two vibronic peaks increases when $V < 0$ (corresponding to H-aggregate) but decreases when $V > 0$ (corresponding to J-aggregate).

When the coupling strength is large as compared to ω_0, the split in vibrational states is significant such that the vibrational levels are spread over the entire exciton band, while the bright state is located on the top (bottom) of the band for the H- (J-) aggregate. In this

case, the absorbance spectra would feature a single peak that is significantly blue- or red-shifted from the original monomeric peaks.

This ratio rule provides a more reliable method to identify the type of aggregates based on spectral line shape. As discussed above, the spectral shift might be due to the nonresonant intermolecular interactions (e.g. gas-to-crystal shift), while the vibronic peak ratio is less affected.

1.5.3 The Essential-state model for multipolar chromophores

In organic conjugated molecules, the overlapping p_Z orbitals of the carbon atoms arise from the alternating single and double bonds to give the pi-character. Charge delocalization is favored along the conjugation units and is responsible for the low-energy physics associated with this class of materials. While the exciton model is the most widely used computational approach to study the molecular aggregates, it does not take into consideration the effect of charge resonance on a single molecule. In multipolar chromophores, the electron donors and acceptors are often separated by a π bridge and the probability of finding the electron on an intramolecular donor or acceptor is highly sensitive to the dipole environments, leading to absorption or fluorescence solvatochromism.

An essential-state model (ESM) describing the charge transfer multipolar dyes has been developed by Painelli and coworkers recently.[107–112] For quadrupolar molecules, such as squaraine molecules, a trio of diabatic electronic states can be used to represents the main charge resonant structures: the zwitterion D^+A^-D ($|Z_1\rangle$, where an electron has been transferred from the left intramolecular donor moiety to the central intramolecular acceptor

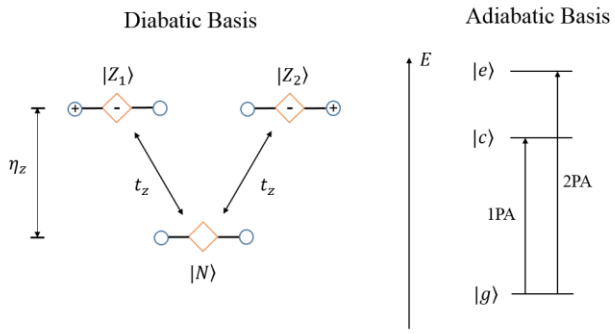

Figure 1.11 Schematics to illustrate the electronic basis states for quadrupolar chromophore in the Essential-state model (ESM). The diabatic states represent the main resonant structures of the molecule as a result of intramolecular charge transfer. The adiabatic states which are the eigenstates of the electronic Hamiltonian are responsible for the optical transitions. For linear quadrupolar chromophore, the first excited state $|c\rangle$ is one-photon (1PA) allowed and the second excited state $|e\rangle$ is two-photon (2PA) allowed.

moiety), DAD ($|N\rangle$), absent of intramolecular charge transfer, and the zwitterion DA^-D^+ ($|Z_2\rangle$, where an electron has transferred from the right hand donor moiety to the central acceptor moiety). Painelli *et al*. have also proposed a case where the electron resides on the π bridge for a dipolar system.[110] For symmetric SQs, the two zwitterion states, $|Z_1\rangle$ and $|Z_2\rangle$, are degenerate and separated from the neutral state, $|N\rangle$, by an energy η_z. The zwitterionic states couple to the neutral state via the electron transfer integral, t_Z, representing the movement of the electron (in squaraines) between a nitrogen atom on one arm and the central four membered ring (Figure 1.11).

The Hamiltonian constructed based on these diabatic states can be straightforwardly diagonalized to give the electronic eigenstates of the chromophore. Specifically, three adiabatic eigenstates are obtained as shown in Figure 1.11. The lowest-energy state is defined as the ground state, $|g\rangle$, while the two excited states, $|c\rangle$ and $|e\rangle$, are one-photon or two-photon allowed, respectively. These three eigenstates are able to characterize the

low energy physics of the quadrupolar chromophore, i.e. absorbance, fluorescence and two-photon absorbance.

Using ESM, Painelli *et al*. have investigated the solvatochromism effect and charge instability in fluorene-based and styrene-based quadrupolar chromophores, as well as squaraine dyes.[107] Later, they have expanded the ESM to study the Coulombic interactions in the associated aggregates.[113,114] In the aggregate model, they have mainly discussed the effect of Coulombic interactions on non-linear optics for multipolar chromophores. The ESM dimer model, with charge resonant diabatic states, naturally considers the polarizability of chromophores in the aggregates, providing an explicit advantage over the exciton model.

1.6 Squaraine Donors for OPVs

Squaraine chromophores has been enthusiastically researched for applications in BHJ-OPV devices recently due to its high extinction coefficient in the near infrared region of the solar spectrum as well as the facile synthetic processes.[115–117] Among many SQ structures, aniline- and indoline-based molecules are more synthetically accessible and thus are more frequently investigated for OPVs. With solubilizing alkyl groups attached to the nitrogen atoms, these SQ molecules generally exhibit high solubility in conventional organic solvents. Marks *et al*. have first reported a use of SQ donors in solution processed BHJ solar cells with efficiency above 1%.[118] In the report, the authors pointed out that the linear or branched alkyl substituents allow manipulation of the solubility as well as control the crystalline packing structures. They have also observed that the solar cell efficiency is sensitive to SQ:PCBM ratio and thermal annealing treatment, presumably due to the

changes in BHJ morphology. Later, the same group has compared the alkyl- and alkenyl-substituted SQ donors for BHJ-OPV devices.[119] The marked effect of different solubilizing alkyl groups has been further recognized.

Thompson and Forrest *et al*. have first reported highly efficient, vapor deposited OPV cells by using an aniline-based squaraine donor, later named "DIBSQ".[120] DIBSQ has been a very successful squaraine donor and high device efficiency can be realized by either solution or evaporation processes. In Wei *et al.*'s report,[120] when compared to the previously used, blue-absorbing copper phthalocyanine, DIBSQ-based devices with thinner donor layer (6.5 nm vs. 40 nm) can achieve higher efficiency (3.1% vs. 1.2%), marked its advantages in absorption (i.e. the high extinction coefficient and the NIR absorption peak). Later, the efficiency has been further increased to 4.6% by thermal annealing the donor layer to improve the SQ crystalline structures and subsequently the exciton diffusion length.[121] Yet, it has also been recognized that the exciton diffusion length is still short (~5 nm) even in these crystalline SQ structures, which significantly limit the use of a thicker donor layer for more efficient solar photon harvesting. Thus, the same group have explored the potential of DIBSQ in solution-processed BHJ solar cells.[40,41] Bulk heterojunction structure alleviates the negative influence of the short exciton diffusion length in DIBSQ donors and an averaged solar cell efficiency of 2.4 % has been obtained with the optimal DIBSQ:$PC_{71}BM$ ratio of 1:6. The lower efficiency can be attributed to the incomplete phase separation between DIBSQ and $PC_{71}BM$ in as-cast blends. Upon solvent annealing the BHJ layer in dichloromethane vapor, the SQ molecules crystallize and phase separate from the fullerenes, leading to a maximum device efficiency of 5.2%.[41] Later, the same group has explored various SQ molecules with N-aryl groups attached to the nitrogen

atoms.[122–125] The new squaraines exhibit red-shifted and broader absorption peaks as compared to DIBSQ. In addition, the aromatic groups are expected to improve π-π stacking of the SQ molecules and thus should improve exciton and charge transport. Yet, only small improvements have been seen.

Chen *et al*. have independently studied DIBSQ in solution processed OPV devices, with reported efficiency of 4.8% under 1-sum illumination.[126] Interestingly, the authors reported an improved power conversion efficiency of 6.1% by co-evaporating the DIBSQ and C_{70} to form the BHJ layer.[127] The authors also investigated the effect of alkyl substituents and the hydroxyl groups on the aniline moiety on solar cell performance.[59] Dramatic changes in absorption spectra of neat films and the SQ single crystal structures have been realized with small modifications in those functional groups, which are responsible for the different solar cell performances.

Recently, Yang *et al*. have explored the possibilities of using asymmetrical squaraines in BHJ devices, and device efficiencies similar to that of DIBSQ have been reported.[128–132] Noticeably, by binding two asymmetrical squaraine molecules together with a benzodithiophene unit, the hole carrier mobility has been improved significantly, leading to a high OPV efficiency of 6.33%.

Spencer *et al*. reported the unique aggregation properties of SQ molecules and the aggregates can be controlled by co-solvent methods.[133,134] These results highlight that the SQ aggregation can be used to control the thin film morphology and thus the device performance. SQ aggregates yield broader absorption spectra which should be beneficial for photon harvesting. At the same time, aggregates represent more ordered packing of molecules and thus are expected to have higher charge and exciton transport properties.

However, SQ aggregation does not always result in device improvements, and Spencer *et al*. made the efforts to apply Marcus-Hush theory to explain the changes in solar cell performance due to the SQ aggregation.[69]

To summarize the above short review, SQ has been utilized in OPV devices only recently, but the power conversion efficiency has been dramatically improved. These achievements were realized by combining the efforts in material design and synthesis, better device structures and fabrications, and deep understanding of these small SQ molecules and their aggregates. In order to further improve the device performance with better molecules, some critical inefficient properties of SQ donors must be overcome; i) the narrow absorption spectra of SQ single molecules, ii) the short exciton diffusion length and iii) the low charge mobility in SQ films. SQ aggregation might provide a solution to all three shortages as aggregates generally have much broader absorption profiles and the crystalline structure in the aggregates is expected to improve the transport properties. In this dissertation, we focus on the effect of squaraine aggregation on solar cell performance and the controlling of squaraine aggregation to further improve the OPV efficiency.

1.7 Aim and Outline of This Dissertation

This dissertation has been focused on developing efficient bulk heterojunction OPV devices based on small squaraine donors and utilizing their aggregation properties to optimize the BHJ morphology and therefore the solar cell efficiency. In this chapter, a basic description of the OPV principles and device physics have been introduced to provide a necessary background and reference for the following chapters. For example, the interpretations of the device parameters in Chapter 3 and Chapter 4, such as short-circuit

current and fill factor, are based on the description in Section 1.3.1. Then, the basics of theoretical models, i.e. exciton model and essential-state model, describing the electronic structures of small molecules and their aggregates have been introduced in Section 1.5. This sets up the launching point for Chapter 5 and Chapter 6.

The following chapters of this dissertation are arranged as follows. In Chapter 2, the experimental details of some major measurements in this dissertation are briefly introduced. The parameters and the set-ups are tuned for the specific measurements involving organic materials and for the specific instruments in the research labs at RIT and at other collaborating universities. The device making procedures have been continuously improved during the research, and different fabrication steps and materials might be used in different chapters, which are indicated in Chapter 2.

In Chapter 3, we start to investigate the effect of squaraine aggregation on BHJ morphology with the first SQ molecule, $DHSQ(OH)_2$. In the absorption spectra, we recognize that $DHSQ(OH)_2$ molecules may exist in either monomeric and aggregated form, and the relative population of monomers and aggregates depends on the weight ratio of the SQ and fullerene. Thermal annealing can induce $DHSQ(OH)_2$ aggregation, causing depletion of monomer population. The film crystallinity and donor-acceptor phase separation are investigated and correlated to SQ aggregation behavior. The OPV device performance is related to the morphologies of the BHJ. In Chapter 4, we explore the effect of N-alkyl substituents on SQ aggregation and BHJ morphology. The device efficiency is further improved to 4-5% with a better designed SQ molecule, $DBSQ(OH)_2$. We find that the SQ aggregates always decrease the power conversion efficiency of the device even

though the BHJ morphology is improved. This should be attributed to the changes in excited state structures of the SQ aggregates as compared to the monomeric state.

In Chapter 5 and Chapter 6, we use essential-state model to theoretically investigate the excited states structures of the SQ aggregates that are relevant to OPV. We identify two types of intermolecular interactions in the SQ aggregates: Coulombic coupling (CC) and intermolecular charge transfer (ICT). Here, we construct theoretical models based on the essential-state model[107,108] to *extract* the information about the excited state structures of these SQ aggregates. The spectral signatures of these aggregates are analyzed to provide a spectral-based diagnostic approach to identify the desired aggregates for OPV application.

In Chapter 7, we further investigate the excited state dynamics in the SQ aggregates. It is recognized that the excitons in Coulombically coupled (CC) aggregates are highly mobile and efficient energy transfer happens from SQ monomers to CC-aggregates. Thus, it is expected that the excitons generated in the system with mixed population have a high probability to reach the heterojunction interface and generate free charges. This at least partially explained the high efficiency obtained from these highly amorphous systems. Finally, Chapter 8 summarizes and concludes for this dissertation.

Chapter 2. METHODS

In this chapter, the materials and the general methods that are employed in this dissertation are introduced. Note that the experimental procedures have been continuously improved over time during this dissertation work, and these will be explicitly stated in the following contents.

2.1 Materials

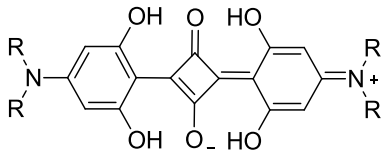

SQ

Figure 2.1 A general chemical structure of squaraine molecules.

In this dissertation, aniline-based squaraine (SQ) molecules were used as the donors in BHJ-OPV devices. These SQ molecules are synthesized by Dr. Jeremy Cody's research group at Rochester Institute of Technology (RIT). SQs have high extinction coefficients exceeding 10^5 cm^{-1} and narrow band gaps of ~ 1.6 eV. The general formula of SQs features a symmetric structure with a central squarylium and two di-hydroxyl anilines (shown in Figure 2.1). The squarylium is an electron acceptor while the nitrogen atoms on the anilines act as electron donors, forming a donor-π-acceptor-π-donor structure. Bigelow and Freund performed semiempirical molecular orbital calculations on SQs and have found that in solutions, the solvent cage surrounding the squarylium is positively charged while the negatively charged solvent cage is found near the nitrogen atoms.[135] This indicates that the

ground state of SQ molecules has a strong zwitterionic character (partial positive charge on two nitrogen atoms while partial negative charge on two oxygen atoms, as drawn in Figure 2.1).

The peripheral groups on the nitrogen atoms are alkyl chains to ensure a good solubility of SQs in conventional organic solvents. We found that SQs with alkyl groups of at least four hydrocarbons (i.e. either n-butyl or iso-butyl) have a good enough solubility for solution processing (> 16 mg mL^{-1}). The peripheral chains also influence the crystal packing. For example, SQ with iso-butyl chains crystalize into a monoclinic structure with a space group of *P*21/*c*,[122] while SQ with n-butyl chains has a triclinic crystal structure with a space group of *P*-1.[136]

[6,6]-phenyl C_{61} butyric acid methyl ester (PCBM) or [6,6]-phenyl C_{71} butyric acid methyl ester ($PC_{71}BM$) was used as the acceptor for our BHJ devices. Poly(3,4-ethylenedioxythiophene) polystyrene sulfonate (PEDOT:PSS) or molybdenum trioxide (MoO_3) was used as the cathode buffer layer to provide better ohmic contact between the BHJ and the Indium tin oxide (ITO). All these materials are commercially available and used as received.

2.2 Optical Characterization

Absorbance and fluorescence are critical methods and often the first step to characterize the excited state properties of SQ chromophores. The absorbance measured from dilute solution can give information on excitations of individual molecules, while the absorbance studies of thin films are measuring the excitations on molecular aggregates or crystalline structures. The change in the spectra of solutions and films can yield

information about the intermolecular interactions in aggregates. The optical measurements are performed for SQs in different environments, *e.g.* Poly(methyl methacrylate) (PMMA) films, neat films and blend films.

Solutions. SQs were dissolved in conventional organic solvents, such as chloroform, chlorobenzene, tetrahydrofuran (THF) and dimethyl sulfoxide (DMSO). Several dilution steps were needed to bring the optical density low enough for the UV-Vis instrument (Shimazu-2401PC spectrophotometer). SQs in our lab exhibit sharp absorbance peaks in solution with extinctions coefficients of > 10^5 M^{-1} cm^{-1} at ~ 650 nm. Fluorescence of SQs in solution was measured using a HORIBA FluoroMax fluorometer. The photoluminescence quantum yield (PLQY) was obtained by using a Quanta-φ integrating sphere. All squaraines have a high PLQY of > 0.8, which falls in the typical characteristics of squaraine dyes.[116,117]

Films. Thin films were made by spin casting the solution with a concentration of 8-16 mg mL^{-1} onto glass substrates. Chloroform was frequently used as the solvent. Typically, the film thickness is in the range of 80-200 nm. The absorbance spectra of the films were largely affected by the addition of PCBM or PMMA, and less sensitive to the concentration and spin speed. In some cases, thermal annealing was performed to the films to induce SQ aggregation. The thermal treatment was performed by placing the film on a digital hot place at a set temperature (the temperature at the surface is calibrated against an infrared thermometer and a ± 5 ºC deviation from the displayed value is assumed). After annealing, the films were allowed to cool to the room temperature before taken to the absorbance measurements.

PMMA films. For some studies, polymethylmethacrylate (PMMA) polymer and SQs are co-dissolved in chloroform solution and then spin cast into thin films. The solution is often heated on a hotplate set at 60 ^{0}C for 5-10 min to ensure the solids are fully dissolved (especially for low SQ weight percent films). Here, the weight percent (wt%) of SQ is defined as the ratio of SQ mass divided by the total weight of both SQ and PMMA solids. Upon spin casting, the SQ molecules are dispersed in the PMMA matrix with the molecular separation controlled by the wt% of SQs. The average molecular separation, d, between SQ molecules in the PMMA matrix can be estimated via:

$$d = \sqrt[3]{\frac{M}{N_A \times wt\% \times \rho_{PMMA}}} \tag{2.1}$$

where M is the molecular mass of SQ molecule, N_A is the Avogadro's number and ρ_{PMMA} is the density of PMMA (typically 1.17 g cm^{-3} obtained from Sigma-Aldrich). Note that Equation (2.1) is under the assumption that adding SQ in PMMA matrix does not alter the density nor the volume of the thin films. Thus, it only works at low SQ wt% regime.

Mixed-solvent solution. For mixed-solvent solutions, we dissolved SQs in a solvent mixture containing DMSO and H_2O. DMSO is a good solvent with a high solubility for SQ monomers and is miscible with H_2O to form a uniform solvent environment. H_2O is a non-solvent for SQs. Thus, the solvent quality can be precisely controlled by changing the volume ratio of DMSO and H_2O.[137] For making a mixed solvent solution, we first dissolved SQ into DMSO to make a stock solution with concentration of 1 mg mL^{-1}. Sonication of the DMSO solution were sometimes needed to ensure that the SQs are fully dissolved. A series of blank solvent blends were prepared with varying DMSO/H_2O volume ratio. The final solutions were made by slowing injecting the DMSO stock solution into the blank

solvent mixture during sonication. The nano-sized aggregates were found to be stable in the solvent mixture for ~ 2-8 hrs. For absorbance measurements, the blank solvent mixtures were used to baseline the spectrometer before taking measurements of each corresponding mixed-solvent solution.

2.3 Solar Cell Device Fabrication

Patterning ITO substrates. In Chapter 4, we describe results from devices made from using patterned ITO, which allows us to get better contact to the two electrodes when taking voltage-current measurements in the glove box. Commercialized ITO plates (5×5 inches) obtained from VisionTek Systems Ltd. were cleaned by rinsing in acetone, isopropanol and deionized water consecutively, and then subjected to air drying. The cleaned ITO plates were then transferred to the Semiconductor & Microsystems Fabrication Laboratory (SMFL) at RIT for lithography processes. In SMFL, HPR-504 photoresist was spin cast onto the ITO plates at a spin speed of 2000 rpm, followed by a soft bake step at 120 ^{0}C. The photoresist layer covered by a self-designed chromium mask (making contact with the photoresist layer) was then exposed to the mercury broadband irradiation. The exposed photoresist was developed using CD-26 positive developer, followed by a hard bake step at 120 ^{0}C. The etching step was performed on a hotplate at 100 ^{0}C (digital reading, while the etchant is at 35 – 55 ^{0}C) for 5 minutes. The etchant was made of hydrochloric acid with 1:1 dilution by deionized water. The etched ITO plates were rinsed in acetone to wash off the un-exposed photoresists, followed by consecutive rinses in isopropanol and deionized water. In the final step, the large 5×5 inches ITO plates were cut into small substrates, each with a dimension of 20×15 mm.

OPV device fabrication. An appropriate number of ITO substrates (unpatterned ITO substrates in Chapter 3 and patterned substrates in Chapter 4) were cleaned in an acetone and isopropanol ultrasonic bath, followed by double rinses in hot deionized water. Substrates were dried using the vacuum air gun with a proper use of cleanroom wipes. At the back of the substrates, the device number was labeled and (for patterned ITO substrate) the divisions between each ITO strip were marked with a line. (The number is to help to easily differentiate devices with different processing conditions and the line is to help find the ITO contact when testing the devices). The substrates were then moved to an oven and annealed at 150 ^{0}C for 15 minutes to ensure that any solvents attached to the surface were fully evaporated. Then, the substrates were UV-Ozone (Jelight Inc. Model 18) treated for 15 minutes.

For devices using a PEDOT:PSS cathode buffer layer (used in Chapter 3), a 1 mL PEDOT:PSS dispersion (obtained from Ossila Inc.) was taken out from the refrigerator and filtered through a 45 μm PTFE filter to remove any large aggregates or particles. Then, the dispersion was spin coated onto the ITO substrates at a spin speed of 4000 rpm, followed by a bake step at 150 ^{0}C for 5 minutes.

For devices using a MoO_3 cathode buffer layer (used in Chapter 4), the patterned ITO substrates were loaded into a cathode buffer layer mask, and then the mask was installed in the vacuum deposition system (Angstrom Engineering Inc.). The MoO_3 evaporation was done in the vacuum with a base pressure of $< 1 \times 10^{-6}$ Torr and a rate of 0.5 Å s^{-1}. After the evaporation, a 100 Å MoO_3 was obtained.

After fabrication of the cathode buffer layer, the substrates were immediately transferred into the glove box to a spin coater. The BHJ layer was obtained by spin casting

the solution onto the substrate at a spin speed of 1500 rpm (unless another speed is noted). For some studies, some BHJ coated substrates were annealed on a hotplate in the glove box; (temperature varies for different studies and will be stated in each Chapter).

Then the BHJ coated substrates were loaded into an anode layer mask for anode layer deposition. Similar to the MoO_3 deposition step, the loaded mask was installed into the evaporator and the base pressure of the chamber was allowed to drop to $< 1 \times 10^{-6}$ Torr. The aluminum is evaporated onto the BHJ layer at a rate of 3 Å s^{-1} with a final thickness of 1000 Å. The final device structure is: ITO(~100 nm)/MoO_3 (10 nm) or PEDOT:PSS (~40 nm)/SQ:PCBM BHJ (~70-120 nm)/Al (100 nm).

Some devices were encapsulated to preserve the photovoltaic materials from degradation. For encapsulation, a glass coverslip and epoxy glue (products from Ossila Inc.) were used to encapsulate it. It was observed that the BHJ active layer material is soluble the epoxy and the device efficiency was found to drop by ~ 15% when measured immediately after encapsulation (although the stability was found to be improved significantly). When storing in ambient condition, the device degrades to < 20% of its original efficiency after 24 hrs. When storing in a nitrogen-filled glove box, the device retains 30 – 50 % of its original efficiency after 24 hrs. When encapsulated with epoxy and cover slips, the device can retain ~ 90% of its efficiency after a week (see Appendix B).

2.4 Solar Cell Performance Evaluation

Current-voltage (J-V) testing. J-V tests were performed on a Newport 91192 solar simulator at a power of 100 mW cm^{-2}. The light intensity was calibrated against standard InGaP solar cells fabricated in NASA Glenn Research Center, Photovoltaic Branch 5410.

The calibration was performed once a month. The OPV devices were tested immediately after the anode layer deposition to prevent any device performance fluctuations due to the material degradation. The J-V measurements were taken by using a Keithley 2400 sourcemeter and a four-point probe geometry. Each device was scanned by sweeping the voltage from -2 V to 2 V.

For devices using unpatterned ITO substrates (in Chapter 3), the J-V test was performed outside the glove box and the probes were placed onto the ITO and aluminum to get contact on these two electrodes. The device area was defined by the area of the aluminum capping layer, which is 2.9 mm^2. Great care had to be taken as the probes can very easily penetrate the thin aluminum layer (100 nm), causing damage to the devices. For devices fabricated on patterned ITO substrates, the device area was defined by the overlapping area of aluminum and ITO, i.e. 4.5 mm^2. Good ohmic contact on both electrodes can be achieved easily without worry of damaging the devices.

The data were collected using an internally developed LabView program. The solar cell short circuit current, open circuit voltage, fill factor and power conversion efficiency were reported by averaging over 16 devices for each data point presented here, and the standard deviations were provided in all cases. Some data from obviously defected devices (e.g. those with significant current leakage or completely short-circuited) were excluded from the averaged value. The percentage of defected devices was less than 5% for devices on patterned ITO substrates and around 25-50% for devices on unpatterned ITO substrates (penetrating the aluminum layer is often the cause).

Spectral response test. External quantum efficiency (EQE) of the solar cell was measured on a spectral response set-up at NanoPower Research Laboratory (NPRL) at RIT.

The system was calibrated against a Si standard supplied by Optronic Laboratories. The light generated by a halogen bulb was sent to a monochromator and then a beam chopper. The monochromatic light was then focused on the solar cell device with a beam diameter of ~1 mm. The currents were measured by two probes attached to ITO (cathode) and aluminum (anode) respectively, using a specialized tool box which is designed and manufactured by Chenyu Zheng and the RIT machine shop. The current signal was sent to the Stanford Research System (SRS) 570 preamplifier. The SRS 570 preamplifier is able to detect current as low as nano amperes and then up-converts it to voltage signal, which is sent to the SRS 830 Merlin lock-in amplifier. The Lock-in amplifier was set to the frequency of the beam chopper. The EQE spectrum and data were obtained using a LabView program.

2.5 Hole-only Device

For measurement of hole carrier mobility, the hole-only devices were fabricated. The preparation/cleaning of ITO substrates is the same as that described in Section 2.3. The ultra-cleaned ITO substrates were then loaded to the evaporator for MoO_3 deposition. At the proper base pressure, a 10 nm-thick MoO_3 layer was evaporated onto the substrates. Then a BHJ layer or a neat donor layer was deposited by spin coating. Each device was capped with another 10 nm-thick MoO_3 layer and a 100 nm aluminum cathode. The device structure is: ITO (~ 100 nm)/MoO_3 (10 nm)/SQ or SQ:PCBM BHJ (~100 nm)/MoO_3 (10 nm)/Al (100 nm). The MoO_3 layers are acting as hole injection and extraction layers due to the low MoO_3 work function.[128] The hole mobilities of the pristine squaraine films as well as of the SQ:PCBM blend films are extracted by fitting the current−voltage curves of

single carrier devices to the Mott−Gurney law (Equation (1.15)) for the voltage region where the current is space-charge limited.[72]

The film thickness is an important parameter that must be measured before applying Equation (1.15). The thickness is measured by an atomic force microscope (Bruker Inc. model INNOVA) performed in tapping mode. First, the films were obtained by spin casting onto glass substrates with a spin speed and a concentration that is the same as is used when preparing the hole-only devices. Then the films were immersed in deionized water to allow the film to crack and create a sharp edge. The thickness of the film can be readily measured using AFM by scanning across such a sharp edge.

Electric measurements were performed inside the glove box using a Keithley 2400 sourcemeter in the dark. The voltage is scanned from 0 V to 6 V to ensure that the space-charge limited regime is reached.

2.6 Morphology Characterization Techniques

The morphological characterization techniques applied in this dissertation include X-ray diffraction (XRD), transmission electron microscopy (TEM), atomic force microscopy (AFM), Differential Scanning Calorimetry (DSC) and thermogravimetric analysis (TGA).

XRD. In this dissertation, two different XRD systems were used. In Chapter 3, The XRD system was built at RIT. Monochromated Cu Kα radiation (λ = 1.542 Å) generated from an analytical sealed tube X-ray source was employed to make the measurements under ambient conditions (293 K). The films were made by spin casting a solution onto the glass substrates. The blank substrates were measured on the identical set up to account for the scattering and diffraction of the X-ray beam by those substrates (the glass). The final

X-ray diffractograms were obtained by subtracting the results of the blank substrates. The diffraction was scanned using a dwell time of 2-8 seconds for each data point to increase the signal-to-noise ratio.

In Chapter 4, thin film XRD measurements were taken at Alfred University, through a collaboration with Scott Misture. A Bruker D8 Advanced system with a Bragg-Brentano geometry set-up was used to take the XRD measurements at room temperature. The diffracted X-ray signal is measured using a LYNXEYE XE position sensitive detector while the films were slowly spinning at a rate of 30 rpm. *In-situ* high-temperature X-ray diffraction measurements (*in-situ* HTXRD) were performed with an Anton PAAR high temperature control system. The X-ray sources are Cu Kα1 (1.54056 Å) and Kα2 (1.54439 Å) lines for both room temperature and high temperature. The films were prepared on the ITO/MoO_3 substrates with the same procedure of OPV fabrication (without aluminum cathode layer). The scans of ITO/MoO_3 substrates were used as the baseline to selectively investigate the diffraction peak of the squaraine crystalline structure. For *in-situ* HTXRD, the diffractograms were measured during a thermal ramp from 30 ^{0}C to 150 ^{0}C (with a 30 ^{0}C interval), then cooled back down to 30 ^{0}C. Powder XRD were measured by carefully spreading the squaraine powders onto a quartz holder. The measurements were taken in both room temperature and high temperature systems.

TEM. A JEOL JEM-2010 transmission electron microscope was used to directly investigate the BHJ morphology. The TEM employed a 210 LaB6 filament and was operated at 200 kV. An AMT image capture system was used to take images. Due to the difference in mass densities of SQ and PCBM, the PCBM-enriched domains appear darker than the SQ-enriched regions. The domain size was estimated by using ImageJ software.

The films for TEM studies were prepared by spin casting solution onto glass substrates and subsequently immersing the films into deionized water. Each film was picked up by a specialized TEM microgrid and then dried by gently touching the microgrid with a cleanroom tissue. The water was allowed to further evaporate under ambient condition. The focus of the electron beam was achieved on local defects of the films, such as cracks or holes and images were then taken on the area beside these defects. The quality of the TEM images was free from the distortions by any image processing.

AFM. The surfaces of the organic films were analyzed using an INNOVA AFM system. The measurements were performed under tapping-mode at ambient condition. The rate of each scan was set at 0.5 Hz. The area of each scan was typically 5×5 μm. The surface roughness was readily obtained from the software with the AFM height image. The AFM images were free from the distortions by any image processing.

DSC and TGA. DSC is a powerful tool to analyze the thermal behavior of the bulk materials. It measures the temperature of the analytes versus the thermal energy provided to it. For melting, crystallization and other exo- or endothermic processes of the analytes, a TA Instruments Q2000 differential scanning calorimeter was used. The sample was loaded in a hermetic aluminum pan and a lid was gently crimped on by using a TA Instrument Press. For decomposition of the materials, a TA Instruments Q500 thermogravimetric analyzer (TGA) was used. The sample was massed using the integrated balance in the TGA prior to thermal ramping and was continuously weighed during the thermal ramping. For DSC, the temperature was ramped back and forth three times from 25 ^{0}C to 270 ^{0}C at a constant ramping speed of 10 ^{0}C min^{-1}. Nitrogen gas was flowed during the scan to prevent material from degradation. For TGA, the temperature was ramped from

25 ^{0}C to 400 ^{0}C at a speed of 5 ^{0}C min^{-1} (after the first ramping, the materials were completely degraded/vaporized).

2.7 Time-resolved Measurements

The excited state lifetime was measured using a time correlated single photon counting (TCSPC) system at RIT, and a transient absorption (TA) spectroscopy system at the University of Rochester.

In TCSPC system (See Figure 2.2), a Newport Ti:Sapphire laser with an output wavelength of 800 nm and a frequency of 76 MHz was used as the excitation source. The laser pump was then converted to the desired wavelength (between 600 nm and 640 nm) by passing it through an optical parametric oscillator (OPO) and a frequency doubling crystal. The beam was then split into two; one triggered the Fast Trigger Diode to initiate the Picoharp 300 picosecond timer and the other excited the sample/analyte. The luminescence was subsequently detected at the right angle geometry with respect to the excitation beam. A monochromator was used to select the emission photons. Immediately after the Avalanche photodiode detected an emitted photon, the Picoharp 300 timer was stopped (the Picoharp 300 timer has a resolution of 4 pico-seconds). The laser pulse duration and the slit width of the spectrometer must be tuned such that no more than one photon is received per start-stop cycle. The fluorescence lifetime was obtained by tail fitting the decay curve.

The femtosecond transient absorption (TA) spectroscopy studies were performed through a collaboration between RIT and University of Rochester. The initial research ideas originated with Chenyu Zheng, who also prepared all samples at RIT. The TA

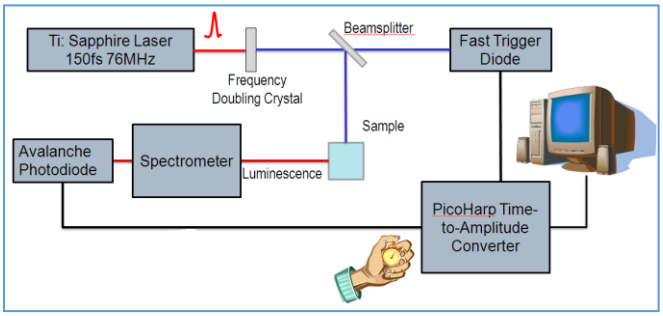

Figure 2.2 A schematic of the time correlated single photon counting (TCSPC) system at Rochester Institute of Technology. The optical parametric oscillator (OPO) is used to provide excitation beam tuning but is omitted in this schematic.

experiments and data interpretation were conducted by Michael Mark at the University of Rochester. The results were discussed by Michael Mark and Chenyu Zheng. In order to assist the readers, the experimental details are introduced here with the full recognition that Mark performed the measurements and data collection.

For the TA set up, A regeneratively amplified Ti:Sapphire laser was used to generate a laser pulse at 800 nm and at a 1 kHz repetition rate. The laser beam was converted to the desired pump wavelength of 640 nm by passing it through a non-collinear parametric amplifier (NOPA).[138,139] The probe beam was created by focusing a beam of the 800 nm fundamental onto a sapphire crystal to generate a white light continuum from 450 nm to 1000 nm. The transient absorption signal was collected by a grating spectrograph (Acton, 300mm fl, 150gr/mm) before reaching a charge-coupled device (CCD) camera (Princeton Instruments, Pixis 100BR). The white light was filtered by using a dye solution (NIR800A, QCR Solutions Corp) to block the residual 800 nm photons. During the experiments, the samples were translated in both x and y direction on a mechanical stage to prevent photo-

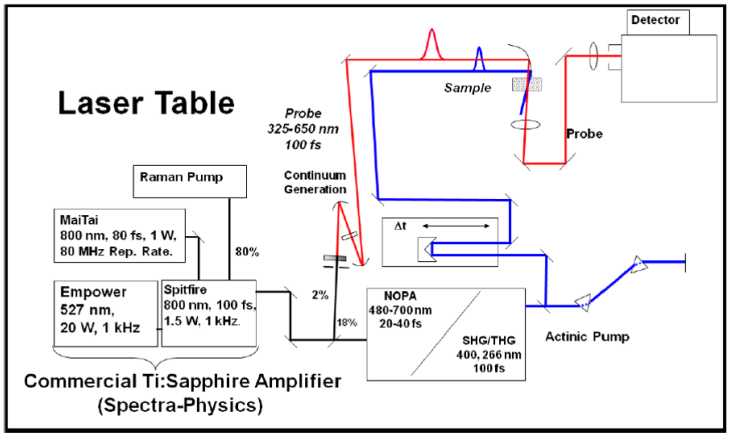

Figure 2.3 A schematic of the femtosecond transient absorption spectroscopy set up at University of Rochester. The commercially available Ti:Sapphire Amplifier (Spectra-Physics) was used as the laser source. The pump beam was generated by a non-collinear parametric amplifier (NOPA). The probe beam was generated by focusing the fundamental 800 nm onto a sapphire crystal to generate a white light continuum from 450 nm to 1000 nm. The transient absorption signal was collected by a grating spectrograph and a CCD camera (not drawn).

bleaching. For solution measurements, the sample was injected into a 2-mm fused silica cuvette with an absorbance of 0.7 at the maximum.

The transient absorption anisotropy was obtained by collecting the transient signal by setting the probe beam at parallel and perpendicular geometries with respect to the pump polarization. The transient anisotropy was calculated via

$$\rho(t) = \frac{(\Delta A_{\parallel} - \Delta A_{\perp})}{(\Delta A_{\parallel} + 2\Delta A_{\perp})} \tag{2.2}$$

For power dependent study, the TA spectra were collected at three powers of 20, 40 and 80 nJ/pulse.

Chapter 3. BHJ MORPHOLOGY AND MONOMER-AGGREGATE POPULATION CONTROL IN SQ:PCBM SOLAR CELLS

In this chapter, we investigate the effect of squaraine (SQ) aggregations in SQ:PCBM bulk heterojunction solar cells. First, we demonstrate a mixed population of monomers and aggregates existing in spin-cast SQ:PCBM BHJ films, where monomers indicate amorphous regions and aggregates are crystalline domains in the BHJ. The population of monomers and aggregates can be tuned by thermal annealing the as-cast films. Our analysis of annealed films demonstrates a delicate trade-off between increased crystallinity and larger domain sizes. Crystallinity improves but often at the expense of larger crystal size, as supported by XRD and TEM measurements. In order to achieve high solar cell performance, we need to improve the film crystallinity and at the same time control the domain growth.

3.1 Introduction

The significant dependence of solar cell efficiency on bulk heterojunction morphology is well established for polymer-fullerene solar cells.[140,141] In terms of how this morphology impacts device efficiency, a well-mixed, small-domain-size morphology with a large donor-acceptor interface will lead to an efficient exciton dissociation. On the other hand, mixed domains may cause inefficient electron and hole charge transport, and higher probabilities for geminate or bimolecular recombination in the BHJ. The optimal BHJ morphology is anticipated as small-size domains (on the 10-20 nm length scale) of donor or acceptor interdigitated into each other to enable i) a large interfacial area that allows an efficient exciton dissociation and ii) connected pathways for each electron or hole to efficiently charge transport to the electrodes.[142] Müller et al. described how it is necessary to simultaneously maximize exciton generation, exciton dissociation and charge transport. However they also state that optimization of the blend ratio and processing protocols to dial in the perfect morphology is a huge barrier to overcome.[143]

For the benchmark material, P3HT, it is well documented that through annealing, the polymer crystallization is the driving force for micro- and nano-structure evolution in P3HT:PCBM blends, while PCBM crystallization is suppressed by miscibility of the fullerene and polymer.[144] As a consequence, a desirable morphology is achieved with a co-existence of pure P3HT crystalline phases and P3HT:PCBM mixed phases leading to an optimal performance. Thus, the morphological improvements can be achieved with the processing conditions.

SQ molecules are known to form aggregates/crystallites in the solid state films.[145] However the morphology in SQ:PCBM BHJ solar cells is less investigated.[126,129,146] It is

suggested that the SQ crystallites exist in the BHJ especially after thermal or solvent annealing, but the size of the crystallites is less clear. Many SQ molecules[59,126,130,130,147,148] synthesized for OPV application show various absorption spectra in neat films with multiple peaks, blue- or red-shifted from the monomer peak in solution, which are thus assigned to H- or J-aggregates. Nevertheless, when blended with PCBM, the absorption spectra are more or less the same (broader profiles with the same peak as the monomer absorbance in solution).

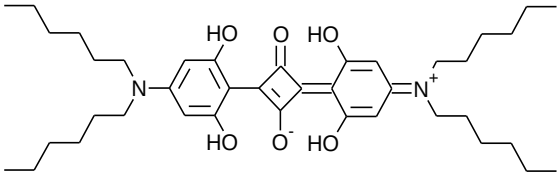

DHSQ(OH)$_2$

Figure 3.1 Chemical structure of DHSQ(OH)$_2$.

In this chapter, we investigate the effect of squaraine (SQ) aggregations in SQ:PCBM bulk heterojunction solar cells. First, we measured the absorbance spectra of DHSQ(OH)$_2$ (2,4-bis[4-(N,N-dihexylamino)-2,6-dihydroxyphenyl]squaraine) (Figure 3.1) molecules in solution, neat film, and in BHJ films with varying donor acceptor blend ratios. DHSQ(OH)$_2$ in solution are monomers with a sharp absorbance peak at 650 nm and a high extinction coefficient. DHSQ(OH)$_2$ in neat films are strongly-coupled aggregates that have broad absorbance profiles with two peaks at 560 nm and 660 nm. The absorption spectra of DHSQ(OH)$_2$ in BHJ films are different from the above two situations, exhibiting a mixed population of monomer and aggregates. Second, we use a X-ray diffraction set up and a bright-field transmission electron microscope and to investigate the film crystallinity and

phase separation in $DHSQ(OH)_2$:PCBM BHJ during thermal annealing. We have demonstrated that the $DHSQ(OH)_2$ monomers are present in amorphous regions while aggregates represents crystalline structures in the BHJ. Finally, organic solar cells were fabricated and the efficiencies were then correlated with the BHJ morphology. We have concluded that the optimal BHJ morphology can be obtained by first using a high fullerene weight ratio to suppress $DHSQ(OH)_2$ aggregation, and then thermal annealing the blend film to improve the film crystallinity. The annealing temperature is critically controlled such that the crystallinity is improved without invoking phase separation.

3.2 Absorbance Study of SQ Aggregation in SQ-PCBM BHJ Films

The absorbance spectra of $DHSQ(OH)_2$ in chloroform solution and as as-cast films are shown in Figure 3.2. The monomer absorbance is sharp and narrow (with a full width at half maximum of 0.073 eV), with a measured extinction coefficient of 1.5×10^5 cm^{-1} M^{-1} at λ_{max} of 650 nm in chloroform. The neat film absorbance shows a dramatic broadening with two peaks at 556 nm and 656 nm. This unique broadening of absorbance has been observed previously.[133,145,149,59] Here we assign this "double-hump" absorbance profile to strongly-coupled SQ aggregates. Better interpretation of the spectrum involving a deeper theoretical investigation can be found in Chapter 6. It should be emphasized here that both absorbance peaks belong to SQ aggregates and there is little monomer population in the neat films (annealing induces little change in the absorbance spectra).

$DHSQ(OH)_2$:PCBM blend films were made by spin casting chloroform solutions co-dissolving SQs and fullerenes (the blend ratio is dictated by the relative weight percent of each component). The absorbance spectra exhibit a gradual change as the fullerene loading

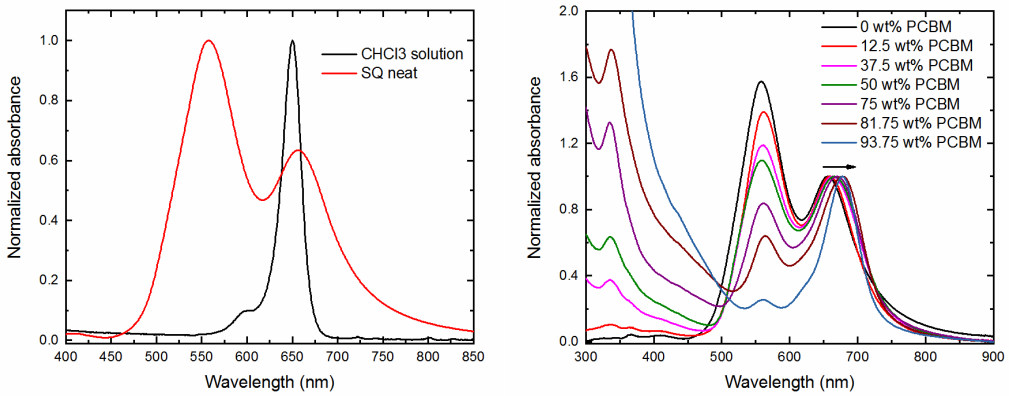

Figure 3.2 Normalized absorbance spectra of $DHSQ(OH)_2$ in dilute chloroform solution (10^{-5} M) and as thin films. Left: absorbance spectra of solution and neat films normalized to the maximum with absorbance peaks at 650nm (solution), and556 nm and 656 nm (film). Right: change in absorbance spectra of $DHSQ(OH)_2$:PCBM blend films as a function of PCBM weight ratio. The spectra are normalized to the lower energy absorbance peak. The black arrow marks the red-shift of the low energy peak as the PCBM loading is increased.

is changed as shown in Figure 3.2. First, we should note that PCBM mainly absorbs at 300 - 500 nm and thus does not significantly overlap with the $DHSQ(OH)_2$ spectra. When the weight ratio of PCBM is increased, the relative peak height at 560 nm diminishes with a concomitant red-shift in the low energy peak. In 93.75 wt% PCBM film, the peak at 678 nm dominates with an absorption "shoulder" at around 630 nm (and the peak at 560 nm is small). In such low SQ content films, the $DHSQ(OH)_2$ molecules can be viewed as "dissolved" in a PCBM solid solution. We thus assign the peak at 678 nm in 93.75 wt% PCBM film to the squaraine monomer. It is immediately noted that there is a ~ 30 nm red shift for $DHSQ(OH)_2$ monomers in blend films as compared to the solution absorbance peak. This red-shifted monomeric peak is tentatively attributed to the nonresonant interaction (i.e. gas-to-crystal shift) between $DHSQ(OH)_2$ molecules and the surrounding environments that the SQs are subjected to, i.e. PCBM vs. chloroform.[150] Indeed, SQs are

known for their strong solvatochromism effect.[107,108] Other possibilities, such as the charge transfer complexes[151] formed by $DHSQ(OH)_2$ and PCBM, though unlikely (since no evidence has been found in absorption spectra for complex formation in solution), cannot be ruled out without further investigations.

Another important observation is that the monomer absorbance in 93.75 wt% PCBM film appears broader than the solution absorbance. This broadening has been reported for SQs in Poly(methyl methacrylate) (PMMA) solid solutions and is attributed to smaller long-range intermolecular interactions (between two SQ molecules).[145] Nevertheless, this smaller interaction is dwarfed by the short-range interactions that must contribute to the formation of the more typical "double-hump" spectra. For now, we will use the term "monomer" to indicate the SQ molecules that are weakly coupled such that the absorbance spectra are similar to that of the monomer in solution, and the term "aggregate" to represent the SQ molecules that are packed densely and orderly and have a "double-hump" absorbance spectra at 560 nm and 660 nm.

Then it is easy to understand that the film absorbance peak at 660 nm is actually a composite peak consisted of $DHSQ(OH)_2$ monomers (peak at 678 nm) and the low-energy peak of the aggregates (peak at 656 nm). It is important to recognize that the resulting peak shifts depend on the relative amounts of the two species present, in accordance with the apparent peak shift observed with the addition of two Gaussian peaks with different peak positions and representing states with exchanging populations. When the monomer population is increased (by increasing PCBM weight ratio) the absorbance peak is moving towards longer wavelength.

Previously, many researchers assigned the absorbance red-shifted from the monomer

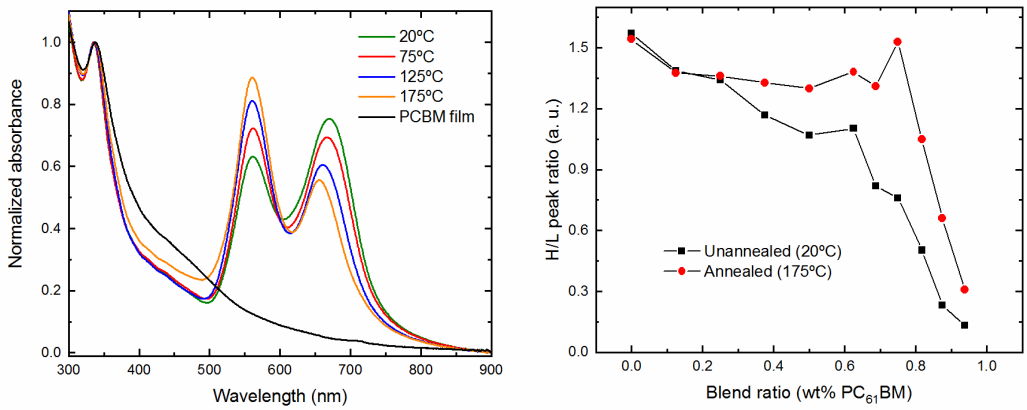

Figure 3.3 The absorbance changes in $DHSQ(OH)_2$:PCBM blend films upon thermal annealing. Left: change in absorbance spectra of the 75 wt% PCBM film as a function of annealing temperature (films were annealed for 1 min); the spectra are normalized to the PCBM absorbance peak and the absorbance spectrum of the neat PCBM film is also shown for comparison. Right: the peak ratio between high energy absorption peak at 560 nm, "H", and low energy absorption peak at 660 nm, "L", in $DHSQ(OH)_2$:PCBM pristine (black square) and annealed (red circle) films. The values of both peaks are obtained by properly subtracting the PCBM contribution. The ratio value, "H/L", represents the relative population of aggregates to monomers; i.e. when there is 100% aggregate, the "H/L" is expected to be 1.57, as for the neat SQ film. Smaller "H/L" values represent higher monomer populations present in the blend films.

in solution to the formation of J-aggregates.[59,126,149] This interpretation was rooted in the red shift relative to the monomer peak in solution. Similarly, the peak at 560 nm in neat and annealed blend films (blue-shifted relative to the monomer peak in solution) was assigned to the $DHSQ(OH)_2$ H-aggregate. Thus, the difference in solar cell performances before and after thermal annealing was sometimes correlated to the changing populations of SQ "J-aggregates" and "H-aggregates".[149] We want to emphasize that it would be hasty to assign the types of aggregates solely based on spectral shift. In the $DHSQ(OH)_2$:PCBM system, we identified two species, monomer and aggregate, each with a different absorbance spectrum.

The conversion from monomer to aggregates can be achieved through thermal

annealing as shown in Figure 3.3. Upon annealing for one minute, the blend film with 75 wt% PCBM shows a "recovery" of aggregate formation, indicated by the increase in absorption at 560 nm and a simultaneous blue-shift of the low energy features from 670 nm (at 20 ^{0}C) to 655 nm (1 min anneal at 175 ^{0}C). In 175 ^{0}C-annealed films, the absorbance mimics the neat SQ film spectrum (Figure 3.2). This again strongly supports the spectral assignment that the features at 650nm – 700 nm result from both $DHSQ(OH)_2$ monomer and aggregate contributions, and that the changes in peak position and peak ratio are caused by the interconversion of these two species.

This same annealing study was conducted through a comprehensive set of different blend ratios. The intensity ratios of the absorbance at 560 nm (high energy, or H) and 660 nm (low energy, or L), after subtraction of the PCBM contribution to each spectrum before and after annealing, are plotted against the blend ratio. For as-cast films, the "H/L" steadily decreases as fullerene wt% increases. After annealing at 175 ^{0}C for one minute, the "H/L" increases to almost the same value as for the neat SQ films, as long as the weight ratio of PCBM is below 80 wt%. Above this threshold, the aggregate formation upon annealing is retarded by the overwhelming amount of fullerenes.

In summary, $DHSQ(OH)_2$ neat films demonstrate the effects of fast aggregation during the spin casting process but, in the high presence of PCBM, transfer of an amorphous, more homogeneous mixture to the film dominates and aggregation is disrupted. The disruption of the aggregation and the relative population of monomer and aggregate correlate well with the percentage of the fullerene present in the films. We consider that upon spin casting from a low boiling point solvent (such as chloroform), the homogeneous mixture of the solution is partially transferred to the film such that the blends are well mixed. When

thermally activated, the $DHSQ(OH)_2$ monomers start to aggregate in the solid films. A large interconversion between monomers and aggregates was seen in films with a range of 40 wt% to 80 wt% PCBM. This change in $DHSQ(OH)_2$ species population is expected to impact the film crystallinity and BHJ morphology.

3.3 Impact of SQ Aggregation on BHJ Morphology

For better connection between $DHSQ(OH)_2$ aggregation and OPV device efficiency, we investigated the morphological change of the films during annealing. With a large phase separation, the surface area of the donor-acceptor interface shrinks and the distance requires for exciton diffusion to the interface increases, leading to a reduced charge generation. On the other hand, high crystallinity is considered to be beneficial for exciton diffusion rate and charge capture. When the dipole orientation factor of donor and acceptor is large, the Förster Resonance Energy Transfer (FRET) is efficient.[152] The dipole orientation factor is large in a highly ordered crystal material, and is small in an amorphous state with randomized dipole alignments.[145] Hence exciton diffusion rates are enhanced in ordered materials. Increased charge transfer integrals between ordered molecules would also indicate more efficient frontier orbital overlap and improved mobility. Reduced bimolecular charge recombination will result leading to improved device performance.[142] The $DHSQ(OH)_2$:PCBM BHJ morphologies at different donor acceptor weight ratio and upon thermal annealing as investigated by using XRD, TEM and DSC.

3.3.1 Change of film crystallinity with SQ aggregation

The film crystallinity was investigated by thin film XRD. The experimental set up was

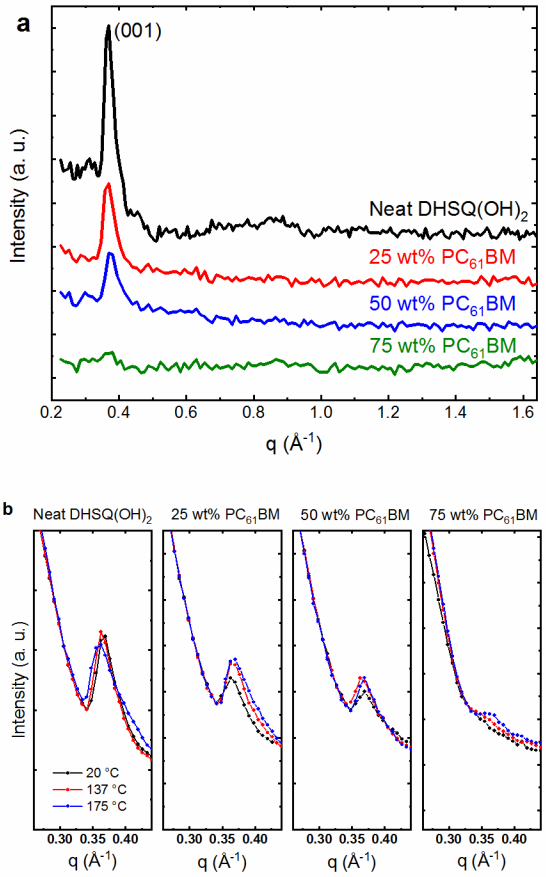

Figure 3.4 X-ray diffractograms recorded for $DHSQ(OH)_2$:PCBM films (a) at different blend ratios in pristine films and (b) as a function of thermal annealing. The films were prepared by spin coating $DHSQ(OH)_2$ or $DHSQ(OH)_2$:PCBM blend solutions with 0 wt% (neat SQ), 25 wt%, 50 wt% and 75 wt% PCBM onto a glass substrate. After XRD measurements of the pristine films, they were then subjected to thermal annealing at 137 ^{0}C and 175 ^{0}C, respectively, for 3 min. The main diffraction peaks for various blend ratios are located at $2\theta = 5.2$, which corresponds to the (001) plane in the single crystal structure. The dwell time for data acquisition is 2 s for all films except the 75 wt% films, in which 8 s dwell time was used to resolve the peak structure.

introduced in Section 2.6. For SQ neat films in Figure 3.4a, one diffraction peak is observed at q = 0.37 Å^{-1} (or $2\theta = 5.2^0$) in good agreement with the 001 plane calculated from the single crystal structure of $DHSQ(OH)_2$.[153] This diffraction peak is sharp and narrow, confirming that the squaraine is are highly crystalline. As the amount of PCBM is

increased, the intensity of the diffraction peak diminishes and broadens, suggesting a decrease in crystallinity in those films. For the 75 wt% PCBM film, the weak diffraction peak is approaching the limit of our experimental resolution. For all blend films, no diffraction peaks were identified for PCBM, indicating that the fullerene molecules were essentially amorphous in the BHJ films.[154]

The crystal peak at q = 0.37 $Å^{-1}$ increases in relative intensity by thermal annealing (Figure 3.4b). This correlates very well with the spectral change and confirms that the $DHSQ(OH)_2$ aggregates are associated with crystallites. The diffraction peak intensity of neat $DHSQ(OH)_2$ films is independent of the annealing temperature, indicating that the $DHSQ(OH)_2$ molecules are already crystallized during spin casting. Overall, the consistent observation in absorbance spectra and XRD results demonstrates that the $DHSQ(OH)_2$ crystallization is the driving force for phase separation and aggregation

3.3.2 SQ-PCBM phase separation upon annealing

Beyond the increase in extent of crystallinity throughout the films, a separate issue is the increase in crystal domain size and the phase separation, also important for OPV performance.[75,88,155–157] Here, we go on to consider phase separation through a differential scanning calorimetry (DSC) study. The samples are prepared by spin casting the solution (with different blend ratios) onto glass petri dishes and then scraping the solids off with a razor blade. The materials obtained in this way are analogous to the BHJ films in OPV devices. During the DSC measurements, the samples are 1) heated from 50 ^{0}C to 260 ^{0}C, and then 2) cooled to below 75 ^{0}C, and again 3) heated back up to 350 ^{0}C. The DSC thermograms recorded for each step are shown in Figure 3.5.

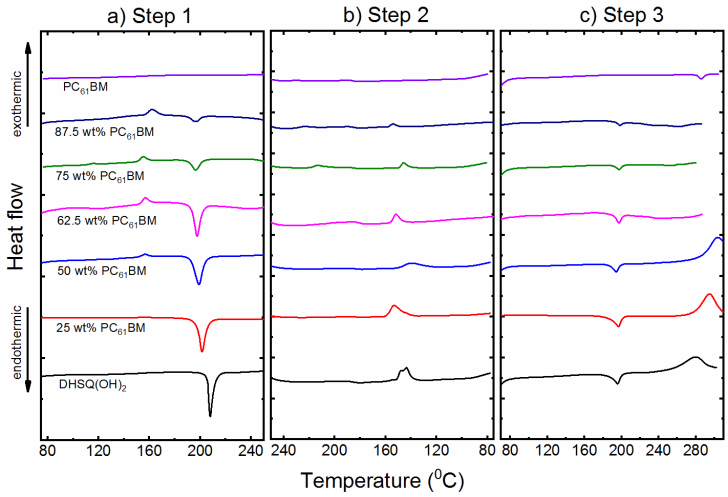

Figure 3.5 The DSC heating and cooling thermograms of $DHSQ(OH)_2$: PCBM bulk heterojunction blends of different compositions. The samples were heated from room temperature to 260 ^{0}C (a, step 1), then cooled to below 75 ^{0}C (b, step 2), and finally heated back to 350 ^{0}C (c, step 3). The exothermic and endothermic peaks are normalized to the mass of the solids.

During step 1 for each blend ratio, separate exothermic and endothermic features are observed respectively at 155 ^{0}C-165 ^{0}C and 194 ^{0}C-208 ^{0}C. The endotherms correspond with the melting point of $DHSQ(OH)_2$, consistent with the literature.[158] The exothermic peak is associated with the SQ-fullerene phase separation because i) it is only observed in the blend films, and increases in intensity with PCBM content; ii) it is not observed in step 3 as the phase separation is assumed to be complete at the end of step 1. It should be noted that the highest temperature for step 1 is delicately set below the melting point of PCBM (at 290 ^{0}C, identified by the small endothermic peak in 100 wt% PCBM film in Figure 3.5, step 3) to eliminate the possibility of DHSQ(OH)2 and PCBM remixing in their liquid-liquid phase.

In the cooling step (step 2), the peaks at 135 ^{0}C-150 ^{0}C are assigned to the $DHSQ(OH)_2$ crystallization exotherms from the melt. In step 3, the endotherms at 190-200 ^{0}C belong to

the re-melting of $DHSQ(OH)_2$. We note that the endotherms in this step are decreased (< 12 ^{0}C) compared to the melting point in the step 1. The shift itself is not fully anticipated but is consistent with a gradual decomposition of the SQ during the process. This observation is also consistent with the thermal decomposition temperature measured by Tian *et al.*[158] Substantial degradation of $DHSQ(OH)_2$ was found at 280 ^{0}C in step 3, where the large exothermic peak was found. The PCBM does not show any decomposition below 400ºC based on an evaluation of the material mass through DTA/TGA.

In summary, DSC results help us to identify the $DHSQ(OH)_2$ crystallization endotherm at 135 ^{0}C-150 ^{0}C and the SQ fullerene phase separation exotherm at 155 ^{0}C-165 ^{0}C. We subsequently investigate the phase separation and BHJ morphology through TEM at two key temperatures: 137 ^{0}C, a point just upon the recrystallization endotherm but below the phase separation exotherm, and 175 ^{0}C a point well above the phase transition exotherm but below the melting point of $DHSQ(OH)_2$.

3.3.3 Change of phase separation with SQ aggregation

Wei *et al.* have measured the exciton diffusion length of a SQ molecule sample to be 1-5 nm.[121] Thus, an optimal domain size of SQ donors is estimated to have a diameter of ~10 nm. Here, we use TEM to investigate the domain size and compare it to the SQ exciton diffusion length.

In TEM micrographs (Figure 3.6), the dark areas are assigned to the PCBM-rich domains and the light areas are assigned to the SQ-rich domains. The origin of the contrast in the TEM images is ascribed to the density difference between SQ (ρ = 1.22 g cm^{-3} as measured for SQ single crystals and considered the upper limit for the density of SQ films[153]) and PCBM (ρ = 1.5-1.6 g cm^{-3})[55,159,160] and $\rho = 1.22$ g cm^{-3}. Thus, the bright

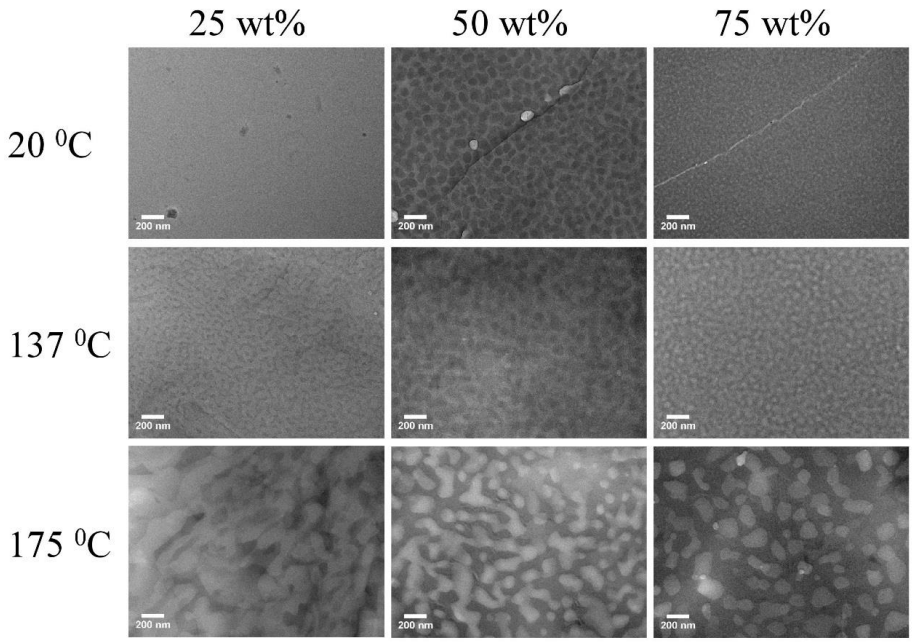

Figure 3.6 TEM micrographs of spin-cast DHSQ(OH)$_2$:PCBM films without treatment (top) and annealed at 137 ^{0}C (middle) and 175 ^{0}C (bottom) for 3 min. The blend ratios under study are from left to right: 25 wt%, 50 wt% and 75 wt% of PCBM. The scale bar at the bottom of each image is 200 nm. The crack lines in some images are only for focusing the objective lenses of the TEM.

phases are assigned to the SQ-rich domains and the dark phases are PCBM-rich domains, due to the relatively higher electron scattering density of PCBM as compared to SQs.

In the TEM image of unannealed films (Figure 3.6, top panel), the composites appear to be well mixed. For 25 wt% PCBM, the fullerene phase cannot be distinguished from the SQ aggregate phase (the black dots are assumed to be defects in the films). In 50 wt% PCBM films, SQ and fullerene phases can be seen with an estimated size of 100-200 nm in diameter. Such domains, if chemically pure, are considered too large as compared to the exciton diffusion length of SQs. In 75 wt% PCBM films, small and fine phases are formed. We infer from the 50 wt% sample that these two compounds are chemically incompatible

and phase separate when mixed evenly. This is consistent with thermodynamically driven phase separation observed in DSC. UV-Vis absorption showed that even in 75 wt% PCBM films, the squaraine aggregates still exist in a high population but, given these TEM images and our XRD data, the crystalline domains formed in such films are small in size (< 50 nm in diameter), assuring a high donor acceptor interfacial area.

Annealing at 175 ^{0}C induces a dramatic phase separation for all films independent of the blend ratio. At a slightly lower annealing temperature, 137 ^{0}C, the phase separation was not as profound as for the 175 ^{0}C annealed films, as hypothesized. This is because the annealing temperature is below the critical phase separation temperature characterized by DSC. Given the increase in aggregate absorption in UV-Vis spectra (Figure 3.3) and the increase in X-ray diffraction peak (Figure 3.4) after annealing at 137 ^{0}C, the extent of crystallinity is increased while further phase separation is minimized leading towards an optimized morphology for OPV device operation.

3.4 Organic Solar Cells Based on DHSQ(OH)$_2$:PCBM BHJ

The OPV cells have been fabricated using SQ and PCBM in a device structure of ITO/PEDOT:PSS/SQ:PCBM BHJ/Al. The BHJ active layer was deposited by spin casting chloroform solution with varying SQ to PCBM ratios with a fixed squaraine concentration of 4 mg mL^{-1}. The active layers were annealed at 137 ^{0}C or 175 ^{0}C for 30 seconds, and the device results are compared to unannealed devices. The device parameters are listed in Table 3.1.

Upon increasing the PCBM ratio from 25 wt% to 75 wt%, the power conversion efficiency increased from 0.15% to 0.98%, corresponding to a 6-fold improvement. This is

Table 3.1 The device performances of $DHSQ(OH)_2$: PCBM at different blend ratios with and without thermal treatments.

Blend ratio	Thermal treatment	Device parameters			
		J_{SC} (mA/cm^{-2})	V_{OC} (V)	FF	PCE (%)
3:1	None	1.95 ± 0.32	0.29 ± 0.06	0.27 ± 0.07	0.15 ± 0.05
	175 ^{0}C	0.2	0.02	0.07	0.00 (diode)[a]
1:1	None	4.15 ± 0.15	0.53 ± 0.05	0.39 ± 0.03	0.86 ± 0.12
	137 ^{0}C	3.84 ± 0.22	0.55 ± 0.04	0.43 ± 0.05	0.92 ± 0.19
	175 ^{0}C	0.54	0.15	0.26	0.02 (diode)[a]
1:3	None	4.69 ± 0.30	0.52 ± 0.06	0.40 ± 0.06	0.98 ± 0.19
	137 ^{0}C	4.64 ± 0.21	0.59 ± 0.07	0.45 ± 0.06	1.24 ± 0.26
	175 ^{0}C	1.08	0.18	0.26	0.06 (diode)[a]

[a] the devices showed diode behavior and the parameters can hardly be obtained and thus are considered imprecise (with no standard deviation provided).

attributed to the large heterojunction interface provided by the finely mixed donor and acceptor phase at high fullerene content and the associated higher electron mobility for high volume-percentage PCBM.[143] Upon 175 ^{0}C annealing, the well mixed phases separate into large chemically pure domains, as shown in the TEM images (Figure 3.6), which leads to the diode like behavior and a tremendous deterioration of device efficiency.

When annealed at 137 ^{0}C, the low temperature onset of the crystallization exotherm of $DHSQ(OH)_2$ obtained from DSC thermograms, the device performance improves from 0.86% to 0.92% for the 1:1 blend and from 0.98% to 1.24% for the 1:3 blend. The increased device efficiency mainly stems from the improved open circuit voltage and fill factor. The short circuit current, however, stays the same or even slightly decreases after annealing. This is counterintuitive given that film crystallinity increases without any detrimental phase

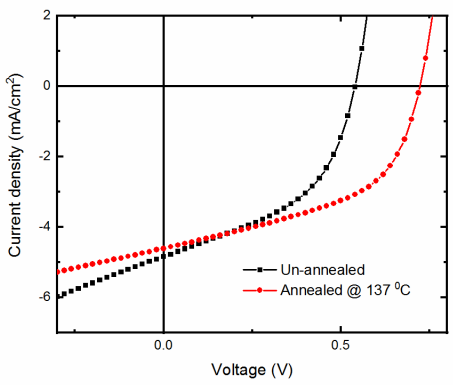

Figure 3.7 Current-Voltage characteristics of DHSQ(OH)2:PCBM BHJ devices before and after thermal treatment. The solar cell parameters for best unannealed devices: Jsc = 4.84 mA cm^{-2}, Voc = 0.54 V, FF = 46.6%, PCE = 1.22%; the solar cell parameters for best annealed devices: Jsc = 4.61 mA cm^{-2}, Voc = 0.72 V, FF = 49.9%, PCE = 1.66%.

separation, as demonstrated by XRD and TEM. The reason for unimproved J_{SC} is considered to be related to the LUMO energy level shift upon aggregation. The J-V characteristics of the champion as-cast and annealed solar cells are shown in Figure 3.7, with the solar cell parameters listed in the figure caption. It is immediately seen that the annealed device yielded a better Voc compared to the as-cast solar cells. This improvement in Voc is not well understood.

In previous studies of squaraine materials in OPV devices, the same strategies employed to optimize solar cells, such as thermal annealing, do not always lead to the same resulting device efficiency. It has been reported that improving crystallinity of the SQ films by thermal annealing[121,126] and solvent annealing[41] results in an optimized solar cell performance. Our group has found a decrease in the device efficiency after thermal annealing[69] and, in this case, we assign this to the significant DHSQ(OH)$_2$:PCBM phase separation at high annealing temperatures. The domain size after phase separation is estimated to be 50-200 nm in diameter, comparable to the expected thickness of the films.

Extensive phase separation will lead to loss of PCE but mixing can be controlled through rapid evaporation of spin-casting solvent and dilution by PCBM. The increase in efficiency resulting from higher PCBM blend ratios therefore has a different origin to the increase in efficiency described elsewhere,[40,41,126] associated with conducting PCBM networks.

The phase separation of small squaraine molecules when mixed with fullerenes is unique when compared to polymers. It has been reported that the P3HT and PCBM are essentially miscible in the films[143,144]. In our study, we found that the phase separation happened with no limitation. This suggests that the optimization strategy of squaraine based OPV devices should be different from that of polymer based devices. In particular, based on our work, we suggest that more attention should be paid to the phase separation during fabrication. Thermal annealing, solvent annealing and use of solvent additives remain important since these processing parameters allow some control over intrinsic factors like crystallinity and chemical incompatibility.[144]

3.5 Discussion

In this chapter we demonstrated the successful application of a squaraine molecules, $DHSQ(OH)_2$, in OPV devices. The power conversion efficiency obtained from optimizing BHJ morphology is 1.24 ± 0.26 %, with a champion efficiency of 1.66 % (Jsc = 4.61 mA/cm^2, Voc = 0.72 V, FF = 50%). The device efficiency is improved by over 25 % regarding to the unoptimized devices.

Specifically, in $DHSQ(OH)_2$:PCBM BHJ solar cells, we recognized a mixed population of squaraine monomer and aggregate. The relative population can be tuned by changing the SQ:PCBM blend ratio and thermally annealing the films. We demonstrated

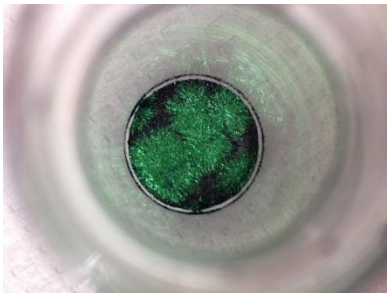

Figure 3.8 A photograph of $DHSQ(OH)_2$:PCBM film formed in the bottom of a scintillation vial by slow evaporation of chloroform solvent. The green snowflake-like fibers are SQ crystals and the black amorphous material in between the SQ crystals is the pure PCBM clusters.

that the SQ aggregate is associated with crystalline structure and infer a subsequent benefit for charge transport in the BHJ. On the other hand, thermal annealing can induce extensive phase separation, leading to domain sizes much larger than the exciton diffusion length. The optimal device performance can be achieved the mid-way between mixing and phase separation, where the crystallinity of the film is improved without initiating the formation of large and pure domains. This can be done by first blending SQ with a high content of PCBM to form a mixing morphology, and then by annealing such films at a carefully chosen temperature and annealing time to allow SQ to aggregate/crystallize into small and interconnected domains. We then demonstrate a correlation between BHJ morphology and device efficiency, which can serve as a guideline for characterizing new SQ materials and optimizing their photovoltaic performance.

We found that the $DHSQ(OH)_2$ and PCBM completely phase separate under slow evaporation of chloroform, leaving fiber-like snowflake-shaped SQ crystals with PCBM domains filling the rest of the space (Figure 3.8). During this slow evaporation process over a month, the system moves towards a well-established, thermally equilibrated and large-scale phase separation.

We note that the power conversion efficiency of our devices is low. The OPV device performance can be optimized by inserting an electron transporting or exciton blocking layer, such as bathocuproine (BCP) [59,123], by replacing the PEDOT:PSS layer with materials with better energy matching, such as MoO_3 [121,126] and by replacing PCBM with $PC_{71}BM$, which absorbs more efficiently in the visible spectrum [153]. We will address this issue in the next chapter.

Chapter 4. IMPACT OF ALKYL CHAIN LENGTH ON BHJ MORPHOLOGY AND SOLAR CELL PERFORMANCE

In this chapter, we have investigated a series of aniline based squaraines (SQs), with varying solubilizing alkyl chains, as donor materials in bulk heterojunction (BHJ) solar cells. Although these squaraine molecules exhibit similar absorbance spectra and crystal structure, the difference in properties that drive the OPV performance becomes apparent when blending each squaraine with PCBM. Disruption of SQ aggregation is observed with the presence of PCBM, more so for the shorter side chain SQ. As a result, the shorter side chain SQs exhibit a large drop in hole-mobilities of the BHJ films as compared to their neat films, whereas the mobility decreases for the longer side chain counterparts are small. However, morphological studies have shown that the phase separation rapidly happens during the spin casting process for the longer side chain SQs. Ultimately it is the extent of phase separation that dominates the final device efficiency. After device optimization, our best performing SQ yields a champion cell efficiency of 5.6%.

4.1 Introduction

The alkyl groups attached to the rigid conjugated units in small molecule or polymeric materials are mainly for promoting their solubility in common organic solvents. Recently, modification of alkyl side groups has been shown to be an effective way to control the crystallization of the polymers and small moelcules.[81–83,161] In a previous work by Nguyen *et al.*, a further increase in alkyl side groups in polymers, for example to octyl (i.e. P3OT) and decyl (i.e. P3DT), was found to significantly aggravate the phase separation and led to unsatisfactory morphology and device efficiency.[81] Gadisa *et al*. studied the effect of alkyl side chain length of poly(3-alkyl thiophene) (P3AT), specifically with butyl (i.e. P3BT), pentyl (i.e. P3PT) and hexyl (i.e. P3HT) side chains, on morphology and charge transport in P3AT:PCBM BHJ.[82] The results showed that the P3HT:PCBM BHJ, with a higher degree of phase separation, has a more balanced bipolar charge transport in BHJ and thus a better device performance.

Successful OPV application of SQ molecules is at least partially related to their ability to aggregate or crystallize in thin films either upon spin casting or after subsequent annealing treatment. Highly crystalline SQ films lead to a significant increase in exciton diffusion length and charge mobility, and thus improved power conversion efficiency (PCE). For example, Wei *at el*. has reported an increase in exciton diffusion length of SQ by a factor of 3 after thermally annealing the DiBSQ(OH)$_2$ thin films before C_{60} and aluminum cathode deposition.[121] For solution processed bulk heterojunction (BHJ) cells using DiBSQ(OH)$_2$, the cell PCE was significantly increased by over 100% after solvent vapor annealing (SVA) in dichloromethane (DCM) vapor.[41] In some previous studies, however, a decrease in device PCE was found after thermal annealing for some other

SQ:PCBM systems, in which the only molecular structure difference of our SQs as compared to DiBSQ(OH)$_2$ is the choice of side chains.[69,145] In Chapter 3, we pointed out that the efficiency roll-off of our SQ:PCBM BHJ solar cells is due to over-developed phase separation. Therefore, controlling donor acceptor phase separation is critical for highly efficient SQ:PCBM based solar cells.

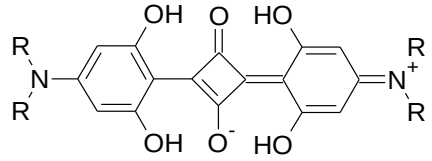

SQ

R = n-propyl, *n*-butyl, *n*-pentyl, or *n*-hexyl

Figure 4.1 Molecular structure of a series of aniline based SQ molecules. R = n-propyl, n-butyl, n-pentyl and n-hexyl for DPrSQ(OH)$_2$, DBSQ(OH)$_2$, DPSQ(OH)$_2$ and DHSQ(OH)$_2$ respectively.

In the present chapter, we study the influence of solubilizing alkyl side groups on hole mobility, film crystallinity, phase separation and, subsequently, solar cell performance of SQ:PCBM BHJ. A series of aniline based SQ molecules with n-propyl (i.e. DPrSQ(OH)$_2$), n-butyl (i.e. DBSQ(OH)$_2$), n-pentyl (i.e. DPSQ(OH)$_2$) and n-hexyl (i.e. DHSQ(OH)$_2$) carbon chains (Figure 4.1) were synthesized according to the procedure described previously.[136] The first three SQs are needle-like shiny crystals, while DHSQ(OH)$_2$ is a fiber-like dull solid.

These SQ molecules show very similar properties in solution and as neat films, as they share the same conjugated backbones and the same crystal packing motif. However, we observe different degrees of aggregate disruption in as-cast SQ:PCBM blend films; for SQs with longer alkyl groups, the aggregation is less disrupted in the presence of fullerenes,

leading to a higher degree of film crystallinity. Subsequently, the phase separation is more profound for SQs with longer alkyl chains. As a result, OPV performance is in the order of $DBSQ(OH)_2$ > $DPSQ(OH)_2$ > $DHSQ(OH)_2$. The low efficiency of devices employing $DHSQ(OH)_2$ is related to its non-optimal BHJ nanomorphology with extensive phase separation, while the best performing BHJ of $DBSQ(OH)_2$:PCBM is essentially a uniform mixing of two components.

Although hierarchical phase separation and polymer crystallization has often been considered as critical to achieve high efficiency in polymer/fullerene solar cells,[75,155] our observations suggest a different case for SQ based OPV. Thin film X-ray diffraction studies have demonstrated that the best performing $DBSQ(OH)_2$:PCBM BHJ films are essentially amorphous. This is likely due to the smaller (when compared to polymers) exciton diffusion length, L_d = 1~5 nm,[121,124] measured in typical SQ films; efficient exciton dissociation cannot be achieved once the domain size is above this value. Our work has shown that longer side chain length (from butyl to hexyl) will exacerbate the phase separation between squaraine donors and fullerene acceptors in spin-cast BHJ films, leading to a large decrease in solar cell performance. Although the trend is readily seen that the shorter side groups would be beneficial to achieve optimal BHJ morphology when blended with fullerenes, we want to emphasize that the alkyl side groups must be sufficiently long to enable a good solubility of squaraine in conventional organic solvents. $DPrSQ(OH)_2$, for example, has limited solubility of 3 mg/mL in chloroform, which renders a low film quality through solution casting processes.

4.2 Single Crystal Structures

The single crystal structures of this series of aniline based SQ molecules feature a common "slip stack" packing motif. The crystal structure of a representative SQ, $DBSQ(OH)_2$, is shown in Figure 4.2. The crystal system is triclinic with the *P*-1 space group. The molecular backbone (i.e., phenyl-squarylium-phenyl) is planarized by intramolecular hydrogen bonds between the phenyl ring hydroxyl groups and the squaric core oxygens. The slip stack structure comfortably fits the long N-alkyl molecular arms and, at the same time, enables short interplanar spacing.

The cartoon in Figure 4.2b illustrates one way to quantify this slip stack structure using artificial Cartesian coordinates. The y-axis is defined by the molecular long axis on which are located the two nitrogen atoms (blue dots), the x-axis is defined by the short axis on which are located the two squaric oxygen atoms (red dots). The z-axis is perpendicular to

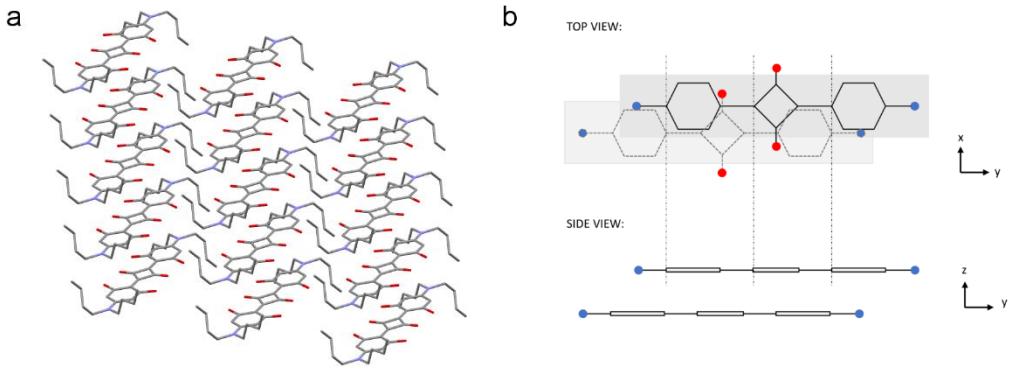

Figure 4.2 Single crystal structures of aniline SQs with linear alkyl side groups. **a)**: Molecular packing of $DBSQ(OH)_2$ single crystal, featuring a π-π stacking with slippages in both long and short molecular axes; other SQs adopt a similar slip stacking motif in the single crystal. **b)**: a simple cartoon illustrates the slip stack of the SQ molecules with an artificial Cartesian coordinate; x and y axes are along the short and long molecular backbones respectively, so the z axis is perpendicular to the parallell π-stacked molecular planes. Red dots represent oxygen atoms on the squaric acid moiety and blue dots are nitrogen atoms to which the alkyl groups attached (omitted).

the xy plane. In this way, the small differences in crystal structure of three SQs can be quantified and the results are summarized in Table 4.1, along with the unit cell dimensions. Overall, the difference in π-π stacking distance, Δz, is less than 0.1 Å and the differences in slips in x and y axes, Δx and Δy, are less than 0.2 Å.

Table 4.1 Single crystal structure data for aniline based SQ molecules with linear alkyl chains. The unit cell dimensions for $DPrSQ(OH)_2$, $DBSQ(OH)_2$, $DPSQ(OH)_2$ and $DHSQ(OH)_2$ single crystals are listed, along with the calculated slippages in the short and long molecular axes (i.e. Δx and Δy respectively) and π-π interplanar distances (Δz).

Compound	a / Å	b / Å	c / Å	Δx / Å	Δy / Å	Δz / Å
$DPrSQ(OH)_2$[42]	5.215(2)	10.894(4)	11.156(5)	1.848	3.579	3.318
$DBSQ(OH)_2$[42]	5.169(4)	10.846(9)	13.538(11)	1.879	3.470	3.353
$DPSQ(OH)_2$	5.227(2)	10.694(4)	15.412(5)	1.688	3.621	3.371
$DHSQ(OH)_2$[50]	5.097	10.746	16.604	1.734	3.498	3.276

4.3 Impact of Alkyl Chain on SQ Aggregation

All three SQs share typical absorbance spectra in solution and films, as shown in Figure 4.3. The absorption spectra of these squaraine monomers in solution overlap with each other, sharing a stronger 0-0 transition at 650 nm ($\varepsilon = 3 \sim 4 \times 10^5$ M^{-1} cm^{-1}) and a weak 0-1 transition at 600 nm. The similar absorption profile in chloroform solutions is due to the shared molecular conjugated backbone unit. The alkyl side groups do not perturb the electronic structures of the individual molecule. The absorption spectra of squaraine

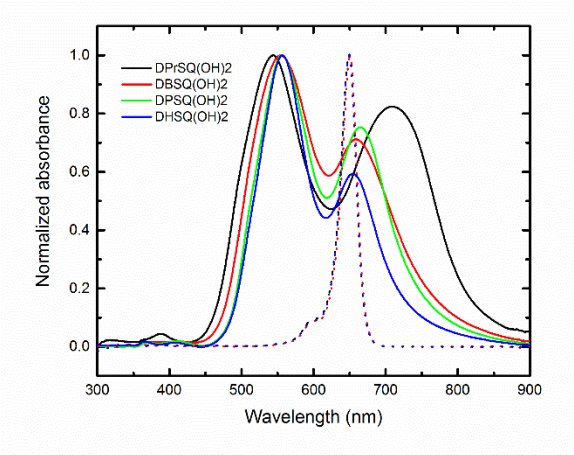

Figure 4.3 Normalized absorbance spectra of three SQs in chloroform solution (dashed line) and as neat films (solid line). The absorbance spectra for all three solutions overlap each other with the same peak position. The SQ neat films are annealed at 90 ^{0}C for 5 min to ensure a complete aggregation of SQ molecules.

films are also similar to each other with a "double-hump" shape and the two peaks are at 550 nm and ~ 660 nm. Noticeably, DPrSQ(OH)$_2$ has a larger low-energy band which red-shifted to ~730 nm. This is due to the strong coupling to intermolecular charge transfer state (will be discussed in Chapter 6). The red-shifted peak and broader absorption profile might benefit the light harvesting properties. However, the low solubility of this squaraine limit its practical application in solution-processed solar cell devices.

After annealing the neat films at 90 ^{0}C, the absorbance spectra do not change for DPSQ(OH)$_2$ and DHSQ(OH)$_2$; but for DPrSQ(OH)$_2$ and DBSQ(OH)$_2$, the absorption changes a little with further splitting between the peaks (Figure A1). This change in absorbance indicates that DBSQ(OH)$_2$ may have re-arranged itself in a tighter crystal packing structure under annealing. The lack of significant spectral change upon annealing for DPSQ(OH)$_2$ and DHSQ(OH)$_2$ indicates that the crystallization may be immediately

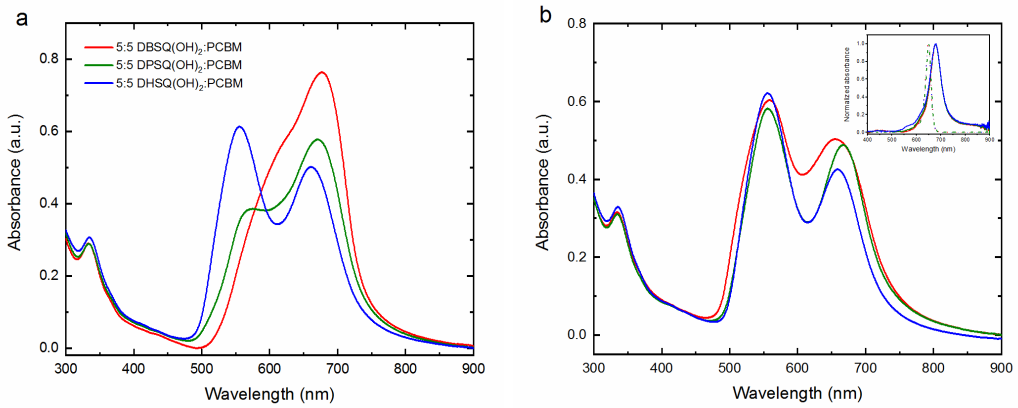

Figure 4.4 Normalized absorbance spectra of three SQs in SQ:PCBM (1:1 w/w) blend films. **a**): as-cast films show different absorption spectra with SQs of different side chain lengths.**b**): absorbance spectra of the blend films after annealing at 90 ^{0}C for 5 min. **b**) inset: SQ monomer absorbance peak in 98 wt% PCBM, with dashed lines representing the absorption spectra of SQ monomer in solution for comparison.

complete after spin casting. Overall, the neat film absorbance spectra of all three SQs are very similar, which undoubtedly results from the shared molecular backbone, as well as the similar crystal packing motif.

Except for DPrSQ(OH)$_2$, the solubilities of all SQs studied here, in chloroform, are > 24 mg/mL. The low solubility (3 mg mL^{-1}) of DPrSQ(OH)$_2$ significantly limits its practical application in solution processes. Thus, the later discussion will be mainly focused on the other three DBSQ(OH)$_2$, DPSQ(OH)$_2$ and DHSQ(OH)$_2$.

In contrast to the similar absorbance spectra of solution and neat films in Figure 4.3, the absorbance spectra of as-cast SQ:PCBM blend films are distinct from each other. The absorbance spectra of SQ:PCBM blend films with the weight ratio of 1:1 is shown in Figure 4.4a. Here PCBM is used instead of PC$_{71}$BM to open the optical window (500-750 nm) through which the absorbance of SQ aggregates can be clearly seen. DBSQ(OH)$_2$ shows a

disruption of aggregation in the presence of 50 wt% PCBM, as evidenced by a loss of the double hump and a peak emerging at 677 nm, similar to the peak at 678 nm of the (monomer) blend films with 2 wt% of SQ (Figure 4.4b inset). But if one compares these two spectra, the SQ absorbance peak in the 50 wt% PCBM films is broader than that in 98 wt% PCBM films, with a distinguishable "shoulder" at 600 nm. This shoulder decreases as the PCBM weight ratio is increased and, therefore, it is ascribed to the weak interaction between SQ molecules in the SQ:PCBM blend films. On the other hand, the $DHSQ(OH)_2$:PCBM blend film exhibits an absorbance spectrum similar to that of the neat film, indicating the aggregates are formed completely. Interestingly, for the $DPSQ(OH)_2$:PCBM blend film, an intermediate spectrum is exhibited, with a distinguishable aggregate double hump as well as a monomer absorption feature.

Similar absorbance spectra were observed for other blend ratios, from 5:5 to 2:8. Specifically, $DBSQ(OH)_2$ aggregates are completely disrupted throughout different blend ratios (with the absorbance "shoulder" decreasing as the PCBM ratio increases), $DPSQ(OH)_2$ shows absorbance spectra indicating mixtures of aggregate and monomer and the aggregates of $DHSQ(OH)_2$ are gradually disrupted by increasing the weight ratio of PCBM, but a significant amount of aggregates are still formed in a 2:8 SQ:PCBM blend ratio. Even in 2:98 blend ratios, a small DHSQ(OH)2 aggregate absorbance peak at 550 nm can clearly be observed in the spectrum (Figure 4.4b inset). Thus, SQ aggregate formation, when blended with PCBM, is favored by longer alkyl side groups.

Upon annealing the SQ:PCBM films at 90 ^{0}C for 5 min, the absorbance spectra of all three blend films start to resemble those of the neat films, as seen in Figure 4.4b, with the biggest spectral change being observed for the $DBSQ(OH)_2$:PCBM blend. This spectral

change suggests i) there is a significant amount of initial disorder of $DBSQ(OH)_2$ and $DPSQ(OH)_2$ molecules in the as-cast blend films and ii) these SQ molecules can easily self-assemble or aggregate in films upon thermal annealing.

Figure 4.4a and b are explained as follows. The disruption of aggregation in as-cast $DBSQ(OH)_2$:PCBM blends is due to the rapid loss of the solvent environment during spin casting with the materials being frozen into a kinetically stable mixed state, not too dissimilar to the homogeneous solution phase. $DPSQ(OH)_2$ and $DHSQ(OH)_2$, however, manage to form ordered structures (i.e. aggregates) in the blend films even during spin casting.

4.4 Impact of Alkyl Chain on BHJ Morphology

Due to such differences in aggregation for these three SQ molecules when blended with PCBM, the heterojunction blends are expected to have varying film crystallinity, hole mobility properties, film morphologies and subsequently different organic photovoltaic performances. In morphology characterizations, the SQ:PCBM blend ratio is fixed at 5:5 w/w. This is to maximize the contrast between these different materials, although higher PCBM weight ratio would decrease the phase separation and film crystallinity, resulting in higher device performances, especially for $DHSQ(OH)_2$ (as demonstrated in Chapter 3).

4.4.1 Crystallinity of neat and BHJ films

In the XRD study, the films were prepared by spin casting neat SQ solutions or SQ:PCBM solutions onto MoO_3 treated ITO substrates, resembling the condition of the films prepared for hole-only and solar cell devices. The XRD patterns of ITO/MoO_3

substrates were recorded and weak diffraction peaks of the ITO layer were identified at $2\theta = 21.5^0$ (corresponding to the (2 1 1) plane), $2\theta = 30.6^0$ (corresponding to the (2 2 2) plane) and $2\theta = 35.5^0$ (corresponding to the (4 0 0) plane)[162]; no diffraction peaks were identified for the thin MoO_3 layer (thickness = 8 nm). Besides these peaks, the crystalline SQ diffraction peaks of neat and blend films are found at $2\theta = 5^0 \sim 6^0$ for all three SQs. This is expected since all SQs share the same crystal packing motif (Figure 4.2).

In thin film XRD patterns of neat SQ films (Figure 4.5), the SQ crystalline structures can be identified with a sharp peak at $2\theta = 6.01^0$, 5.68^0 and 5.01^0 for thermally annealed $DBSQ(OH)_2$, $DPSQ(OH)_2$ and $DHSQ(OH)_2$ neat films, respectively. The $DHSQ(OH)_2$ neat film pattern also features a small peak at $2\theta = 9.91^0$, suggesting a higher degree of crystallinity of this SQ in spin-cast films. It should be mentioned that for $DBSQ(OH)_2$ and $DPSQ(OH)_2$, similar diffraction peaks of $2\theta \approx 9\text{-}10^0$ are also observed but with a much lower intensity. The diffraction peaks at $2\theta = 5^0 \sim 6^0$ are close in position with the (0 0 1) plane powder diffraction peak, calculated based on SQ single crystal structures. The rest of the diffraction peaks are lost in the background due to the thin nature of the films.

Given that for $DHSQ(OH)_2$, the peak intensity is greatest and full width at half maximum (FWHM) is the narrowest, we conclude that $DHSQ(OH)_2$ neat films exhibit the highest level of crystallinity. The as-cast $DPSQ(OH)_2$ neat films are also highly crystalline. The thermal annealing does not significantly change the intensity and shape of the diffraction peaks of these two SQ neat films, consistent with the observation in absorbance spectra after annealing. The XRD patterns of as-cast $DBSQ(OH)_2$ neat films only show a very weak XRD peak at $2\theta = 6.01^0$ and multiple shoulders at $2\theta = 7^0 \sim 8^0$, consistent with the as-cast $DBSQ(OH)_2$ neat films being more amorphous. A more crystalline film is

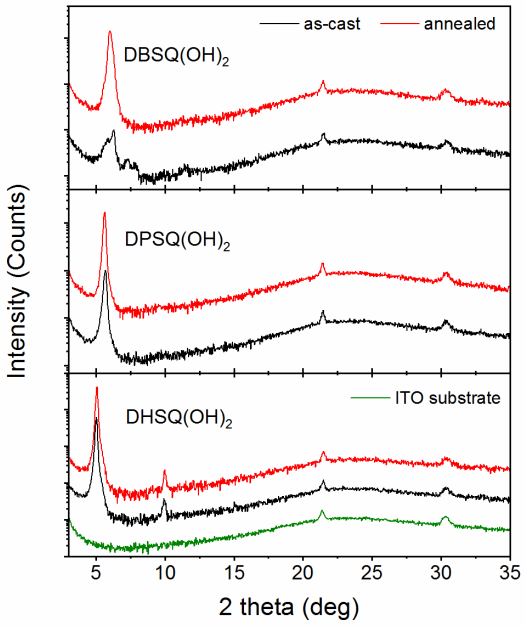

Figure 4.5 X-ray diffraction (XRD) patterns of SQ neat films before (black) and after (red) thermal annealing. The ITO substrate diffraction pattern is also provided in green. Thermal annealing was done *in-situ* with temperature ramped up every 30 ^{0}C from 30 ^{0}C to 150 ^{0}C, then cooled down to 30 ^{0}C. The results for annealed films refer to the films after they have been cooled back down to 30 ^{0}C. In order to clearly resolve all the diffraction peaks, the peak intensities were plotted logarithmically and the diffractograms of annealed films are shifted upwards.

obtained after annealing, indicated by a significant increase in the diffraction peak at $2\theta = 6.01^0$ and disappearance of the shoulder peaks. In general, SQs with longer side chains, i.e. $DHSQ(OH)_2$ and $DPSQ(OH)_2$, have a higher degree of crystallinity in the as-cast films. It is, interestingly, the opposite trend to that from the reported polymer side chain studies, which suggests that side chains could induce disorder and defects in the crystal structure.[163]

For XRD patterns of blend films (with SQ:PCBM 5:5 w/w) shown in Figure 4.5, the results correspond very well with the absorbance spectral data in Figure 4.4. First, for $DBSQ(OH)_2$:PCBM blends, the absorbance spectra indicate a complete disruption of SQ

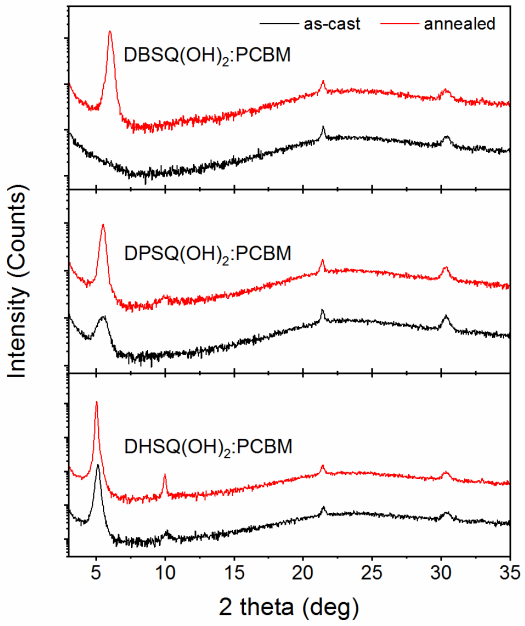

Figure 4.6 X-ray diffraction (XRD) patterns of SQ:PCBM blend films (5:5 w/w) before (black) and after (red) thermal annealing. The experimental condition was kept the same as Figure 4.5, the peak intensities were plotted logarithmically and the diffractograms of annealed films are shifted upwards.

aggregation. Correspondingly, there are no observable diffraction peaks in the XRD patterns of the DBSQ(OH)$_2$:PCBM films. Second, DHSQ(OH)$_2$ is fully aggregated in blend films as indicated by absorbance. Consistently, a sharp peak at $2\theta = 5.14^0$ is observed in the XRD patterns together with a weak peak at $2\theta = 9.99^0$. These two peaks for the blended films are consistent with the diffraction patterns of neat DHSQ(OH)$_2$ films ($2\theta = 5.01^0$ and 9.91^0), indicating that this SQ can retain highly crystalline structure in the films even in the presence of PCBM. Third, DPSQ(OH)$_2$:PCBM blend films act in an intermediate way, having a certain degree of crystallinity as predicted by absorbance spectra. Fourth, after thermal annealing, XRD patterns of all three SQ:PCBM blend films exhibit a high film crystallinity with their peaks resembling those of the annealed neat SQ

films. These trends are wholly consistent with our observations in absorbance spectra. Thus, we conclude that the film crystallinity of SQ:PCBM BHJ is completely driven by squaraine aggregation.

4.4.2 Phase separation in BHJ films

Besides the crystallinity, we have also characterized the phase separation in BHJ films using AFM and TEM. Samples for TEM measurements were prepared as described previously in Section 3.3.3. The samples prepared for AFM images were analogous to OPV devices.

For the surface morphology of SQ:PCBM blend films analyzed by tapping mode AFM, we obtained a root mean square (rms) of surface roughness to be 1.21 nm, 1.90 nm and 3.31 nm for $DBSQ(OH)_2$, $DPSQ(OH)_2$ and $DHSQ(OH)_2$ blend films respectively. Amorphous films are expected to have finer granularity and to be smoother, whereas crystalline films are expected to show a courser topography associated with the larger domains. Thus, we expect $DHSQ(OH)_2$ BHJ films to have a larger domain size due to phase separation. Indeed, we see that, in TEM images, a very clear phase separation between $DHSQ(OH)_2$ and PCBM. The diameters of the dark phases are estimated to be 60-80 nm. $DPSQ(OH)_2$:PCBM blends show a finely mixed morphology with weak bright/dark contrast and $DBSQ(OH)_2$:PCBM blends show a completely mixed and contrast-less image, which is consistent with its amorphous film morphology proven by the XRD results.

Therefore, we conclude that SQs with longer side groups have a higher degree of crystallinity and subsequently more extensive phase separation in the as-cast films. Similar observations have been reported by Nguyen *et al*[81] and Gadisa *et al*[82] for polymer-fullerene systems and by Min *et al*[83] for oligomer-fullerene systems. One explanation is that the

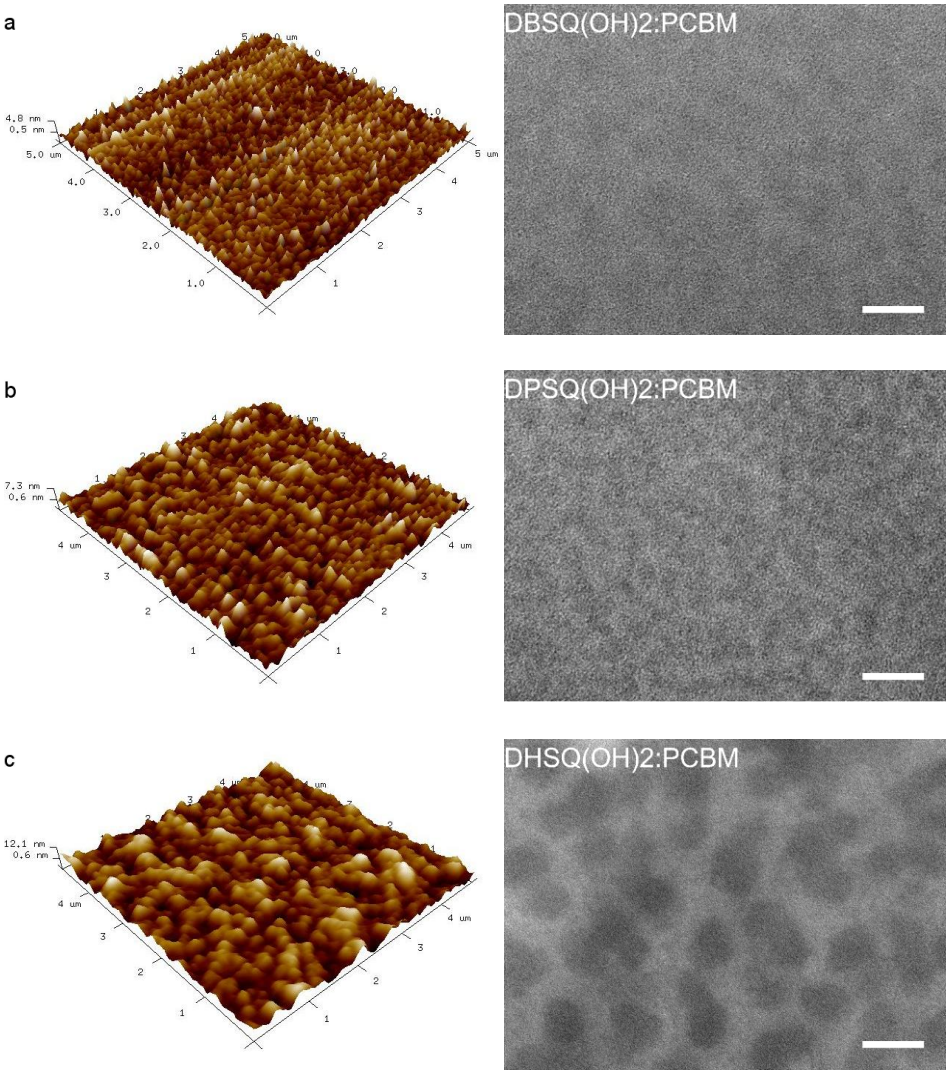

Figure 4.7 Atomic force microscope (AFM) height images (left panel) and Transmission electron microscope (TEM) images (right panel) for a) DBSQ(OH)$_2$:PCBM, b) DPSQ(OH)$_2$:PCBM and c) DHSQ(OH)$_2$:PCBM blend films. The SQ:PCBM weight ratio is 5:5. AFM image size: 5 × 5 μm. Scale bars in TEM: 100 nm.

longer side groups create more space between the rigid conjugated backbones, thus allowing improved diffusion of fullerenes towards increasing phase purity. Overall, we interpret our data in a similar way. The XRD results in Figure 4.6 show that peak position, 2θ, decreases (or d-spacing increases) as the side chain length is increased for SQ materials. If we assign the sharp XRD peak at $2\theta \approx 9\text{-}10^0$ to the (0 0 1) plane of SQ crystallites, then

the *c*-axis configuration of the crystals formed in BHJ films is calculated to be 13.52 Å, 14.31 Å and 16.22 Å for $DBSQ(OH)_2$, $DPSQ(OH)_2$ and $DHSQ(OH)_2$, respectively.

We also consider that as the side chains increase in size, the overall rigidity of the molecule is reduced, with a lower relative contribution of the intramolecular hydrogen bonding. The flexibility towards diffusion of molecules (in particular, the fullerenes) is increased. In other words, the materials will be more "liquid-like" as the side chains increase, especially at the early stage of the solution drying process during spin casting. As fullerene self-assembly takes place, this leads to the enrichment of the pure phases and therefore the phase separation is accelerated.[79] After the fullerene diffuses out from the SQ:PCBM mixed phase, the remaining SQ molecules can aggregate or crystalize into pure phases with crystallite dimensions similar to those of the neat SQ films.

4.5 Impact of Alkyl Chain on Solar Cell Performance

4.5.1 Hole carrier mobilities in neat and blend films

Due to such differences in aggregation, crystallization and phase separation for these three SQ molecules in blended films, the heterojunction blends are expected to have varying hole mobility properties and subsequently different organic photovoltaic performances.

Charge mobility is a critical factor that influences the free charge extraction (versus recombination) in the bulk heterojunction layer, and thus can significantly affect the solar cell short-circuit current and fill factor.[37,164] Previous work by Proctor *et al*[70] has shown that in solution processed small molecule (SM) solar cells with fill factor > 0.65, the hole mobilities of the donor acceptor blends are almost exclusively on the order of 10^{-4} $cm^2/V \cdot s$.

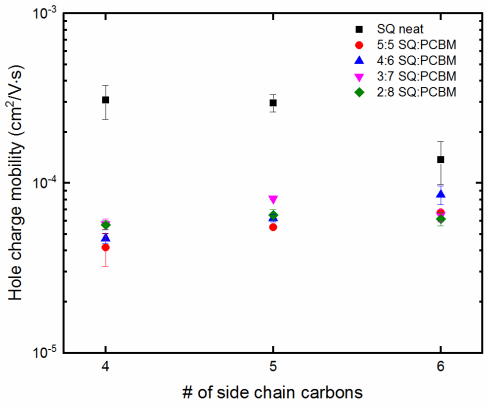

Figure 4.8 Hole mobilities of SQ neat films (black squares) and SQ:PCBM blend films (colored dots) as a function of the number of side chain carbons of the SQ molecule. The measurements were done on unannealed films. For each mobility data point, we averaged over 5 different devices.

Indeed, the hole mobility is often measured to be the lower limit of the bipolar charge transport in SM:PCBM bulk heterojunctions.[36,70,97,165] Therefore, it is considered a critical threshold property to evaluate small donor molecules for OPV application. Here, the hole mobilities of the pristine squaraine films as well as of the SQ:PCBM blend films are extracted by fitting the current-voltage curves of single carrier devices to the Mott-Gurney law for the voltage region where the current is space-charge limited.[166] The device structure and fabrication can be found in Chapter 2, and the results are shown in Figure 4.8 and Table 4.2.

The hole mobilities of SQ neat films are measured to be 3.1×10^{-4} $cm^2/V\cdot s$, 3.0×10^{-4} $cm^2/V\cdot s$, 1.4×10^{-4} $cm^2/V\cdot s$ for $DBSQ(OH)_2$, $DPSQ(OH)_2$ and $DHSQ(OH)_2$ respectively. The fitted curves can be found in Figure A2. In neat films we recall that the absorption spectra and XRD patterns are similar for each SQ, representing a similar extent of crystallinity. Therefore, we can attribute the decrease in hole mobility, as the side chain

Table 4.2 Hole mobility values of SQ neat and SQ:PCBM blend films (unit: 10^{-4} $cm^2/V{\cdot}s$).The data are averaged over 4-6 devices (the standard deviation for each parameter is shown in the parenthesis).

SQ	Neat film	SQ:PCBM blend films (D:A blend ratio)			
		(5:5)	(4:6)	(3:7)	(2:8)
$DBSQ(OH)_2$	3.1 (±0.7)	0.42 (±0.09)	0.47 (±0.03)	0.57 (±0.03)	0.56 (±0.04)
$DPSQ(OH)_2$	3.0 (±0.3)	0.55 (±0.04)	0.62 (±0.03)	0.81 (±0.01)	0.65 (±0.05)
$DHSQ(OH)_2$	1.4 (±0.4)	0.67 (±0.08)	0.85 (±0.11)	0.65 (±0.06)	0.61 (±0.06)

length increases, to the detrimental impact of non-conductive alkyl groups. Overall, the hole mobilities of SQ neat films are promising and are all above 10^{-4} $cm^2/V{\cdot}s$. Yet, after blending the SQ with PCBM, the mobility immediately drops by up to an order of magnitude, to μ_h = 4.2×10^{-5} $cm^2/V{\cdot}s$, 5.5×10^{-5} $cm^2/V{\cdot}s$, 6.7×10^{-5} $cm^2/V{\cdot}s$ for $DBSQ(OH)_2$:PCBM, $DPSQ(OH)_2$:PCBM and $DHSQ(OH)_2$:PCBM blends respectively at the 5:5 ratio. This is clearly related to the disruption of squaraine crystalline structures in blend films. If one compares the hole mobilities with the absorbance and XRD data, a trend is readily observed; for SQ with larger spectral change or crystallinity disruption when blended with fullerene (as compared to SQ neat films), the drop in hole mobility is also more significant. Specifically, $DHSQ(OH)_2$ is able to retain 50% of its neat film mobility in SQ:PCBM 5:5 (w/w) blend films, whereas the mobility of $DBSQ(OH)_2$ drops to only 10% of its neat film mobility for films with the same weight to weight blends. As a result, the hole mobilities of the blended films are similar to each other, with $DHSQ(OH)_2$ blends taking the highest value. Therefore, the change in hole mobilities between neat and blend films correlates very well with the disruption of the packing order in the SQ donor phases.

4.5.2 Organic photovoltaic performance

Organic photovoltaic devices are constructed with the same conditions for all three SQs, and the results are listed in Table 4.3. Power conversion efficiency of all three SQs are 2.0-3.6%. The Voc values slightly decrease from 0.84 V to 0.79 V as the blend ratio increases, but do not change much when comparing different SQs. This is consistent with the assumption that the alkyl side chains do not significantly perturb the electronic energy levels of these molecules. In general, higher device performance is achieved in the order of $DBSQ(OH)_2$ > $DPSQ(OH)_2$ > $DHSQ(OH)_2$.

The differences in fill factor and short circuit current in these solar cells should be highlighted. We recall that even though $DBSQ(OH)_2$ and $DPSQ(OH)_2$ each have a higher hole mobility when compared to $DHSQ(OH)_2$, the hole mobilities of SQ:PCBM BHJ films are measured to be similar for all three SQs. Therefore, we cannot use mobility alone to explain the difference in solar cell performances. In fact, the difference in solar cell performance can only be well explained by considering BHJ morphology. For 5:5 ratio, the short circuit current decreases from 8.5 mA/cm^2 to 7.6 mA/cm^2, and then to 6.8 mA/cm^2 as side chain length decreases, and the fill factors of $DBSQ(OH)_2$ and $DPSQ(OH)_2$ based devices are above 0.5 while the $DHSQ(OH)_2$ based devices only exhibited a FF of 0.44. This should be related to the dissatisfactory nanomorphology of $DHSQ(OH)_2$:PCBM at the 5:5 ratio, as shown in Figure 4.7. Specifically, the $DHSQ(OH)_2$:PCBM blend phase separates extensively while the other two blends are well mixed. Noticeably, the $DHSQ(OH)_2$:PCBM 3:7 blends yield a competitive FF of 0.5, leading to a slight increase in the efficiency to 2.9%. This is because the $DHSQ(OH)_2$ aggregation is, to a certain degree, disrupted in the 3:7 blend, as compared to the 5:5 blend. We have already shown

Table 4.3 Detailed organic photovoltaic cell parameters for SQ:PCBM at different blend ratios under 1-sun illumination. The values are obtained by averaging over 16 cells on different films (the standard deviation for each parameter is shown in the parenthesis).

SQ materials	Blend ratios	Jsc (mA/cm^2)	Voc (V)	FF (%)	PCE (%)
DBSQ(OH)2	5:5	7.59 (±0.16)	0.84 (±0.01)	47.5 (±1.4)	3.01 (±0.15)
	4:6	8.40 (±0.20)	0.82 (±0.01)	48.1 (±1.3)	3.30 (±0.12)
	1:2 (best)	8.34 (±0.11)	0.82 (±0.01)	52.0 (±0.6)	3.57 (±0.12)
	3:7	9.16 (±0.29)	0.79 (±0.01)	42.1 (±1.0)	3.02 (±0.08)
	1:3	8.01 (±0.15)	0.79 (±0.01)	40.0 (±1.2)	2.52 (±0.08)
	2:8	7.24 (±0.18)	0.74 (±0.01)	37.2 (±0.6)	1.98 (±0.08)
DPSQ(OH)2	5:5	5.98 (±0.25)	0.85 (±0.01)	51.6 (±1.7)	2.62 (±0.19)
	4:6	6.74 (±0.17)	0.84 (±0.01)	53.0 (±2.0)	2.99 (±0.15)
	1:2	7.28 (±0.24)	0.83 (±0.01)	50.0 (±1.8)	3.00 (±0.08)
	3:7 (best)	7.36 (±0.17)	0.83 (±0.01)	52.3 (±1.6)	3.20 (±0.10)
	1:3	7.83 (±0.12)	0.82 (±0.01)	45.5 (±1.7)	2.92 (±0.11)
	2:8	7.57 (±0.16)	0.80 (±0.01)	43.2 (±1.9)	2.63 (±0.13)
DHSQ(OH)2	5:5	6.47 (±0.17)	0.84 (±0.01)	43.1 (±1.4)	2.34 (±0.14)
	4:6	6.69 (±0.19)	0.83 (±0.01)	46.4 (±1.0)	2.59 (±0.13)
	3:7 (best)	6.76 (±0.19)	0.82 (±0.01)	48.5 (±2.0)	2.68 (±0.16)
	2:8	6.52 (±0.29)	0.79 (±0.01)	42.9 (±2.0)	2.22 (±0.21)

in Chapter 3, that the SQ phase domain size is greatly reduced as the PCBM weight ratio increases. As a result, the $DHSQ(OH)_2$:PCBM 3:7 w/w BHJ morphology has been slightly improved towards a more well mixed state, similar to $DBSQ(OH)_2$:PCBM and $DPSQ(OH)_2$:PCBM blends at the 5:5 weight ratio. Therefore, SQs with longer side chains need more PCBM to disrupt the aggregation and thus to suppress the phase separation.

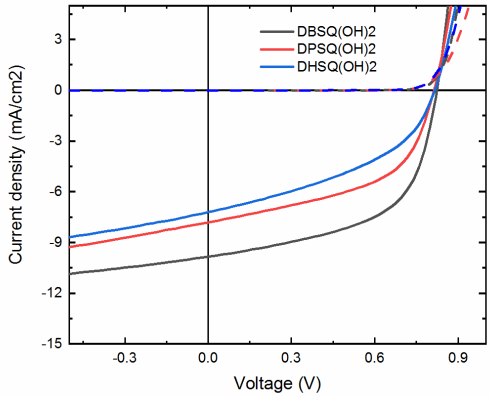

Figure 4.9 J-V curves of the representative SQ:$PC_{71}BM$ bulk heterojunction solar cell for each squaraine molecule. The dark current is shown in the dashed line suggesting the robustness of the solar cell devices.

We then switched the fullerene acceptor from PCBM to $PC_{71}BM$. $PC_{71}BM$ has a higher absorptivity in the visible region of the spectrum, and thus is expected to enhance the contribution of fullerene absorption to photo-generated charges. The efficiency is further increased by using $PC_{71}BM$ for $DBSQ(OH)_2$, mainly due to the improved short-circuit current from 8.5 mA/cm^2 to 10.2 mA/cm^2, resulting in an increased power conversion efficiency to 5.4% (champion device). Interestingly, the solar cell characteristics remain the same for $DPSQ(OH)_2$ based devices independent of fullerene choice. For $DHSQ(OH)_2$, the solar cell efficiency even decreases from 2.9% to 2.5%, after switching the acceptor from PCBM to $PC_{71}BM$. This could be related to the enhanced phase separation when using $PC_{71}BM$ as the acceptor.[60]

Although the $DBSQ(OH)_2$:$PC_{71}BM$ blend has achieved the best solar cell efficiency, the XRD data suggest that the blend is essentially amorphous, resulting from highly mixed SQ and fullerene. This amorphous state leads to a large drop in hole mobility in the blend films (4.2×10^{-5} cm^2/V·s) as compared to the neat films (3.1×10^{-4} cm^2/V·s), which is a

significant drawback for charge transport and collection. We noticed that there are a few small molecules, such as the dithienosilole (DTS) based donors, which are able to retain high hole mobilities when blended with PCBM.[15,70,77] As a result, the OPV devices produced by such materials are more efficient compared to our SQ-based OPV cells. We thus highlight a possible future study to improve the hole mobility of SQ materials when blended with fullerenes.

Table 4.4 OPV parameters of optimized DA ratio of $DBSQ(OH)_2$, $DPSQ(OH)_2$ and $DHSQ(OH)_2$ when blended with $PC_{71}BM$. Devices are made the same way as the devices using PCBM. The data are analyzed by averaging over 16 devices on different films.

Donor	Blend ratios	Jsc, mA/cm^2	Voc, V	FF	PCE, % (ave.)[a]
DBSQ(OH)2	1:2	9.98 (±0.30)	0.82 (±0.01)	0.55 (±0.01)	4.54 (±0.20)
DPSQ(OH)2	3:7	7.65 (±0.10)	0.82 (±0.02)	0.49 (±0.01)	3.10 (±0.11)
DHSQ(OH)2	3:7	6.72 (±0.51)	0.80 (±0.02)	0.41 (±0.01)	2.24 (±0.21)

4.5.3 Optimizing $DBSQ(OH)_2$-based devices

In Chapter 3, we demonstrated that the film morphology can be carefully optimized by thermal annealing at a low temperature. Here, we conducted thermal and solvent vapor treatment for DBSQ(OH)2:$PC_{71}BM$ BHJ solar cells and seek to further improve the solar cell efficiency.

Nevertheless, we found that the solar cell efficiency is reduced when the devices were annealed at 90 ^{0}C or through gentle solvent annealing for 5 min (Table 4.5). The drop in

Table 4.5 Photovoltaic performances of $DBSQ(OH)_2$:PCBM and $DBSQ(OH)_2$:$PC_{71}BM$ BHJ solar cells before and after annealing treatment. The optimized ratio of 1:2 is used in this study. The treatment is done before the evaporation of the aluminum anode.

Acceptor	Treatment	Jsc, mA/cm^2	Voc, V	FF	PCE, %
PCBM	No	8.31 (±0.11)	0.83 (±0.01)	0.52 (±0.01)	3.57 (±0.12)
	TA[a]	7.76 (±0.19)	0.75 (±0.02)	0.47 (±0.01)	2.71 (±0.14)
	SVA[b]	8.07 (±0.21)	0.78 (±0.02)	0.45 (±0.01)	2.84 (±0.14)
$PC_{71}BM$	No	9.98 (±0.30)	0.82 (±0.01)	0.55 (±0.01)	4.54 (±0.20)
	TA[a]	9.91 (±0.32)	0.80 (±0.01)	0.44 (±0.02)	3.48 (±0.12)
	SVA[b]	9.83 (±0.24)	0.80 (±0.02)	0.44 (±0.01)	3.41 (±0.11)

[a] TA is thermal annealing at 90 ^{0}C for 5 min after spin casting the active layer.
[b] SVA is solvent vapor annealing by subjecting the films in chloroform vapor for 5 min.

device efficiency mainly comes from the slightly reduced Voc and largely reduced FF. This is contradictory to what we have found previously in Chapter 3. For treated films, the crystallinity is only marginally improved as proven by the XRD patterns in Figure 4.10, and the BHJ films are still largely amorphous. On the other hand, the no extensive phase separation was seen in the TEM images (Figure 4.11). Here, we think the $DBSQ(OH)_2$:PCBM (or $PC_{71}BM$) system might be different from that of $DHSQ(OH)_2$, in that the $DHSQ(OH)_2$ will have already formed significant amount of aggregates in the blend films (during spin casting), while $DBSQ(OH)_2$ largely remains as monomers. Therefore, an annealing treatment of $DBSQ(OH)_2$-based devices would induce much larger change in the relative populations of monomers and aggregates. We look to understand the relative contributions of the energetic states (i.e. excited states of monomer and aggregate)

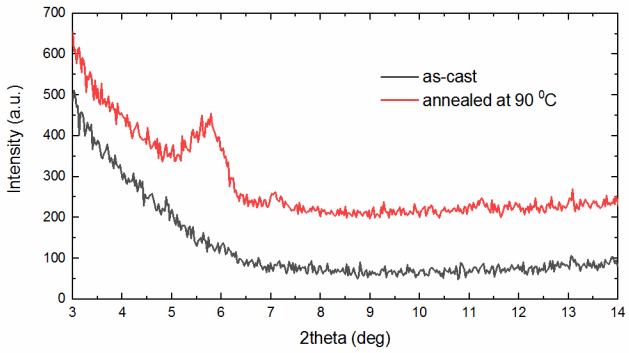

Figure 4.10 X-ray diffraction patterns of DBSQ(OH)$_2$:PCBM (1:2 w/w) films before (black) and after (red) thermal annealing at 90 ^{0}C for 5 min. In order to clearly resolve all the diffraction peaks, the diffractograms of the annealed film are shifted upward.

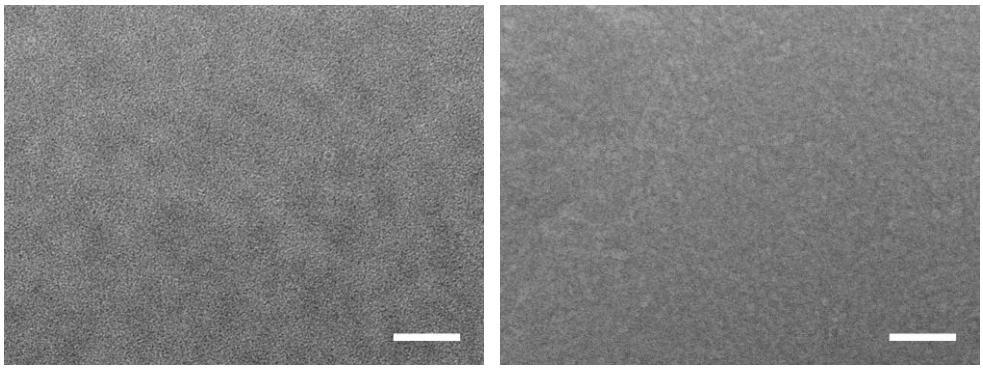

Figure 4.11 TEM images of DBSQ(OH)$_2$:PCBM (1:2 w/w) bulk heterojunction films before (left) and after (right) thermal annealing at 90 ^{0}C for 5 min. Scale bar: 100 nm.

to the dissociated charges at the heterojunction interface in the following chapters of this dissertation.

4.6 Discussion

In this chapter, we have provided a comprehensive description of the properties of a series of squaraines with varying side-chain length, pertinent to their use in organic

photovoltaics. Despite the molecular structure differences, the molecules pack with the same slip-stack motif, and absorbance spectra of neat films are very similar for each material. Nevertheless, when these squaraines are blended with PCBM, the differences in properties that drive OPV efficiency become apparent. Absorbance spectra indicate well a qualitative disruption of crystallinity, more so for short chain squaraines. For longer side-chain squaraines, phase separation is more significant and some evidence of crystal structure is retained by $DHSQ(OH)_2$:PCBM blends. Melting point and crystallization temperatures decrease as the side chains become larger, which leads to a greater ease of squaraine and PCBM self-assembly.

Hole carrier mobility is increased for neat films made with squaraines of short side chain length but when crystal packing is disrupted in blends, this mobility drops. For squaraines of longer side chain length, the blended films retain a higher mobility than their short chain counterparts, resulting from phase separation during the spin casting process phase separation even during the spin casting process. However, ultimately it is the phase separation that limits the power conversion efficiency. We found that the amorphous film with the finely mixed morphology yielded better device performance than the crystalline film with phase separated donor and acceptor domains. These results and interpretations culminate in an ongoing strategy to maximize ordered molecular packing while maintaining smaller domain sizes that nevertheless connect in a bicontinuous network. $DBSQ(OH)_2$ is therefore the best selection in our series (while solubility for squaraines decreases quickly as chain length is reduced further).

This observation of reduced efficiency with increased phase separation seems different to results from a previously reported squaraine, $DiBSQ(OH)_2$, (or DIBSQ). In this case,

Wei *et al* have reported an increase in power conversion efficiency when the BHJ film was subjected to thermal or solvent annealing (leading to higher squaraine aggregation and film crystallinity).[41,121] We, on the other hand, found an immediate decrease in efficiency when we mildly anneal our devices. This might be attributed to the different alkyl groups between DiBSQ(OH)$_2$ (i.e. branched alkyl chains) and the series of squaraines investigated in this chapter (i.e. linear alkyl chains). Specifically, the linear alkyl chains in our squaraines will lead to tighter and more thermodynamically favorable aggregation/crystallization, based on chemical intuition. When we compared the annealed BHJ films, we found that our DIBSQ:PC$_{71}$BM BHJ showed a much higher diffraction peak in XRD and a more dramatic absorption change due to squaraine aggregation than DIBSQ:PC$_{71}$BM with similar annealing procedures.[41,167] The linear alkyl chains are expected to allow a better diffusion of fullerenes in the BHJ films. Even though TEM shows no phase contrast, we estimate that a small extent of phase separation has already taken place in as-cast DBSQ(OH)2:PC$_{71}$BM films, leading to an optimal BHJ morphology even without annealing. Thus, as-cast DBSQ(OH)$_2$-based devices can yield comparable efficiency as the DIBSQ-based devices with post additional treatments.[41,121]

Chapter 5. USING AN ESSENTIAL-STATE MODEL TO INVESTIGATE THE COULOMBIC INTERACTIONS IN SQUARAINE AGGREGATES

In this chapter, we use an Essential-state model (ESM) to simulate the SQ monomer and aggregate absorption spectra. The basics of ESM have been introduced in Chapter 1. Three diabatic electronic states are employed to describe the charge resonant structures of the quadrupolar SQ molecules and the Hamiltonian is diagonalized to yield vertical ground and excited states. By adding vibrational and vibronic Hamiltonians, the SQ monomeric absorption spectra can be well reproduced by ESM. For SQ aggregates, there are two forms in as-cast and annealed blend films; one has a slightly broader absorption spectrum than for monomers and a higher Franck-Condon shoulder; the other has a much broader absorption spectrum with a "double-hump" profile. By performing joint experimental and theoretical investigations, we have successfully simulated the absorption spectrum of the first type of aggregates that were observed in as-cast BHJ films and analogous PMMA solid solution films. We conclude that this is a typical H-aggregate where the Coulombic coupling dominates the intermolecular interactions when molecules are less densely packed. The spectrum of the second type of aggregates cannot be rationalized with the current model indicating another form of interactions exists between molecules in the aggregates (for details see Chapter 6).

5.1 Introduction

Understanding the nature of the excited states of squaraine donors is critical for developing efficient OPV cells as well as many other optoelectronic applications. Schwenn *et al*,[168] and separately Coffey *et al*[169] discuss the major driving forces for generation of free carriers from excitonic states using Marcus Hush theory (see Section 1.3.3). The molecular aggregates are known to have shifted electronic states due to the intermolecular interactions.[105] Thus, the driving force for electron transfer from the squaraine aggregates to fullerene acceptor should be different when compared to the electron transfer from squaraine monomers. Spencer *et al*.[170] subsequently describe how Marcus-Hush theory can be used to explain why the increased crystallinity (and associated aggregation) within squaraine devices may have a detrimental effect upon the donor-acceptor electron transfer rate, which appears to limit OPV device efficiency.

In a system with a variety of aggregates and polymorphs, the intermolecular coupling between the multiple donors and the fullerene acceptor will vary depending on the electronic and spatial properties of those donor species. Thus, even for the simple binary bulk heterojunction systems, the ability of molecules to form aggregates, polymorphs, or complexes could introduce more than one type of donor-acceptor interface. For our studied SQ molecules, e.g. $DBSQ(OH)_2$, the absorption of the solution shows a narrow peak (FWHM ~ 0.081 eV) at 650 nm, which transfers to a broader profile in as-cast BHJ films, and then further changes into a characteristic "double-hump" spectrum after thermal annealing. Thus, there exist at least two types of SQ:PCBM interfaces and annealing would change the relative population these two. Direct comparison of these two interfaces in terms of their contribution to OPV performance might be complicated given that there are

many other critical factors, such as BHJ morphology, charge mobility, anode or cathode buffer layers, etc. Therefore, we must first develop a comprehensive understanding of the excited state properties of squaraines, based on their molecular structure and the solid state packing in pure and blended form.

In more recent work, some confusion seems apparent regarding the origin of the panchromatic solid state spectral features when using typical assignments[134,171–175] based solely on the aggregation-induced spectral shifts[176,177] described by Kasha.[105], where a red-shift is characteristic of J-aggregates and a blue-shift is characteristic of H-aggregates. Thus, high energy peaks are often attributed to H-state excitation, and low energy peaks attributed to J-state excitation. Such an assignment is misleading considering that spectral shifts can arise from non-resonant couplings.[177,150] In addition, concerted H- and J-state excitations (i.e. Davydov splitting) rely on the oblique arrangement of transition dipole moments, contradicted by the observation that the SQ single crystal structures feature a slip stacking motif with one molecule per unit cell (Figure 4.2). Thus, accurate interpretation of the SQ film absorbance spectra is the critical first step to understand the energetic states of SQ aggregates.

Bigelow and Freund[178] performed semi-empirical molecular orbital calculations on squaraine monomers, emphasizing the ground state conformational and solution-phase spectroscopic properties. In solution, they describe a positively charged solvent cage surrounding the oxygen atoms and a negatively charged solvent cage surrounding the amino phenyls, inducing a greater $D^{+/2}$-A^{-}-$D^{+/2}$ character within the ground state. The calculations of Bigelow and Freund[178] suggest that the crystal structure of a hydroxy-squaraine might reveal an intermolecular packing consistent with these solvent

interactions, i.e. the zwitterionic contribution in the crystal phase seems to be stabilized through intermolecular electrostatic interactions in a manner similar to the stabilization achieved in solution via the formation of squaraine/solvent complexes.

Mixing of zwitterionic character within the ground state was also shown by Painelli and coworkers to be essential for describing symmetry-breaking and solvatochromism in a variety of quadrupolar dye molecules.[107] The essential-state model accounts for the charge-transfer nature of the transitions within a given squaraine: each chromophore is described with two donor units (amine side arms) and a central squarylium acceptor unit.

In this chapter, we investigate the SQ monomer and aggregates by using the ESM. For SQ aggregates in as-cast BHJ films as well as in PMMA solid solution films, we consider the Coulombic interaction between different donor and acceptor sites of the molecule. With a full understanding of the nature of the excited states in squaraine aggregates, we provide a foundation to recognize the critical impact of controlling aggregation towards higher efficiencies of OPV devices, which rely on a fast rate of charge transfer at the bulk heterojunction interface.

5.2 Models

5.2.1 Monomer Hamiltonian with vibronic coupling

In this section, we derive the Hamiltonian for a symmetric SQ chromophore and its aggregate using the ESM.[107,108] As previously introduced in Section 1.5.3, for quadrupolar dyes with linear D-π-A-π-D or A-π-D-π-A structures, the ESM identifies three essential states including one neutral state and two degenerate zwitterionic states, i.e. D-A-D ($|N\rangle$), D^+-A^--D ($|Z_1\rangle$) and D-A^--D^+ ($|Z_2\rangle$) (with similar definitions for the A-π-D-π-A molecule).

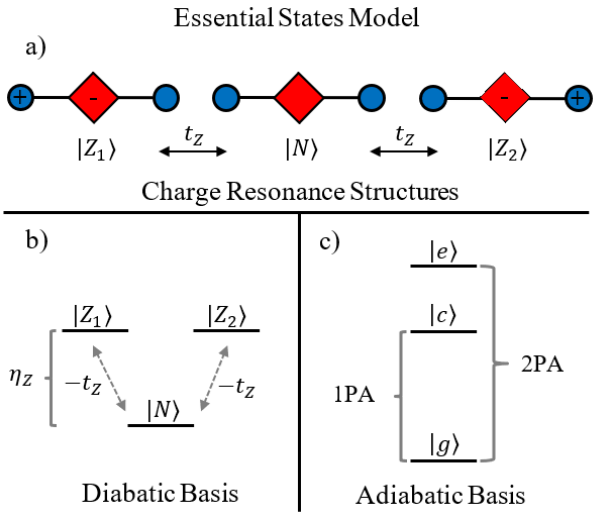

Figure 5.1 Illustration of the basic concepts of the Essential-state model (ESM) for squaraine molecules. a) Three essential diabatic states describing the charge resonance structures; b) energy diagram of diabatic states and coupling between them; c) energy diagram of adiabatic states calculated based on the Hamiltonian in Equation (5.1).

The two zwitterionic states lie above the neutral state with energy η_z ($\eta_z > 0$) and are coupled to the neutral state via a charge transfer integral, t_z. The electronic Hamiltonian for a single chromophore can thus be expressed as

$$\hat{H}_{mon}^{el} = \eta_z \sum_a |Z_a\rangle\langle Z_a| - t_z \sum_a \{|N\rangle\langle Z_a| + h.c.\} \tag{5.1}$$

Diagonalizing the Hamiltonian yields three "adiabatic" states, each a linear combination of the essential "diabatic" states:

$$|g\rangle = \sqrt{1-\rho}\,|N\rangle + \sqrt{\rho/2}\,(|Z_1\rangle + |Z_2\rangle) \tag{5.2}$$

$$|c\rangle = \sqrt{1/2}\,(|Z_1\rangle - |Z_2\rangle) \tag{5.3}$$

$$|e\rangle = \sqrt{\rho}|N\rangle - \sqrt{(1-\rho)/2}\,(|Z_1\rangle + |Z_2\rangle) \tag{5.4}$$

where $|g\rangle$ is the ground state, and $|c\rangle$ and $|e\rangle$ are the first (one-photon allowed) and second

(two-photon allowed) excited states. The energy of each electronic state is: $E_g = \eta_Z - t_Z\sqrt{2(1-\rho)/\rho}$, $E_c = \eta_Z$ and $E_e = \eta_Z + t_Z\sqrt{2\rho/(1-\rho)}$. Here, $\rho = 0.5(1 - \eta_Z/\sqrt{\eta_Z^2 + 2t_Z^2})$ which defines the charge distribution of the squaraine molecule in the ground state, $D^{\rho}/_2 - A^{-\rho} - D^{\rho}/_2$. When ρ is approaching 0 (η_Z is a large positive value), the ground state is dominated by the $|N\rangle$ state and the $|c\rangle$ and $|e\rangle$ states become degenerate and are dominated by zwitterionic states. The $|c\rangle$ state is completely zwitterionic, independent of ρ. Thus, $|c\rangle$ can be represented by $D^{0.5} - A^{-1} - D^{0.5}$, with the charge having been completely moved from nitrogen to squarylium. For a typical quadrupolar dye, $0 < \rho < 0.5$.

In order to account for intramolecular vibrations, one vibrational coordinate is introduced for each charge transfer degree of freedom (vibrational site), thereby accounting for the nuclear geometry rearrangement caused by the different charge distributions. For each vibrational site, we visualize each arm as a quantum harmonic oscillator adopting a vibrational mode with an energy quantum of $\hbar\omega_{vib}$ = 1300 cm^{-1} (or 0.16 eV). Thus, the vibrational Hamiltonian reads,

$$\hat{H}_{vib}^{mon} = \hbar\omega_{vib}\sum_a b_a^\dagger b_a \tag{5.5}$$

where $b_a^\dagger$ (b_a) creates (annihilates) a vibrational quantum on each molecular arm ($a = 1$, left arm; $a = 2$, right arm) of the chromophore with an energy of $\hbar\omega_{vib}$ (assumed to be the same for both neutral and zwitterionic states). For monomer simulations, we found that the total vibrational quanta (left + right arms) of 4 is able to accurately reproduce the experimental absorbance spectra.

For vibronic coupling, the nuclear geometry of each arm is represented as a harmonic

potential with the equilibrium point (arm length) defined by the electronic state of the system. If one arm is hosting a zwitterion, the parabola minimum of its nuclear potential surface will be shifted, as compared to its neutral form, by λ_z^2, which is the (zwitterionic) Huang-Rhys (HR) parameter, and $\lambda_z^2 = 1$. Thereafter, orthogonality requirements are dropped and the vibronic coupling is allowed between $|N\rangle$ and $|Z_1\rangle$ or $|N\rangle$ and $|Z_2\rangle$ with a different vibrational state on the appropriate arm. The vibronic coupling factors are calculated through the Franck-Condon principle. For example, the neutral state with one vibrational quantum on its left arm ($|N\_1\_0\rangle$) can couple to the first zwitterionic state with no vibrational quantum ($|Z_1\_0\_0\rangle$) through an integral of $-t_z\langle 1|\tilde{0}\rangle$. The first and second terms are the electronic and the vibronic coupling terms, respectively. Note that the vibrations on the right arm for the two states are the same (= 0 in this case). If, on the other hand, the vibrational quantum numbers on the right arms of the $|N\rangle$ and $|Z_1\rangle$ state are different, the coupling term as well as the whole integral goes to zero, which is subject to the orthonormality rule of the wavefunction. Therefore, we can write the vibronic coupling term in the Hamiltonian as:

$$\widehat{H}_{vib}^{mon} = \hbar\omega_{vib}\lambda_z \sum_a \left(b_a^\dagger + b_a + \lambda_z\right)|N\rangle\langle Z_a| \tag{5.6}$$

The complete monomer Hamiltonian constructed by combining the electronic (Equation (5.1)), vibrational (Equation (5.5)) and vibronic (Equation (5.6)) Hamiltonians is:

$$\widehat{H}^{mon} = H_{el}^{mon} + H_{vib}^{mon} + H_{vib-el}^{mon} \tag{5.7}$$

The eigenvalues and eigenstates can be obtained by diagonalization of the Hamiltonian in Equation (5.7).

5.2.2 Aggregate Hamiltonian with Coulombic coupling

For squaraine aggregate, we first consider the Coulomb interaction between molecules in zwitterionic states; the zwitterion charge densities are collapsed to positive and negative point charges residing on the nitrogen atoms and at the center of the four-membered ring, respectively. Thus, the Coulomb potential for each specific aggregate state $|S\rangle$ can be calculated by:

$$\hat{V} = \frac{1}{4\pi\varepsilon\varepsilon_0}\sum_{S}\sum_{n>m}\sum_{i,j}\frac{\boldsymbol{q}_n(i)\boldsymbol{q}_m(j)}{|\boldsymbol{r}_{n,i}-\boldsymbol{r}_{m,j}|}|S\rangle\langle S| \tag{5.8}$$

where ε is the dielectric constant of the materials and is assumed to be equal to 3 in the calculation, taking into account the screening of charges not explicitly accounted for within the model. n and m counts the molecule number in the aggregates, while i and j counts the site number on each molecule (= 1, 2 and 3 for left nitrogen, central squarylium and right nitrogen). $\boldsymbol{q}$ and $\boldsymbol{r}$ represent the point charge and the position vector for a specific molecular site, and we input values taken from the experimental squaraine single crystal structure determination. We assume that the squaraine aggregates in thin films adopt similar packing structures as in the single crystal. The single crystal structures for all unbranched alkyl anilinic di-hydroxyl squaraines studied in our work share a similar slip-stack motif.

The $DBSQ(OH)_2$ single crystal structure is shown in Figure 4.2 in Chapter 4. The Coulomb interaction between molecules in different stacks in single crystal structure can be neglected because the distance between the functional groups is far (> 10 Å, see crystal dimensions in Table 4.1). Thus we only consider the Coulomb interaction between the nearest-neighbor molecules in the same stack. The distance between two interacting point charges can be calculated using four geometry parameters: the arm length (l), the pi-

stacking distance (Δz), and the long (Δx) and short (Δy) axis displacements. The arm length, l, is the distance separating the nitrogen atoms from the center of the squarylium ring. The pi-stacking distance, Δz, is the distance between the two planes of neighboring molecules. Δx is the slip distance along the long molecular axis (across two nitrogen atoms). Finally, Δy is the slip distance along the short molecular axis (across two oxygen atoms).

With Equation (5.8), we can write the Coulombically-coupled (CC) aggregate as

$$\hat{H}_{CC}^{Agg} = \sum_{n} \hat{H}_{n}^{mon} + \hat{V} \tag{5.9}$$

Here, the aggregate contains n chromophores in one stack of molecules. While the Coulomb interaction impacts only the diagonal elements of the Hamiltonian when expressed in the diabatic basis, rotation into the adiabatic basis that diagonalizes $\sum_n \hat{H}_n^{mon}$ transforms these interactions to the more familiar terms responsible for resonant energy transfer between molecular sites. The off-diagonal terms coupling degenerate states are similar to the terms that serve to couple molecular excitons in exciton theory. For example, when the intermolecular separation *R* is large, the familiar point-dipole coupling expression which scales as R^3 is recovered. Additionally, there are off-resonant Coulomb terms which account for the molecular polarizability by allowing states having different numbers of excitations to mix.

5.2.3 Oscillator strength and optical spectra calculation

Oscillator strength describes the probability of the transition between eigenstates (*e.g.* absorption or emission) and is proportional to the square of the transition dipole moment, a quantum mechanical matrix, as:

$$f_{ge} = E_{ge}\langle G|\hat{\mu}|\Psi_e\rangle^2 \tag{5.10}$$

$\hat{\mu}$ is the dipole moment operator; G and Ψ_e are the wavefunctions of the ground (with the lowest-energy state) and excited states of the transition, whose values can be pulled directly from the eigenvector matrix. The transition energy is given by $E_{ge} = E_e - E_g$. The oscillator strength calculations run over all the eigenstates that are above the ground state (defined by its energy).

The dipole moment of a given state in the diabatic basis is calculated by collapsing the charge densities to point charges located on the donor or acceptor moiety as described above. For a pair of equal and opposite charges (e) separated by a distance r, $\mu = e\vec{r}$.[179] In the case of squaraine monomer, r should be equal to the arm length. To simplify the calculations, we normalize the dipole moment (by setting the arm length equal to 1) to get the relative oscillator strength values. Thus, the monomer dipole moment operator can be simply written as

$$\hat{\mu} = |Z_2\rangle\langle Z_2| - |Z_1\rangle\langle Z_1| \tag{5.11}$$

given that the dipole moments of the two zwitterionic states are of the same magnitude with opposite direction. For aggregates, the dipole moment can be evaluated by the sum over the charge expression:

$$\boldsymbol{\mu}(S) = \sum_n \sum_{q_S(n)} q_S(n)\boldsymbol{r}_{q_S(n)} \tag{5.12}$$

where the terms are defined previously.

The absorbance spectra are calculated by applying a Gaussian broadening function to the oscillator strength of the ground-to-excited state transitions:

$$A(E) = \sum_{\Psi_e} f_{ge} \exp(-\frac{E - E_{ge}{}^2}{\sigma^2}) \tag{5.13}$$

where $2\sqrt{\ln(2)}\,\sigma$ is the full width at half maximum of the absorbance line shape.

The fluorescence spectra are calculated in a similar manner as the absorbance (Equation (5.13)):

$$F(E) = \sum_{\Psi_g} E_{e_0 g} \left|\langle \Psi_{e_0} | \hat{\mu} | \Psi_g \rangle\right|^2 \exp(-\frac{E^2}{\sigma^2}) \tag{5.14}$$

where the calculation runs over all the eigenstates that are below the initial excited state. Thus, the identification of the initial excited states $|\Psi_{e_0}\rangle$ is critical. We assume that, after excitation, the excited state with the lowest energy is populated as the relaxation generally happens much quicker than emission. Thus $|\Psi_{e_0}\rangle$ is the excited state with the lowest energy. We note that each eigenstate is a linear combination of the essential diabatic states. For the SQ aggregate, the electronic ground state and excited states have different combinations from the neutral and zwitterionic states, analogous to that of the monomer as shown in Equation (5.2) – Equation (5.4). Generally, the ground (excited) state has less (more) contribution from the zwitterionic state. Hence, $|\Psi_{e_0}\rangle$ is the lowest-energy state that has a sudden increase in the zwitterionic character.

5.3 Experiments and Simulations

5.3.1 Monomer absorption spectrum and simulations

In order to parameterize the essential states Hamiltonian of Equation (5.13) for SQ spectra, we compared our calculated absorption spectrum for each molecule with the experimentally measured spectrum.

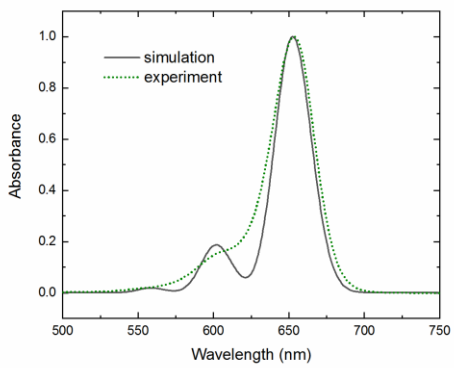

Figure 5.2 Simulated (black line) and experimental (green dots) monomer absorption spectra (normalized to the maximum). Simulation parameters are listed in Table 5.1.

Previously, Painelli and coworkers have successfully applied ESM to SQ molecules.[107,108] In accordance with their results for a similar SQ, we set t_Z = 1.05 eV. The vibrational quantum, $\hbar\omega_{vib}$ = 1300 cm^{-1} (0.16 eV), corresponding to the vinyl stretching mode in nuclear motions of conjugated molecule.[106] The zwitterionic Huang-Rhys parameter (λ_z^2) describes the displacement of the potential energy surface minima between the zwitterionic and neutral states, and its value is set equal to 1. [106,180] By adjusting the energy of the diabatic zwitterion states until our simulations reproduced the experimental spectrum, we obtained $\eta_Z = 0.69$ eV for the best spectral fit. For all monomer calculations, we have applied a Gaussian lineshape function with standard deviation 0.06 eV.

Figure 5.2 shows the simulated monomer spectrum along with the experimental results for comparison. A good fit is demonstrated by using the parameters in Table 5.1. These parameters are the same for all the other di-hydroxyl squaraine molecules studied (such as DPrSQ(OH)$_2$, DPSQ(OH)$_2$ and DHSQ(OH)$_2$), which is expected as they share the same conjugation backbones. It is quite interesting that a (diabatic) HR factor of unity for the vibronic coupling within each "arm" does not lead to a vibronic progression with roughly

equal 0-0 and 0-1 intensities, as would be expected of the Poissonian progression with a HR factor of 1. This is because the ESM approach is different to the well-known exciton model in that the essential states selected to represent the chromophore are "premixed" or diabatic states. Thus, the parameters associated with these diabatic states cannot be directly "copied" into the adiabatic regime. For example, after diagonalizing the monomer Hamiltonian, λ_z, which denotes the PES shift in the diabatic basis, is transformed into λ, which describes the PES shift in the adiabatic eigenstates (i.e. ground and excited states). Thus, one cannot simply extract λ_z from the vibronic progression present in the monomer absorption or emission spectra.

Table 5.1 Simulation parameters for the SQ monomer absorption spectrum that best represents the experimental data in chloroform solution.

Parameter	$DBSQ(OH)_2$
η_Z	0.69 eV
t_Z	1.05 eV
λ_z^2	1
$\hbar\omega_{vib}$	0.16 eV
Vibmax	4
Linewidth	0.15 eV
Spectral Shift	-0.087 eV

5.3.2 Aggregate absorption spectrum in PMMA films

The absorption spectra of SQ thin films are different from that in solution (e.g. $DBSQ(OH)_2$ in different environments in Figure 5.3). In particular, as shown in Figure 5.3, the absorption of the solution shows a narrow peak at 650 nm with a Franck-Condon (FC)

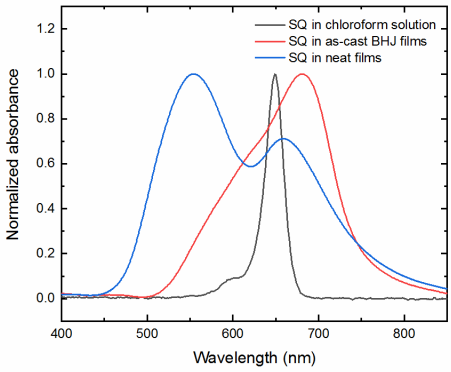

Figure 5.3 Normalized absorption spectra of $DBSQ(OH)_2$ in chloroform solution (black), as-cast BHJ films (red) and neat films (blue). The concentration of solution is 10^{-5} M. The spectrum of as-cast BHJ films (SQ:PCBM 1:1 w/w) is obtained by subtracting the PCBM contribution from the total absorption.

shoulder at 600 nm. SQ molecules in as-cast BHJ films exhibit slightly broader profiles with a red-shifted peak at 678 nm. Also, the FC shoulder is taking a higher oscillator strength than that of the solution spectra. The SQ molecules in neat films provide a unique "double-hump" absorption profile and both peaks are broad, leading to a panchromatic absorption spectra. These spectral differences for the SQs result from the different intermolecular interactions in various environments. For solutions with a concentration of 10^{-5} M, the SQ molecules are completely dissolved with an average intermolecular distance of ~ 55 nm. At such large distances, the intermolecular interaction is negligible. Thus, the solution spectrum clearly belongs to the SQ monomer. For thin films, the intermolecular separation is much closer. In such cases, the intermolecular interactions, such as Coulombic coupling (CC) or intermolecular charge transfer (ICT), become strong and significantly impact the absorption spectra.

In this chapter, we continue to focus on the SQ aggregates in BHJ films in Figure 5.3.

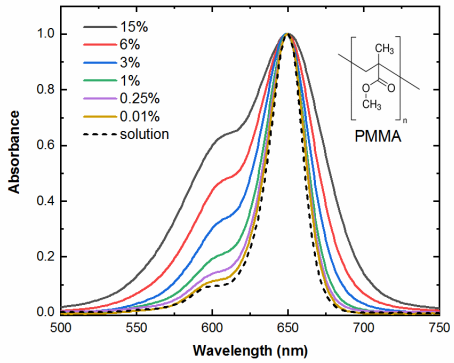

Figure 5.4 Normalized absorption spectra of $DBSQ(OH)_2$ in PMMA films with varying SQ wt%. The SQ solution spectrum is also shown in dashed line for comparison. Inset: molecular structure of PMMA.

In SQ:PCBM BHJ films, nevertheless, the interactions are complicated. As previously mentioned, the red-shifted absorption peak may come from the SQ-PCBM interaction. Thus, we blend polymethylmethacrylate (PMMA) polymer, instead of PCBM, with SQ to control its aggregate. PMMA is a transparent, inert polymer with good solubility in typical organic solvents. It does not interact with SQs and shows little absorption in the SQ-active region. Upon spin casting, we effectively disperse SQs randomly in the PMMA matrix and the intermolecular separation is controlled by the weight percent of the SQs. With controlled intermolecular distance, we can obtained the SQ aggregates that mimic the aggregates in as-cast BHJ films.

As shown in Figure 5.4, when $DBSQ(OH)_2$ is mixed into the PMMA matrices, the absorption profile is shown to antisymmetrically broaden such that the 0-1 vibronic transition gains oscillator strength as the wt% of SQ increases from 0.01% to 15%. The absorption spectrum of the 0.01 wt% PMMA film is almost overlapping with the solution spectrum, suggesting minimum intermolecular interactions. With the PMMA density of

1.17 g cm^{-3} (Sigma-Aldrich), we estimated a SQ intermolecular distance of ~20 nm in the 0.01 wt% PMMA film (Equation (2.1)). This separation distance quickly decreased to ~1.7 nm in the 15 wt% PMMA film (data listed in Table 5.2).

Table 5.2 Estimated intermolecular distance of SQ molecules in PMMA films.

wt%	Distance (nm)
0.01%	19.9
0.25%	6.8
1%	4.3
3%	3.0
6%	2.4
15%	1.7

5.3.3 Simulation of CC-aggregate absorption

According to the single crystal structure of $DBSQ(OH)_2$, the molecules are packed in a parallel manner with one molecule per unit cell (Figure 4.2). The conjugation backbone of the molecule is planar and the registry of the adjacent molecule features a slip stack (Δx = 3.4 Å and Δy = 2.0 Å) and a short interplanar distance (Δz = 3.4 Å). When dispersed in PMMA solid solutions, we will start by making the simplest of assumptions, that the molecular packing is similar to the slip stacking in the single crystal structure, albeit with a much larger intermolecular distance. Thus, in our aggregate model, we keep Δx and Δy consistent with that of single crystal structure and varied the Δz from 5 Å to 20 Å. Note that we are building the simplest model here. We recognized that the orientation of the

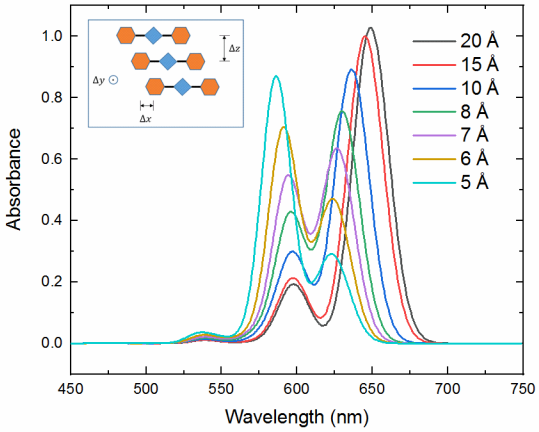

Figure 5.5 Simulated absorption spectra of $DBSQ(OH)_2$ trimer at different Δz, assumed to mimic the SQ aggregates in PMMA films. Inset: packing structure of SQ trimer. Δx = 3.4 Å and Δy = 2.0 Å, consistent with the single crystal structure. Δz is varied from 20 Å to 5 Å, corresponding to the large range of molecular separations in PMMA films.

molecule should be more random and complicated in the PMMA films, which would certainly necessitate more exhaustive computational investigations.

In the ESM model, we consider a trimer of $DBSQ(OH)_2$ due to the computational time restraints of working with larger aggregates. We are aware that the trimer may not be expected to account for the entirety of the aggregates due to its finite size; however, it is an efficient model that takes account of Coulombic interactions well, between adjacent molecules. A small number of time-consuming simulations of larger aggregates consisting of rigid chromophores do not significantly alter the conclusions drawn from the trimer system. The molecules in the trimer are allowed to interact Coulombically via $\hat{V}$ in Equation (5.8) and (5.9). The position of the molecules with respect to others determines their Coulombic interaction, which we have scaled by a dielectric constant (ε) of 3 to account for the screening effect.

The simulated trimer spectra are shown in Figure 5.5. As we can see, the 0-1 (0-0) vibronic peak continuously gains (loses) oscillator strength as Δz decreases. This is consistent with what we have observed in PMMA films. With this simple packing alignment assumption, when comparing Figure 5.5 and Figure 5.4, we think that there exist various types of aggregate in PMMA films, each with a different Δz. For example, in 6 wt% PMMA film, the SQ aggregates can have a large range of Δz and each one has its own contribution to the overall spectra. Thus, even though the average molecular separation is estimated to be 2.3 nm, there will exist SQ aggregates with a Δz of < 1 nm. This is further explored in transition absorption spectroscopy in Chapter 7. Overall, there is a higher population of aggregates with short Δz in concentrated PMMA films, as compared to the dilute films. For 0.01 wt% PMMA film, we think the molecules are well dispersed in the PMMA matrix and there is little aggregate population.

In a short summary, the SQ aggregates in BHJ films and analogous PMMA films do result from intermolecular Coulombic interactions and we assign this type of aggregate as the CC-aggregate. The increased 0-1 vibronic oscillator strength coincides with the expectations of H-aggregate character in the Exciton model as introduced in Section 1.5.2.

5.3.4 Fluorescence of CC-aggregate

Identification of H- and J-aggregates could help to infer the local molecular orientations in the solid state, because this aggregation must arise from changes in intermolecular interactions. The consequences of photophysical properties and photovoltaic performances on aggregation must be explored. Más-Montoya and Janssen[181] have reported that the H- or J-aggregate formation of diketopyrrolopyrrole (DPP) based molecules can be controlled by changing the position of the side chains on the two

peripheral thiophene units. In particular, the DPP-based molecules that form H-aggregates exhibit lower photovoltaic performances than those that form J-aggregates; nevertheless, the exact mechanism is unclear. Hestand *et al*.[29] theoretically investigated the slip stacked 7,8,15,16-tetraazaterrylene (TAT) nanopillars and found that upon transversely sliding the molecules in the aggregates by 0.5 Å, the H-aggregate behavior of the nanopillars is reinforced by the constructive interference between long-range Coulombic coupling and a short-range charge transfer coupling. This then leads to a dramatic improvement in exciton mobility, which is beneficial for many organic optoelectronic applications.

As previously mentioned, the SQ CC-aggregates exhibit similar vibronic intensity redistribution to those predicted for H-aggregates defined by the Exciton model. Historically, the molecular exciton model, which is based on Frenkel excitons, is widely used to investigate the photophysics of molecular aggregates. The exciton model describes the Coulomb-induced splitting of the local, degenerate excited states in an uncoupled aggregate into upper and lower exciton states (as compared to the original monomer excited state). For aggregates with a collinear transition dipole moment alignment, two types of aggregates are categorized according to the sign of the Coulombic coupling term; if the coupling is positive (negative), then the "bright" states, which carry all the oscillator strength, is located at the top (bottom) of the band, leading to formation of an H- (J-) aggregate.[105] For the H-aggregate, the higher excited states are populated after excitation, and then quickly decay to the lowest excited state via molecular vibrations. Since the lowest excited state does not couple to the ground state, fluorescence is inhibited. Suppressed fluorescence is a signature of H-aggregate.[105]

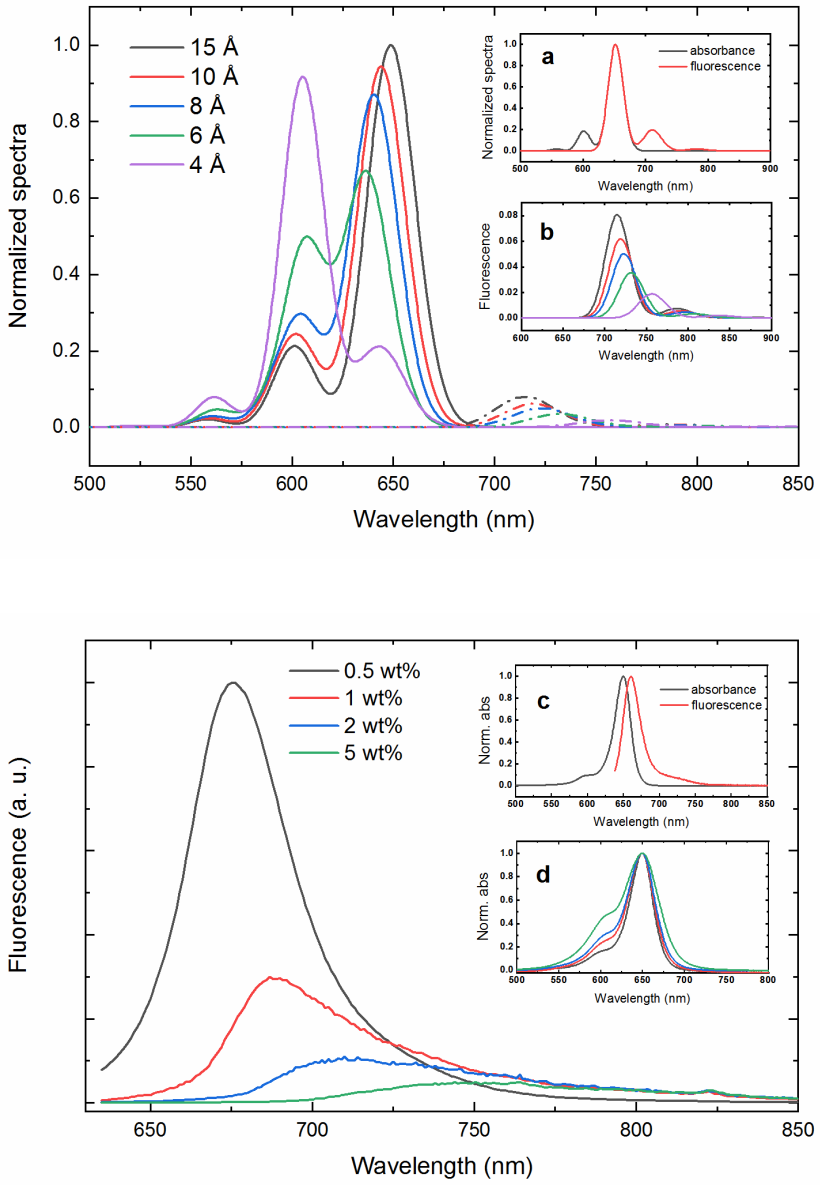

Figure 5.6 Upper panel: simulated absorption (solid lines) and fluorescence (dash-dot lines) spectra of $DBSQ(OH)_2$ *trimer* at different Δz; Lower panel: fluorescence spectra obtained from measuring PMMA films at different weight percent. Inset **a**: simulated monomer absorption and fluorescence spectra. Inset **b**: same fluorescence spectra as in the main figure but with a larger scale. Inset **c**: experimentally obtained monomer absorption and fluorescence spectra. Inset **d**: the absorption spectra of the PMMA films at different weight percent. For simulation: Δx and Δy were set the same as Figure 5.5. Δz is varied from 15 Å to 4 Å. For experiments: the emission spectra were measured in the same conditions for all films.

We performed a theoretical investigation on the fluorescence properties of the CC-dimer (instead of trimer). The fluorescence calculation details have been introduced previously (Section 5.2.3) and the simulated spectrum is shown in the upper panel of Figure 5.6. The absorption spectrum of the dimer demonstrates a vibronic intensity redistribution as the molecules approach each other (i.e. decreasing Δz) in the aggregate, similar to the observation in Figure 5.5. The fluorescence spectrum showed an immediate drop in intensity in the dimer as compared to the monomer (as shown in Inset **a** in Figure 5.6) and the fluorescence quantum yield continues to decrease as molecules become closer (Δz is decreased) (see Figure 5.6 inset **b**), with a concomitant red shift in peak position. This suppressed fluorescence further suggests that the SQ molecules form H-aggregates.

The experimental fluorescence spectra of PMMA films are shown in Figure 5.6 (lower panel). Of note, the PMMA films were made by co-dissolving SQ with PMMA in chloroform solution and then spin casting into thin films. The concentration of PMMA in chloroform was fixed at 40 mg mL^{-1}. At low SQ weight percent, the molecules are considered monodispersed in the films with fixed thickness, and thus each film has the same optical path length. Thus, we view PMMA films as a solid solution of SQ molecules and the molecular separations (and subsequently the intermolecular interactions) are controlled by SQ wt%. Indeed, the absorption spectra (Figure 5.6 Inset **d**) demonstrated that more SQ aggregates are formed in higher SQ wt% films, similar to that observed in Figure 5.3. The fluorescence spectra were measured at the same condition for all films. Consistent with our ESM calculations, the fluorescence intensity decreases quickly (with red-shifted peaks) as the SQ wt% is increased. Yet, the contribution from the inner filter effect[152] (*i.e.* reabsorption of emitted radiation) cannot be ruled out.

Based on a good match between theoretical and experimental observations in Figure 5.6, we conclude that SQ forms H-aggregates in the PMMA films (as well as in the as-cast SQ:PCBM BHJ films). The intermolecular interactions are dominated by the Coulombic coupling between charges on donor and acceptor moieties in adjacent SQ molecules. Hence, the excitons generated in such aggregates should adopt similar properties as the Frenkel excitons.

5.4 Discussion

In this chapter, we use an Essential-state model (ESM) to simulate the SQ monomer and aggregate absorption spectra. First, we introduced the monomer and aggregate Hamiltonian within the ESM. Three diabatic electronic states are used to describe the main charge resonant structure of the SQ monomer. Upon diagonalization, three adiabatic states are obtained, representing the ground, first excited and second excited state. The electronic states are then filled by multiple vibrational levels by considering the vibrational and vibronic Hamiltonians. The monomer absorption spectra can be well reproduced by the complete Hamiltonian in Equation (5.7), demonstrating the accuracy of the ESM in describing the electronic configurations of single SQ molecules in solution.

For SQ thin films, we identified two forms of SQ aggregates; one has a slightly broader absorption spectra than monomers and a higher 0-1 Franck-Condon shoulder and has been observed in as-cast SQ:PCBM blend films as well as in PMMA solid solution films; the other has a much broader absorption spectrum with a “double-hump” profile, which was observed in neat films or annealed SQ:PCBM blend films. By tuning the ESM to account for the intermolecular Coulombic interactions, we have successfully rationalized the

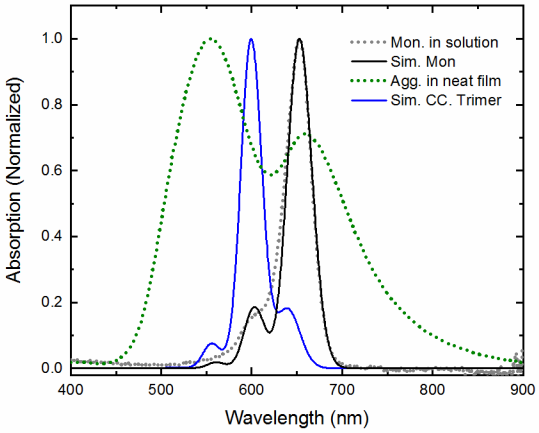

Figure 5.7 Experimental (dotted lines) and simulated (solid lines) absorption spectra of $DBSQ(OH)_2$ monomer and aggregate. The simulation cannot faithfully reproduce the typical SQ aggregate spectrum in neat films, which is much broader and the peak splitting is dramatic as compared to the vibronic spacing (~0.16 eV).

spectral behavior of the first form of aggregates. We conclude that, in PMMA films (or as-cast SQ:PCBM blend films), the SQ molecules exist in H-aggregates with various intermolecular separation, Δz. Each aggregate has its contribution to the overall absorption spectrum.

On the other hand, the Coulombic ESM failed to simulate the typical absorption spectrum of the second form of aggregates. Figure 5.7 shows a simulated absorption spectrum of SQ aggregates with the molecules interacting Coulombically. The calculation was performed by considering the SQ trimer positioned at a geometry consistent with the single crystal structure, which is assumed to be the most stable and compact conformation in which SQ molecules pack. We see that the absorption spectrum of SQ neat films is much broader than the simulated spectrum and the peak spacing is 0.38 eV, significantly larger than the vibronic spacing, ~ 0.16 eV, obtained from simulations.

While several explanations can be given to account for the origin of the spectral line shape of the SQ aggregates in neat films, we found that these arguments are not consistent with the experiments. For example, one might reasonably attribute the two broad peaks to upper and lower Davydov components. Nevertheless, this contradicts the single crystal structure where there is only one molecule per unit cell. Davydov splitting requires oblique transition dipole moment alignments so that the absorption to both symmetric and antisymmetric excited states is allowed. Other explanations are also suggested. For example, one might also assign the two peaks to H- and J-aggregates that are independently formed in the neat films. On the other hand, there might exist another interaction mechanism acting within the single crystal of SQs that causes this panchromatic absorption profile. We look to further test these hypotheses and discover the origin of the broad absorption spectra of SQ neat films in Chapter 6.

Chapter 6. INTERMOLECULAR CHARGE TRASNFER IN SQ AGGREGATES

The Essential-state model (ESM) with Coulomb considerations can successfully rationalize the spectral lineshape of the PMMA films. Yet, it failed to simulate the broad absorption spectra associated with SQ neat films. As discussed above, there might be an additional form of intermolecular interaction when SQ molecules are densely π-stacked. The single crystal structure of the SQs has been introduced in Chapter 4. From this structure, one can see that the donor moiety (nitrogen atom) is near the acceptor moiety (squarylium) of the next molecule in the same stack. We thus hypothesize that the intermolecular charge transfer can effectively occur between neighboring molecules, which modifies the ESM to allow several additional charge-separated (CS) diabatic states. The simulation based on the revised model against the experiments has been proven to be successful, which validates our hypothesis. We assign this new form of SQ aggregate to the "ICT-aggregate". The origin of the two broad absorption peaks in SQ ICT-aggregates has been discussed in detail. Together with Chapter 5, we have developed complete theory to assign the SQ aggregates in solid state films; the CC-aggregate forms when SQ molecules are Coulombically interacting with each other in a loose packing geometry while, when chromophores are sufficiently close, ICT-aggregates are formed. The photophysics of each type of aggregate can be fully explained by the ESM. The work presented in this chapter is based on the collaboration between RIT and Temple University. The initial model was developed by Dr. Nicholas J. Hestand at Temple University and was modified by Chenyu Zheng. The simulation results presented in this chapter were performed based on Chenyu's code, but much credit should certainly go to Nick. The data were used in this chapter with Dr. Hestand's consent.

6.1 Introduction

As previously discussed, the Coulombic coupling is not sufficient to represent the entire intermolecular interactions in SQ single crystals. We note that Tristani-Kendra and Eckhardt[182] have studied the origin of the absorption line shape of a similar SQ molecule, 1,3-bis[4-(N,N-diethylamino)-2-hydroxyphenyl]squaraine (DESQ(OH)). In particular, they assigned the absorption polarized perpendicular to the molecular plane to an intermolecular charge transfer (ICT) interaction. They argued that the slip-stacked crystal packing of DESQ(OH) provides an ideal environment for ICT due to a short interplanar spacing of 3.35 Å. The spatially overlapping molecular orbitals at the donor (nitrogen) and acceptor (squarylium) moieties on neighboring molecules also support the argument. Earlier, Tanaka *et al*.[183] have pointed out how the slipped stack or "staircase" structure is favorable for charge resonance interactions for aggregates of cyanine dyes. Recently, Guasch *et al*.[184] studied the ICT in a dimer of D-A dyads and its effect on optical and electron spin resonance (ESR) spectra. They suggested that the electron delocalization in the dimer system is driven by the subtle "interplay" of intramolecular electron transfer and ICT.

As shown in Figure 4.2, our $DBSQ(OH)_2$ also packs in a slip stacking arrangement in single crystals. The nitrogen atom of one molecule is placed in close proximity to the squarylium of the neighboring molecule. Adding the fact that the interplanar spacing (Δz) is as small as 3.35 Å (Table 4.1), it suggests that the $DBSQ(OH)_2$ (as well as similar SQs such as DPrSQ(OH)2, $DHSQ(OH)_2$, etc.) is a good candidate for ICT. Specifically, the charges can transfer from the nitrogen to the squarylium of the neighboring molecule through molecular orbital overlap. We assert that ICT is responsible for the double-hump

absorption observed in SQ neat films.

In this chapter, we extend the ESM for aggregates to allow for intermolecular charge transfer between molecules. We show that, with the extended model, the double-hump is a result of interplay between intramolecular and intermolecular charge transfer in SQ aggregates. Thus, together with the theoretical modeling in Chapter 5, we provide a comprehensive framework for understanding the nature of the excited states in SQ aggregates, which critically depends on the molecular packing. We hence recognize the huge potential of controlling aggregation in OPV devices towards higher efficiency.

6.2 Models

Intermolecular charge transfer (ICT) necessitates four additional diabatic states to represent the ionized molecule after the charge has been transferred: D^+AD ($|C_1\rangle$), DAD^+ ($|C_2\rangle$), DA^-D ($|A\rangle$) and $D^+A^-D^+$ ($|Z_3\rangle$). Note that $|Z_3\rangle$ is a cationic state holding a zwitterion. Since we consider that the total aggregate must remain as a neutral-charge entity during a photoexcitation, the charge-separated (CS) states always exist in pairs (an anionic state and a cationic state). These four CS diabatic states are produced by ICT from the original three neutral diabatic states. Thus, the ESM has been extended to account for a total of seven diabatic states. Such ionic species are expected to affect the optical properties of the material as it couples directly to the optically active exciton state.

We further define the energy of the infinitely separated anionic ($|A\rangle$) and cationic ($|C_1\rangle$ or $|C_2\rangle$) pair to be η_{CT}. For simplicity, we approximate the energy of an infinitely separated $|Z_3\rangle$ and $|A\rangle$ pair to be $\eta_{CT} + \eta_Z$, adding the energy required to create a zwitterion on the neutral arm of a cation in a $|C_1\rangle$ (or $|C_2\rangle$) and $|A\rangle$ CS pair. While this approximation is not

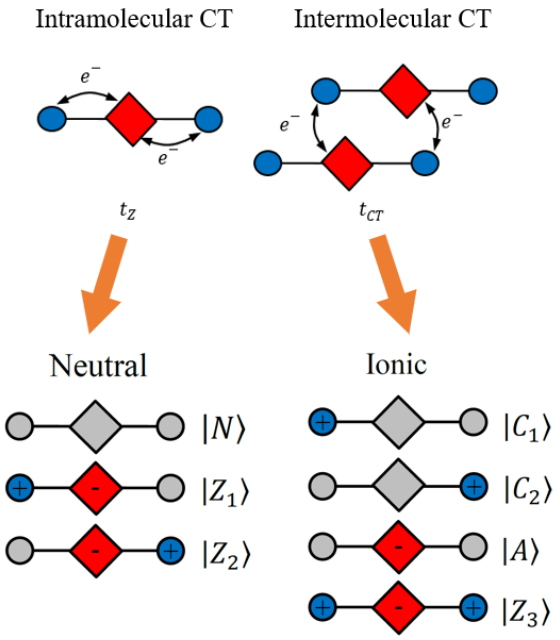

Figure 6.1 An illustration of the intramolecular (left) and intermolecular (right) charge transfer for squaraines in the upper panel, and the resulting total of seven diabatic states in the bottom panel. The rhombus represents the squarylium and the circle denotes the nitrogen atom.

rigorous, it reduces the number of adjustable parameters in the model and should be a suitable estimate. The total energy of the CS pair is also influenced by the distance dependent Coulomb interaction through the Coulomb operator $\hat{V}$. The neutral states and CS states couple through an intermolecular charge transfer integral, t_{CT}, which describes the transfer of an electron between overlapping donor and acceptor moieties on neighboring molecules, as shown in Figure 6.1. Last but not the least, the equilibrium nuclear geometries of the ionic states are defined by an ionic HR factor, λ_{CT}^2. Since we expect that the geometric rearrangement of the ionic species is smaller compared to the zwitterion, λ_{CT}^2 is simply set to the half of the λ_z^2, in line with the expectation that the geometric rearrangement of the ionic states is smaller than that of the zwitterionic states.[185]

Now, the complete Hamiltonian for the ICT-aggregates reads:

$$\widehat{H}_{ICT}^{Agg} = \widehat{H}_{CC}^{Agg} + \widehat{H}^{CS} + \widehat{H}^{inter} \tag{6.1}$$

where $\widehat{H}_{CC}^{Agg}$ has been introduced in Equation (5.9); $\widehat{H}^{CS}$ is the Hamiltonian for CS states and $\widehat{H}^{inter}$ represents the ICT term that couples the neutral and CS states.

The Hamiltonian for the additional CS states can be written as a sum of the electronic and vibronic terms can be written as

$$\widehat{H}^{CS} = \widehat{H}_{el}^{CS} + \widehat{H}_{el-vib}^{CS} \tag{6.2}$$

It should be noted that the vibrational energy of the CS states is accounted for in the $\widehat{H}_{CC}^{Agg}$ term in Equation (6.1). The electronic Hamiltonian for CS states is given by

$$\widehat{H}_{el}^{CS} = \eta_{CT} \sum_{n} |A_n\rangle\langle A_n| + \eta_Z \sum_{n} |Z_{3,n}\rangle\langle Z_{3,n}| - t_Z \sum_{a,n} \left(|Z_{3,n}\rangle\langle C_{a,n}| + h.c.\right) \tag{6.3}$$

where n runs over all the molecules in the aggregates. Since the aggregate remains charge neutral before and after excitation, the anions and cations must exist in pairs. Thus, the first term counts the number of CS pairs. The energy of a CS pair composed of one molecule in the anion state $|A\rangle$ and the other molecule in the cation state, $|C_1\rangle$ or $|C_2\rangle$ is η_{CT}, while the $|A\rangle$ $|Z_3\rangle$ pair has an additional energy of a zwitterion, η_Z. The third term describes the *intramolecular* charge transfer that transforms a cationic state ($|C_1\rangle$ or $|C_2\rangle$) to the $|Z_3\rangle$ state, via a intra-CT integral of t_Z.

The vibronic Hamiltonian that couples the electronic and nuclear degrees of freedom is

$$\begin{aligned} \widehat{H}_{el-vib}^{CS} = {} & \hbar\omega_{vib}\lambda_{CT} \sum_{n,a} \left(b_{a,n}^{\dagger} + b_{a,n} + \lambda_{CT}\right)\left(|C_{a,n}\rangle\langle C_{a,n}| + |A_n\rangle\langle A_n|\right) \\ & + \hbar\omega_{vib}\lambda_Z \sum_{n,a} \left(b_{a,n}^{\dagger} + b_{a,n} + \lambda_Z\right)|Z_{3,n}\rangle\langle Z_{3,n}| \end{aligned} \tag{6.4}$$

where the potential energy surfaces (PES) of the CS states are shifted by the ionic HR factor, λ_{CT}^2. Note that while the cation only influences the molecular arm where it resides, the anion is considered to affect both arms. We treat the PES shift of anion and cation states with the same ionic HR factor to reduce the adjustable parameters. We do not expect the exact value of the ionic HR factor to have a large effect on our main results. Finally, the second term in Equation (6.4) describes the PES shift of the $|Z_3\rangle$ state, for which we considered both arms hold a zwitterion (with the zwitterionic Huang-Rhys factor, λ_Z^2).

The ICT term, $\widehat{H}^{inter}$, in Equation (6.1) can be expressed as

$$\begin{aligned}\widehat{H}_{el}^{inter} = \\ -t_{CT}\sum_n \big(&|N_nN_{n+1}\rangle\langle A_nC_{1,n+1}| + |N_nN_{n+1}\rangle\langle C_{2,n}A_{n+1}| \\ &+ |A_nC_{1,n+1}\rangle\langle Z_{2,n}Z_{1,n+1}| + |C_{2,n}A_{n+1}\rangle\langle Z_{2,n}Z_{1,n+1}| \\ &+ |Z_{1,n}Z_{1,n+1}\rangle\langle C_{1,n}A_{n+1}| + |Z_{2,n}Z_{2,n+1}\rangle\langle A_nC_{2,n+1}| \\ &+ |Z_{3,n}A_{n+1}\rangle\langle Z_{1,n}N_{n+1}| + |A_nZ_{3,n+1}\rangle\langle N_nZ_{2,n+1}| + h.c.\big)\end{aligned} \tag{6.5}$$

which describes all possible movements of electrons between molecules. While Equation (6.5) is somewhat cumbersome to write down, its physical meaning is intuitive. In our model, the squaraines are slip stacked from left to right as the index n increases, thus, electrons transfer between molecules from the right arm of the molecule with index n and the left arm of molecule having index $n+1$. For example, the electron can be transferred from the right nitrogen atom of the molecule n to the central squarylium of the molecule $n+1$, resulting in a coupling between the initial state $|N_nN_{n+1}\rangle$ and the final state $|A_nC_{1,n+1}\rangle$ via an inter-CT integral, t_{CT}, as expressed by the first term of Equation (6.5).

The calculation of the oscillator strength and absorption spectra are the same as described in Section 5.2.3. Of note, CS states (including $|Z_3\rangle$ state) does not have transition

dipole moments and their impact on absorption spectra lies in their ability to couple to the three neutral states shown in Figure 6.1.

6.3 Experiments and Simulations

6.3.1 SQ aggregates in mixed solvent solutions

As previously shown in Figure 5.7, the ESM dimer with Coulomb interaction cannot reproduce the absorption spectra of the neat films of $DBSQ(OH)_2$ (and other linear-chain SQ molecules). The broadening of the absorption spectrum into the double hump is often found in similar anilinic squaraines with linear N-alkyl chains. In literature, many attribute it to existence of different SQ polymorphs in the neat films, and therefore the coexistence of H- and J-aggregates.[149,172–175] Although these interpretations contradict to the SQ single crystal structures, we look further evidences to interpret the unique absorption spectra of SQ aggregates in neat films.

We turn our attention to the $DBSQ(OH)_2$ aggregates formed in mixed solvents where a nice transformation from monomers to aggregates can be controlled by changing solvent quality or temperature. In the mixed solvent work, we dissolve the squaraine in a mixture of solvents containing dimethyl sulfoxide (DMSO) and H_2O. DMSO is a good organic solvent with a high solubility for SQ, and is miscible with H_2O (a non-solvent for SQs) to form a uniform solvent environment.[186] As the solvent quality is controlled by changing the ratio of the two solvents, a transformation between monomers and aggregates can be observed (see Figure 6.2a). The absorption spectra of the SQ aggregates formed in mixed solvents mimic those of the neat films, indicating that both aggregates have the same structure and packing. The photoluminescence spectra of the mixed solvent solution during

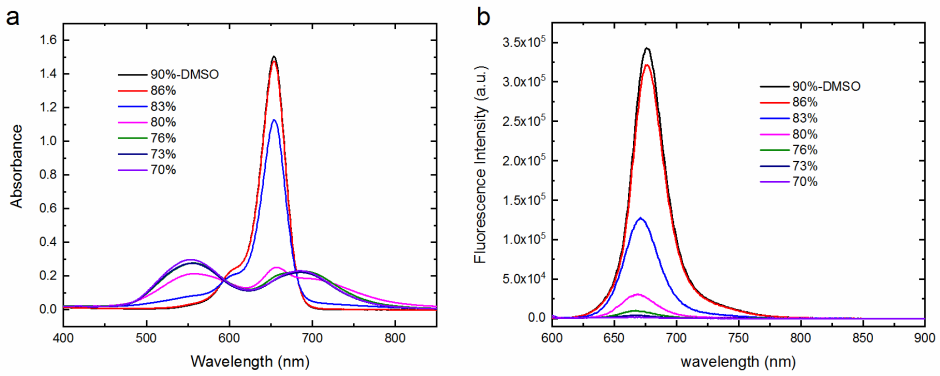

Figure 6.2 The **a**) absorption and **b**) photoluminescence spectra of $DBSQ(OH)_2$ in $DMSO:H_2O$ solvent mixtures measured as a function of solvent quality change. For photoluminescence spectra, the solvent mixture was excited at 595 nm.

such transformations are shown in Figure 6.2b. As the monomer population decreases, the monomer absorption peak disappears, as does the fluorescence. Any fluorescence emission for a J-aggregate would be seen as transitions to the bottom of the exciton band are optically allowed. We stress how the lack of fluorescence must contradict an assignment of the low energy peak to a J-aggregate (as well as to a monomer) and we present an alternative, more accurate assignment based on our ESM and intermolecular charge transfer consideration.

Using solvent mixtures of 80% DMSO:20% H_2O (by volume) for $DBSQ(OH)_2$, the absorption spectra show the coexistence of monomers and aggregates. Then the mixed solvent solutions were heated up to 65 ^{0}C and with this temperature increase, the SQ molecules should be entropically driven to separate from aggregates into monomers. Indeed, from room temperature, 25 ^{0}C, to 65 ^{0}C, a gradual increase in monomer absorption is seen in Figure A3 with a concomitant decrease in the double hump at ~540 nm and ~710 nm. Two isosbestic points at 595 nm and 672 nm can be clearly identified, which serves as strong evidence for the inter-conversion between monomer and a single form of aggregate

(with a double hump absorption feature). Similar experiments have been performed for other squaraines and the results are similar to those of $DBSQ(OH)_2$.

6.3.2 Simulation of SQ ICT-aggregate

The simulated spectra based on Equation (6.1) are shown in Figure 6.3 with a narrow absorption line width (0.05 eV) to resolve all the subpeaks. In the model, we again consider a dimer as an effective representative of SQ aggregates in the solvent mixture due to the computational restraints (as now four additional diabatic states are activated by ICT). For both simulated curves (with only CC, and with both CC and ICT), the dimer geometry is consistent with the single crystal structure. As compared to the ESM when only considering Coulombic coupling (blue curve), the influence of ICT is immediately seen as this spectrum contains a substantial contribution of low energy components filled out with vibronic structures (red curve). The high energy peak is further blue shifted and the whole collection of spectral features is reminiscent of the experimental spectrum. As we broaden the Gaussian lineshape to 0.15 eV, the simulated absorption spectrum is greatly consistent with the spectra of $DBSQ(OH)_2$ in solvent mixtures of $DMSO:H_2O$ as shown in the left of Figure 6.3, demonstrating the critical contribution of ICT on excited state configurations of SQ aggregates that exist in neat films and solvent mixtures.

We have also simulated the absorption spectra of other SQ aggregates, i.e. $DPrSQ(OH)_2$ and $DHSQ(OH)_2$, based on Equation (6.1) and the parameters are listed in Table 6.1. For the simulation, the dimer geometry was set in accord with the single crystal structure while only η_{CT} and t_{CT} were taken as adjustable parameters (note that η_z and t_z are parameterized based on the SQ monomer spectrum simulation as well as the literature[107,108]), which were set to the values that best reproduce the experiments. We stress

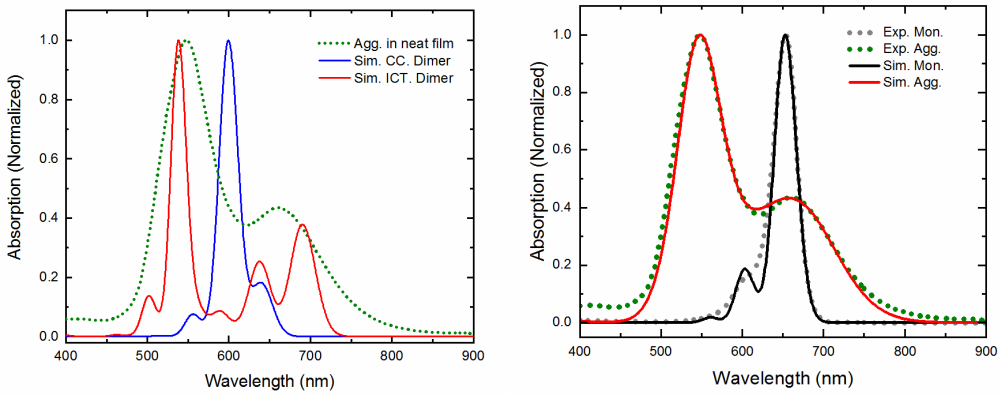

Figure 6.3 Comparison between experimental (dotted line) and simulated (solid line) absorption spectra. Left: a narrow line shape is used to resolve all vibronic structures. Right: an optimized line shape is used to achieve a best fit of the experiments. The blue line is simulated by using Equation (5.9), only considering Coulombic interactions, while the red line is simulated by using Equation (6.1), where both Coulombic interactions and intermolecular charge transfer are considered. The experimental spectrum is obtained from DMSO:H_2O mixed solvent solution. All spectra are normalized to the absorption maximum.

that a consistent Gaussian line width of 0.15 eV was taken for the entire spectrum and the broad peaks in the experiments are due to the overlapping of vibronic structures.

We also found that η_{CT} is largely responsible for the relative peak height of the two "humps" (i.e. as the η_{CT} is increased, the oscillator strength is redistributed to the low-energy peak), while t_{CT} greatly controls the peak spacing (i.e. t_{CT} is large when two peaks are far part in the spectrum). For comparison, the magnitude of the intermolecular charge transfer integral, t_{CT} follows the order of DPrSQ(OH)$_2$ > DBSQ(OH)$_2$ > DHSQ(OH)$_2$, which is in agreement with the far-split absorption peaks in absorption spectra of DPrSQ(OH)$_2$ neat films as compared to other two SQs (Figure 4.3). Thus, DPrSQ(OH)$_2$ appears to couple more strongly to the ICT state than the SQs with longer side groups, which is consistent with the shorter nearest-neighbor donor-acceptor distance observed in

DPrSQ(OH)$_2$ single crystals. Note that the t_{CT} obtained from the dimer simulation is considered as an effective value that represents the upper bound of the true values. In large aggregates, most molecules have two nearest neighbors to which each can couple, while only one coupling is counted in the dimer model. In real case, a smaller t_{CT} is enough to represents the intermolecular charge transfer strength and to reproduce the absorption spectra of the aggregates.

Table 6.1 Essential-state parameters for DPrSQ(OH)$_2$, DBSQ(OH)$_2$ and DHSQ(OH)$_2$. The monomeric parameters are the same for all three SQs while the main differences lie in the energy of the charge separated states, η_{CT}, and the intermolecular charge transfer integral, t_{CT}, which are underlined.

Parameter	DPrSQ(OH)$_2$	DBSQ(OH)$_2$	DHSQ(OH)$_2$
η_z	0.69 eV	0.69 eV	0.69 eV
t_z	1.05 eV	1.05 eV	1.05 eV
λ_Z^2	1	1	1
η_{CT}	<u>1.42 eV</u>	<u>1.37 eV</u>	<u>1.53 eV</u>
t_{CT}	<u>0.55 eV</u>	<u>0.34 eV</u>	<u>0.30 eV</u>
λ_{CT}^2	0.5	0.5	0.25
$\hbar\omega_{vib}$	0.16 eV	0.16 eV	0.16 eV
Line width	0.15 eV	0.15 eV	0.15 eV
Spectral shift	-0.087 eV	0.006 eV	0 eV

6.4 Discussion

In this chapter, we have faithfully reproduced double-hump absorption spectra of SQ aggregates in neat films with the special consideration of intermolecular charge transfer (ICT). Yet, the exact origin for such peak splitting and vibronic structures in Figure 6.3 is

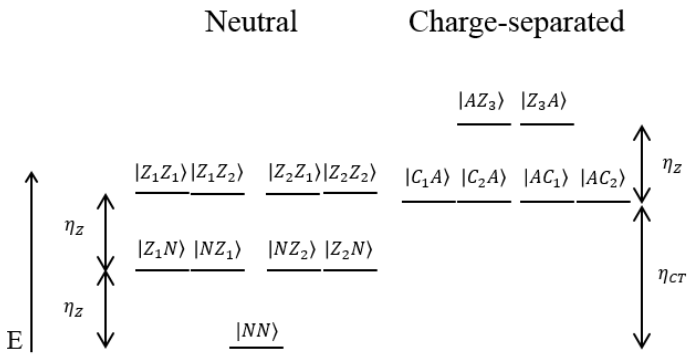

Figure 6.4 Energy diagram of rigid dimer diabatic states. The neutral states are shown on the left while the CS states are shown on the right, indicated with the energy difference between each state. The CS states are approximately located near the double zwitterionic states, given that $\eta_{CT} \approx 2\eta_Z$.

less clear. As mentioned previously, the new ionic states do not have transition dipole moment and their contribution to the spectrum is entirely due to their ability to couple to the original neutral excitonic states. Here, we build a rigid (*i.e.* vibrationless), non-interacting (*i.e.* without intermolecular interactions) dimer model to mechanistically understand the spectral lineshape of SQ ICT-aggregate. In this simple model, only electronic Hamiltonian is considered to investigate how the ionic states mixes with the neutral excitonic states.

The Hamiltonian for rigid, non-interacting dimer model can be written as:

$$\hat{H}_{el}^{ni} = \sum_{n} \left(\hat{H}_{el,n}^{neu} + \hat{H}_{el,n}^{CS} \right) \tag{6.6}$$

where n runs from 1 to 2 for the dimer. In Equation (6.6), we only consider the seven electronic states for the (charge neutral) dimer. The Coulomb and intermolecular charge transfer coupling terms ($\hat{V}$ and $\hat{H}_{el}^{inter}$) are neglected. Also neglected are the vibrational

and vibronic coupling terms. Thereafter, the Hamiltonian in Equation (6.6) only contains 15 possible diabatic dimer states: $|NN\rangle$, $|NZ_1\rangle$, $|NZ_2\rangle$, $|Z_1N\rangle$, $|Z_1Z_1\rangle$, $|Z_1Z_2\rangle$, $|Z_2N\rangle$, $|Z_2Z_1\rangle$, $|Z_2Z_2\rangle$, $|C_2A\rangle$, $|AC_1\rangle$, $|C_1A\rangle$, $|AC_2\rangle$, $|Z_3A\rangle$ and $|AZ_3\rangle$. Their energies are shown in Figure 6.4. Here, we take the order within the ket to denote the molecule number. For example, the ket $|NZ_1\rangle$ defines the first molecule in state N and the second molecule is in the state of Z_1. The first nine states that represent both molecules in the dimer are neutral, and the remaining six states are cation-anion pairs. While t_Z is considered in the model (in $\widehat{H}_{el,n}^{neu}$) for the mixing of $|N\rangle$, $|Z_1\rangle$ and $|Z_2\rangle$ states, t_{CT} is neglected and thus the CS-dimer states do not mix with the charge neutral states.

Eigenstates and eigenvalues can be obtained by diagonalizing Equation (6.6). The lowest-energy state is defined as the ground state, while all the higher excited states are considered excited states (although some of them are only two-photon allowed). We begin to evaluate the symmetry of the adiabatic electronic states. This involves taking the direct product of the monomeric diabatic states of the two chromophores, in terms of a symmetric (S) and antisymmetric (AS) linear combination of the states with respect to inversion. Based on inversion symmetry, we can separate some degenerate electronic states. Thus, the nine neutral adiabatic eigenstates can be expressed as: $|gg\rangle^S$, $|gc\rangle^S$, $|gc\rangle^{AS}$, $|ge\rangle^S$, $|ge\rangle^{AS}$, $|cc\rangle^S$, $|ce\rangle^S$, $|ce\rangle^{AS}$ and $|ee\rangle^S$, and the six ionic eigenstates are: $|ac_1\rangle^S$, $|ac_1\rangle^{AS}$, $|ac_2\rangle^S$, $|ac_2\rangle^{AS}$, $|ac_3\rangle^S$ and $|ac_3\rangle^{AS}$. Note that the phase of the molecule is defined such that the first and second molecule in the dimer are symmetric under inversion. For ionic adiabatic states, a and c represents general anionic and cationic states, while index 1 to 3 indicates the energy of the states from low to high (and should be differentiated from the number in diabatic states, e.g. $|Z_1\rangle$).

The eigenvalue (i.e. energy) of each state can be calculated and here we only listed several states of interests:

$$E^{(0)}_{|gc\rangle^S} = E^{(0)}_{|gc\rangle^{AS}} = (1+\rho)\eta_Z + 2t_Z\sqrt{2\rho(1-\rho)} \tag{6.7}$$

$$E^{(0)}_{|ac_1\rangle^S} = E^{(0)}_{|ac_1\rangle^{AS}} = \eta_{CT} + \rho\eta_Z + 2t_Z\sqrt{2\rho(1-\rho)} \tag{6.8}$$

$$E^{(0)}_{|ac_2\rangle^S} = E^{(0)}_{|ac_2\rangle^{AS}} = \eta_{CT} \tag{6.9}$$

$$E^{(0)}_{|ac_3\rangle^S} = E^{(0)}_{|ac_3\rangle^{AS}} = \eta_{CT} + (1-\rho)\eta_Z - 2t_Z\sqrt{2\rho(1-\rho)} \tag{6.10}$$

By transforming the transition dipole moment matrix, $\hat{\mu}$, into the symmetrized basis, we found that only one excited state, $|gc\rangle^{AS}$, has a significant transition dipole moment from the ground state $|gg\rangle^S$. Without $\hat{H}_{el}^{inter}$ (which contains the t_{CT} term), all six CS states do not couple to the original nine exciton states and thus do not carry oscillator strength and in the absence of CS states, the $|gc\rangle^{AS}$ state is solely responsible for the absorption lineshape, resulting in the spectrum shown as the blue line in Figure 6.3. Thus, in order to understand the origin of the double-hump absorption profile, we need to investigate how this $|ge\rangle^{AS}$ state mixes with the CS states.

Only the states of the same symmetry can couple and the coupling strength is weak when two involved states are far apart in energy. Thus, $|gc\rangle^{AS}$ can couple to $|ac_1\rangle^{AS}$, $|ac_2\rangle^{AS}$ and $|ac_3\rangle^{AS}$. We have calculated the energies of these four states, as shown in Equations (6.7)-(6.10). $|ac_1\rangle^{AS}$ is the lowest-energy ionic state, but still significantly higher in energy than $|gc\rangle^{AS}$ as $\eta_{CT} \gg \eta_Z$. Thus, the coupling between $|gc\rangle^{AS}$ and $|ac_1\rangle^{AS}$ is small in the non-interacting dimer based on Equation (6.6).

Nevertheless, upon addition of the $\hat{V}$ term in Equation (6.6), the ionic states are stabilized by the Coulomb potential. For example, the energy of $|AC_1\rangle$ states is lowered by

the positive-negative large interaction between molecules. As a result, the energy of $|ac_1\rangle^{AS}$ is close to that of the $|gc\rangle^{AS}$ state.

These two states couple via a matrix element, $\tau = 2t_{CT}t_Z/\sqrt{\eta_Z^2 + 8t_Z^2}$. The general form of the two diagonal states can be written as

$$a|gc\rangle^{AS} - b|ac_1\rangle^{AS} \tag{6.11}$$

$$b|gc\rangle^{AS} + a|ac_1\rangle^{AS} \tag{6.12}$$

where a and b are coefficients determined by the energy difference between $|gc\rangle^{AS}$ and $|ac_1\rangle^{AS}$ and the matrix element. Since $|gc\rangle^{AS}$ carries all the oscillator strength from the ground state, the weight of the $|gc\rangle^{AS}$ (square of the coefficient) in each diagonal state determines the oscillator strength from the ground state.

Thus, in absence of ICT interactions, the squaraine molecules form H-aggregates (consistent with the face-to-face stacking structure in single crystals) and the antisymmetric $|gc\rangle^{AS}$ state is the only optically allowed "bright" state. When ICT is activated, the $|gc\rangle^{AS}$ state strongly mixes with the charge separated state $|ac_1\rangle^{AS}$, and the resulting two diagonal states are both optically allowed (due to the $|gc\rangle^{AS}$ components in each state), leading to the unique double hump absorption spectra. Note that the coupling between other states is also possible even though the energy difference might be large, leading to a more complicated structure of electronic states for squaraine aggregates. Nevertheless, our simple non-interacting rigid dimer model provides a qualitative, reliable understanding of the origin of the double peaked absorption spectrum for SQ aggregates in neat films and solvent mixtures.

Chapter 7. INVESTIGATION OF EXCITED STATE DYNAMICS IN SQ AGGREGATES USING A TRANSIENT ABSORPTION SPECTROSCOPY

In this chapter, the excited state dynamics of fully solvated $DBSQ(OH)_2$ in chloroform solution, as well as the $DBSQ(OH)_2$ monomers and CC-aggregates formed in PMMA solid solution films were investigated using femtosecond transient absorption (TA) spectroscopy. The results demonstrated an efficient transfer of excitations from SQ monomer to CC-aggregates in the films, leading to a shortening of the monomer excited state lifetime. Singlet-singlet annihilation is also observed in both $DBSQ(OH)_2$ monomers as well as the CC-aggregates in PMMA films, indicating the excitations are highly mobile in such systems. The results suggest that the excitons can efficiently diffuse to the $DBSQ(OH)_2$:PCBM interface even in the amorphous, mixed domains containing both monomers and CC-aggregates, which may then explain the high power conversion efficiency achieved in the as-cast BHJ films. The TA experiments and data analysis were performed by Michael Mark in McCamant's lab at University of Rochester. The data were used in this chapter with Michael Mark's consent.

7.1 Introduction

Molecular aggregates may exhibit drastically different photophysical and transport properties when packed in different orientations. As discussed in Chapter 1, for the widely accepted exciton model,[105] the molecular Coulomb coupling splits the excited state of the monomer. For molecules packed in a "face-to-face" ("head-to-tail") geometry, the higher (lower) excited state is optically bright while the lower (higher) excited state is dark, and this aggregate is referred to as an H- (J-) aggregate. Fast exciton diffusion has been often reported for the J-aggregates of several molecular systems, including the perylene bisimide,[187] cyanine dyes[188] and oligomers[63], due to the ease of detecting fluorescence from the lowest Frenkel state of the J-aggregate. Thus, it is often believed that the J-aggregation would benefit exciton diffusion in OPVs.[181] Nevertheless, recent studies have demonstrated that the H-aggregate can also support fast exciton diffusion.[189]

Furthermore, recent theoretical studies[185,190,191] by Nicholas Hestand and Frank Spano have shed light on the molecular aggregates using theory that goes beyond Kasha's H- and J-aggregate description. The intermolecular interactions in such slightly more complicated aggregate systems include both long-range Coulombic coupling as well as short-range charge transfer coupling, and the interference between the two dramatically alters the exciton transport properties.[29] Their work provides a new perspective that the exciton diffusion in aggregates are largely controlled by the nature of the intermolecular interactions.

Exciton diffusion is a fundamental step that greatly impacts OPV performance and therefore the effect of material aggregation on remains a critical topic of ongoing study. In particular, the exciton generated in the aggregate can be delocalized over a few neighboring

molecules via intermolecular coupling, which benefits the exciton diffusion and dissociation in organic photovoltaic devices.[190,192] Wei *et al.* have reported a nearly 3-fold enhancement in exciton diffusion length in thermally annealed SQ:fullerene films, which was attributed to improvements in crystal packing and SQ aggregation. In addition, Bruck *et al*.[149] and Chen *et al*.[104] have individually reported a beneficial J-aggregate formation in SQ-based organic solar cell devices. Nevertheless, in these papers as well as many other studies[134,175,193], the formation of aggregates and the improving OPV performances are considered to be separate or are considered as two individual experimental observations. Even when it appears that they are strongly correlated, the mechanistic details connecting these two observations is still lacking to this date.[193–196]

In this chapter, we investigate the excited state properties in $DBSQ(OH)_2$ aggregates with femtosecond transient absorption spectroscopy. The aggregates of $DBSQ(OH)_2$, as discussed previously, exist ubiquitously in the thin films. By changing the SQ-fullerene blend ratio or when applying a thermal annealing treatment, the SQ absorption can be tuned from a spectrum that is slightly broader (with a higher 0-1 vibronic peak) when compared to monomer absorption to a spectrum that is much broader with a double hump feature (Figure 4.4). The different absorption spectra will later be explained by the nature of the intermolecular interactions, based on theoretical investigations in previous chapters. The former broadened "single hump" absorption is a CC-aggregate in which the Coulombic coupling dominates the intermolecular interactions, while the latter double hump is associated with ICT-aggregates, recognizing that the intermolecular charge transfer also exerts a significant influence on the excited states of the aggregate.

When the CC-aggregate dominates the SQ populations in the $DBSQ(OH)_2$:PCBM as-

cast films, the thin film XRD (Figure 4.6) demonstrates that films are essentially amorphous. However, we found that the amorphous as-cast films produce the most successful OPVs with efficiency >5%. Thus, the exciton diffusion and dissociation are expected to be at high yield for efficient photoinduced-charge generation. Here, we test the power-dependence of the transient absorption decay to study the singlet-singlet annihilation phenomenon in the $DBSQ(OH)_2$ films. The results show that not only are the excitons highly mobile in the monomer and CC-aggregates, but that the energy can be transferred from the monomer to CC-aggregates as described with ultrafast kinetics. These results provide insight as to how such a high power conversion efficiency can be achieved in amorphous as-cast BHJ films for $DBSQ(OH)_2$ and $PC_{71}BM$ blends.

7.2 Transient Absorption Studies of SQ Solution and PMMA Films

As introduced in Chapter 6, the SQ molecules form CC-aggregates when dispersed in PMMA solid solutions. The Coulomb interaction in the aggregate couples the electronic states of individual molecules, leading to H-aggregate-like spectral behavior, i.e. blue-shifted absorption peaks with increasing 0-1 vibronic oscillator strength (Figure 5.4). The steady state absorption spectra of PMMA films with different SQ weight percent have been shown in Figure 5.4. As have been discussed in Chapter 5, the molecular separation distance is decreased as the weight percent of SQ is increased (Table 5.2). Thus, the intermolecular coupling strength between SQ chromophores is stronger in more concentrated PMMA films. Hence, the impact of the coulombic interaction on exciton dynamics can be investigated by comparing the transient absorption results from the

PMMA films with the steady state absorption spectra, which steadily broaden as the contribution of coulombic interaction increases with SQ concentration.

7.2.1 Transient absorption of SQ in solution and in dilute PMMA films

The transient absorption spectra for fully solvated $DBSQ(OH)_2$ monomers in chloroform solution are shown first in Figure 7.1. At early times, At early times, the spectral region of negative change in absorption (ΔOD) mirrors the steady state absorption spectra with a peak at 650 nm. This similarity with the steady-state absorption is explained given that this region is dominated by the ground state bleach (GSB), demonstrating the depopulation of the monomer ground state. There is some contribution from stimulated emission (SE); we note that the steady-state fluorescence peaks at 660 nm, only ~10nm or ~230 cm^{-1} Stokes-shifted from absorption peak. After 5 ps, a slight red-shift of the negative ΔOD peak is seen, the shift being attributed to the stabilization of excited states by solvent reorganization. Two excited state absorption (ESA) bands are seen at 440 nm and 500 nm, corresponding to the $S_1 \rightarrow S_n$ transitions.

The transient signal dynamics of the SQ monomer at 440 nm (ESA peak), 503 nm (ESA peak), 652 nm (GSB peak) and 675 nm (SE peak) are plotted in Figure 7.1b. All the decays can be fitted by a slow time constant of 2.7 ns, and three fast time constants, 200 fs, 1.63 ps, and 11ps. The decays are fit with small amplitudes for the fast components, consistent with the observation of the small and fast loss in kinetic traces, apparent at early times in Figure 7.1b). The fast time constants can be assigned to the solvent and internal reorganization, in accord with the growth of signal at 675 nm, the SE region, due to the dynamic Stokes Shift. The slow time constant is consistent with the fluorescence lifetime measured from TCSPC (*i.e.* 2.3 ns).[197] Transient polarization anisotropy decays via

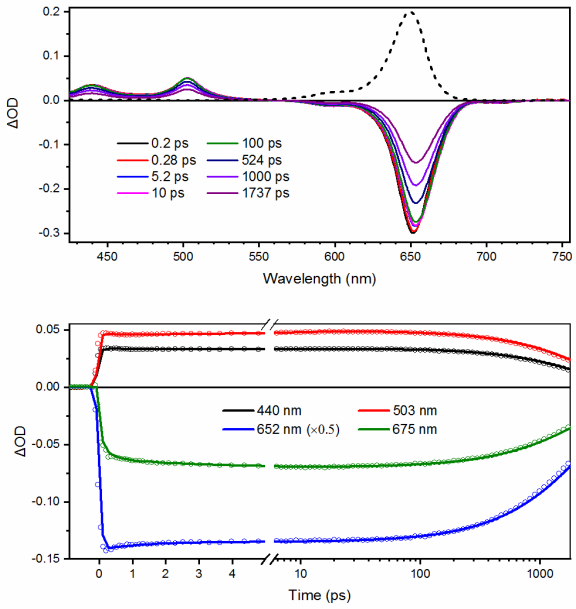

Figure 7.1 Transient absorption spectra (top) and the corresponding kinetic traces (bottom) of $DBSQ(OH)_2$ in chloroform solution after excitation at 640 nm. The steady state absorption spectrum is shown in the dashed line in the top panel. The kinetic traces (at the ESA, GSB and SE peaks) are plotted against a linear time axis for the first 5 ps and a logarithmic time axis for the remaining time period of study (i.e. 6 ~ 1700 ps).

molecular rotation in solution. The transient polarization anisotropy is measured, and seemingly decays via molecular rotation in solution. The rotational correlation time is measured to be 220 ps, which is consistent with the reported values for an indo-based SQ.[198]

The transient absorption spectra of a very dilute PMMA film (0.01 SQ wt%) and the corresponding decay kinetics are shown in Figure 7.2. The spectra are similar to those of the monomer solution in Figure 7.1. However, no fast time constants on a femtosecond scale are observed in the decay dynamics. This is likely due to the rigid PMMA matrix that hinders any structural reorganization of the SQ molecules after excitation. The kinetics are fit well with two time constants of 52 ps and 2.7 ns. The total decay time constant is the

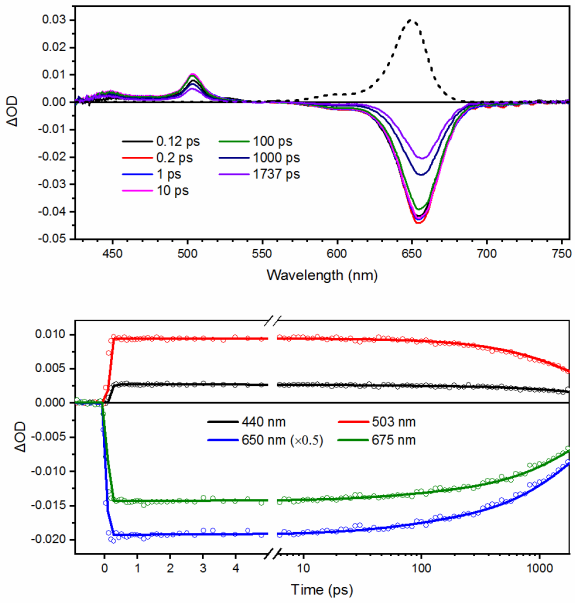

Figure 7.2 Transient absorption spectra (top) and the corresponding kinetic traces (bottom) of $DBSQ(OH)_2$ in 0.01wt% PMMA films after excitation at 640 nm. The steady state absorption spectrum is shown in the dashed line in the top panel. The kinetic traces (at ESA, GSB and SE peaks) are plotted plotted against a linear time axis for the first 5 ps and against a logarithmic time axis for the remaining time period of study (i.e. 6 ~ 1700 ps).

same as that measured for the $DBSQ(OH)_2$ solution, demonstrating that PMMA is a non-interacting medium. In addition, the chromophores in the dilute film are sufficiently far apart (the intermolecular distance of SQs in 0.01 wt% PMMA film is estimated to be ~ 20 nm, see Table 5.2) such that they can be viewed as monomers (with the same photophysical properties as the fully solvated $DBSQ(OH)_2$ monomers in solution) that are "dissolved" in the polymer matrix. Thus, any changes in the photophysical properties of SQs in more concentrated PMMA films can be attributed to the intermolecular interactions as chromophores are closer to each other.

7.2.2 Transient absorption of SQ in concentrated PMMA films

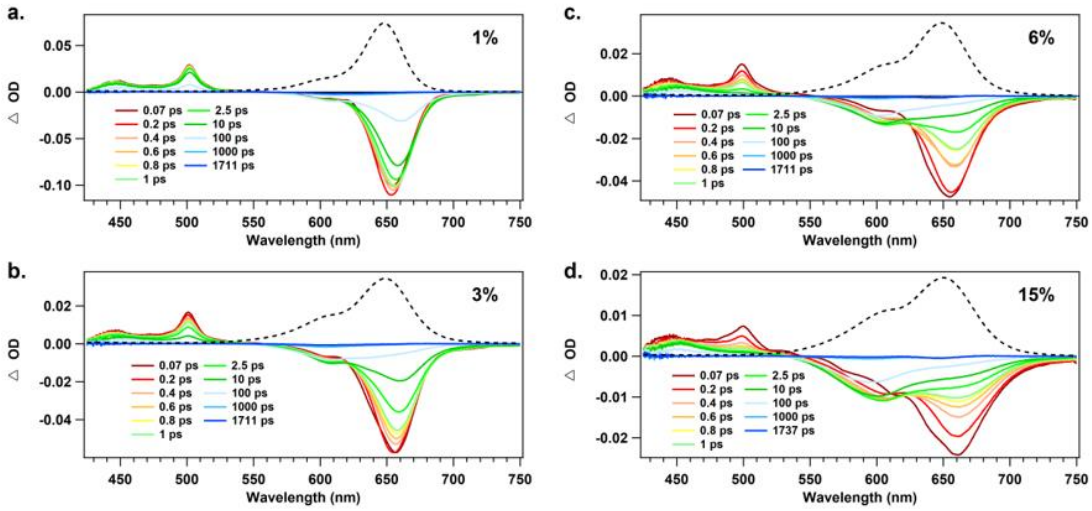

Figure 7.3 Transient absorption spectra of PMMA films with (**a**) 1 wt%, (**b**) 3 wt%, (**c**) 6 wt% and (**d**) 15 wt% of $DBSQ(OH)_2$, after excitation at 640 nm. The steady state absorption spectra are shown as the dashed line in each figure.

The effect of the coupling interaction on excited state dynamics were investigated through transient absorption (TA) and are shown in Figure 7.3. In Chapter 5 we discussed how this Coulombic interaction in the $DBSQ(OH)_2$ CC-aggregate effectively transfers the oscillator strength from the 0-0 vibronic peak to the higher-energy 0-1 peak while simultaneously causing a hypsochromic shift in the transition energies (Figure 5.5). Upon photoexcitation, the TA spectra show an instantaneous negative GSB and positive ESA signals, similar to those in 0.01 wt% PMMA films except that the GSB becomes broader as the concentration increases. As time progresses, the original GSB spectra evolve into new profiles with dominant 0-1 transition peaks and weak 0-0 peaks, prominently illustrated in the 6 wt% and 15 wt% PMMA films. Along with the changing GSB magnitude, the sharp ESA signal at 500 nm diminishes, leaving a single ESA peak at 460

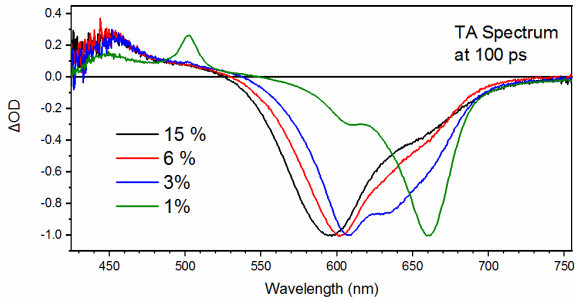

Figure 7.4 Transient absorption spectra of PMMA films of different $DBSQ(OH)_2$ concentrations at 100 ps. The spectra are normalized to the GSB peak. For higher wt% films, the GSB spectra are in great consistency with the simulated spectra in Figure 5.5, exhibiting a higher 0-1 transition peak at 600 nm (more so in higher wt% films). This indicates the preserved excited states after 100 ps are mostly CC-aggregates.

nm, slightly red-shifted from the original ESA peak at 440 nm. Again, these trends are more clearly observed in the concentrated films in Figure 7.4). These changes in both GSB and ESA signals indicate that few monomer excited states are present after 100 ps. The GSB spectra in concentrated (6 wt% and 15 wt%) PMMA films at 100 ps are in great agreement with the simulated absorption spectra using the Essential-state model with Coulombic coupling (Figure 5.5), suggesting that the "new" GSB and ESA signals should belong to the Coulombic-coupled aggregates. For less concentrated films (1 wt% and 3 wt%), the spectral evolution is less clear, but one can still see that the signals at ~600 nm decay at a slower rate when compared to the signals at 650 nm, indicating a small amount of CC-aggregates formed in the dilute films.

The total excited state lifetime (taking into account the longest decay kinetics in the spectrum) is 663 ps, 627 ps, 323 ps and 250 ps for each PMMA films, 1 - 15 wt% respectively. These lifetimes are significantly shorter than that of the monomer in dilute (0.01 wt%) PMMA film, which is 2700 ps. Furthermore, the lifetime measured from the

decay kinetics of monomer ESA at 503 nm for each PMMA films is observed to be even shorter than the total lifetime values indicated above, especially for higher concentration films. In Figure 7.3 c and d, we see an increase in magnitude of the GSB at 605 nm because the monomers can energy transfer to associated CC-aggregates thus depleting their ground state population. Supporting this explanation, an isosbestic point is observed at 625 nm in the early time scale (0-2.5 ps) between the GSB's of the SQ monomers and CC-aggregates. Based on these observations, we assign the early spectral behavior and the fast monomer decay to the energy transfer from monomers to CC-aggregates in PMMA films.

7.3 Excited State Dynamics in PMMA Films

High photovoltaic performance relies on efficient exciton diffusion to the interface, and therefore exciton mobility in organic semiconductors is a critical intrinsic property that will impact the success of a given materials for OPV application. The main excited state diffusion mechanism in bulk heterojunction layers is likely a long-range Förster resonant energy transfer (FRET).[199,200] This energy transfer may be achieved via dipole-dipole interactions between two identical molecules as well as for a heterogeneous donor-acceptor pair. As previously discussed, transfer of excitation energy from monomers to CC-aggregates is inferred from transient absorption spectra for $DBSQ(OH)_2$ PMMA films, and the fast depopulation of the monomer excited state. In this section, we investigate the rate of this energy transfer with respect to the changing SQ wt% in the PMMA films. In addition, this energy transfer may lead to multiple excitations on $DBSQ(OH)_2$ aggregates, which in some circumstances may undergo singlet-singlet annihilation. Such annihilation processes have been investigated for many semiconducting polymers,[187,201–203] as their

study can yield useful information about the exciton diffusion dynamics. Thus, we also test the power dependence of the decay kinetics for the $DBSQ(OH)_2$ PMMA films.

7.3.1 Energy transfer between monomer and aggregate in PMMA films

The energy transfer rate can be extracted from the decay of the monomer ESA at 500 nm, shown in Figure 7.5a and the growth of CC-aggregate GSB at 605 nm, shown in Figure 7.5b. In Figure 7.5a, there is a clear acceleration (from black to red traces) in the loss of the ESA signal at 500 nm as the concentration of $DBSQ(OH)_2$ is increased. For the 1 wt% film, the ESA still exists after 100 ps, while the ESA disappears in less than 2 ps for the 15 wt% film. Consistent with the ESA loss kinetics, the rise (more negative ΔOD) in the 605 GSB signals is observed to be faster in the more concentrated films. For example, the ΔOD in the 605 nm signal is most negative at ~ 80 ps in 1 wt% film while the same ΔOD maximum decrease occurs at ~ 2 ps for the 15 wt% film (Figure 7.5b). Finally, the rate of energy transfer obtained by fitting the kinetic traces are 3.17 ps, 0.56 ps, 1.50 ps and 0.34 ps for 1 wt%, 3 wt%, 6 wt% and 15 wt% films. These energy transfer time constants are much faster than the total excited state lifetimes (see Table 7.1). The faster energy transfer rate in higher concentration PMMA films is attributed to the higher population of $DBSQ(OH)_2$ aggregates, which act as energy acceptors collecting the excitations from the initially excited monomer.

Transient anisotropy decay is a strong indicator for transfer of excitation energies between chromophores. In the rigid PMMA matrix, the SQ molecules are fixed in position. Therefore, the anisotropy can only decay when the excitation on the initially excited molecule is transferred to an adjacent molecule with a different transition dipole moment orientation. The rate constants of anisotropy decay are measured to be 2.95 ps, 0.27 ps,

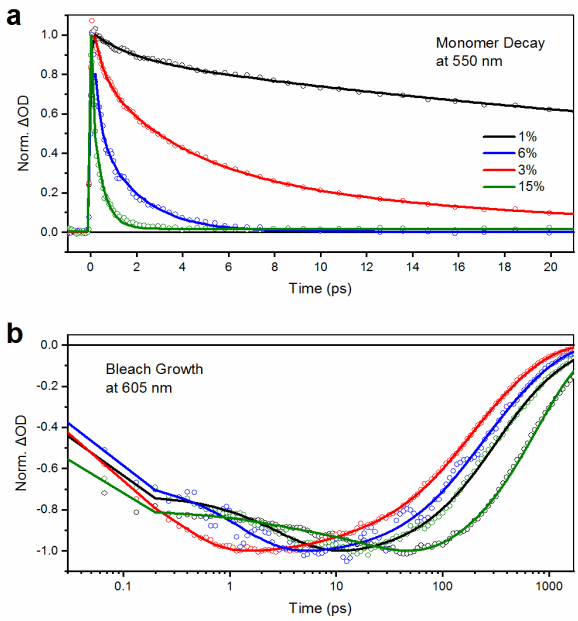

Figure 7.5 Normalized decay profile of ESA signal at (**a**) 500 nm (monomer) and the growth profile of GSB signal at (**b**) 605 nm (CC-aggregate). The GSB signal at 605 nm is plotted logarithmically to illustrate the initial (negative) rise due to the energy transfer from the monomer to CC-aggregate.

0.10 ps and 0.37 ps for the 1 wt%, 3 wt%, 6 wt% and 15 wt% films, respectively, following a general decreasing trend which is in accord with the energy transfer rate constants in those films.

It must be recognized that not only can the loss of anisotropy be attributed to the energy transfer from monomers to aggregates, but it may also originate from homo-FRET transfer between monomers. Indeed, the small Stokes shift of SQ monomer ensures that there is a significant overlapping between absorption and fluorescence spectra. According to Equation (1.10) and (1.11), the FRET radius is calculated to be 7.34 nm for SQ monomers and the corresponding time constants (i.e. the inverse of the rate constant, k_{FRET} in Equation (1.10)) are calculated to be from ~ 100 ps, in the 1 wt% PMMA film, to ~ 0.5 ps,

Table 7.1 The time constants for total excited state lifetime, energy transfer and loss of anisotropy in different PMMA films.

		1% SQ	**3% SQ**	**6% SQ**	**15% SQ**
Total excited state lifetime [a]	τ_1	663 ps	627 ps	323 ps	250 ps
Energy transfer time constant [b]	τ_1	3.17 ps	0.564 ps	1.50 ps	0.344 ps
	τ_2	31.4 ps	4.02 ps	-	-
Anisotropy decay time constant [c]	τ_1	2.95 ps	0.274 ps	0.102 ps	0.366 ps
	τ_2	38.3 ps	2.95 ps	1.20 ps	-

[a] The total excited state lifetime is obtained by fitting the decay kinetics at 620 nm.
[b] The averaged energy transfer rate is obtained by averaging the signal loss at 500 nm (monomer ESA) and signal gain at 600 nm (aggregate GSB).
[c] The anisotropy loss is obtained by fitting the decay kinetics of the TA signal at 660 nm (monomer SE).

in the 15 wt% PMMA film. Clearly, the fast FRET can definitely outcompete the natural decay of the excited state of monomer (i.e. 2700 ps).

In a short summary, the excitation in $DBSQ(OH)_2$ can undergo FRET transfer to other unexcited monomers as well as cascade to the CC-aggregates. Any back energy transfer to the monomers from the CC-aggregates is prevented because the CC-aggregate will not fluorescence, in accordance with theory described in Chapter 5. Hence, at longer times (> 100 ps), there are few excited monomers while most excitations are located on the CC-aggregates, which then decay in several hundreds of picoseconds. Next, we look to investigate the exciton dynamics in $DBSQ(OH)_2$ aggregates in PMMA films.

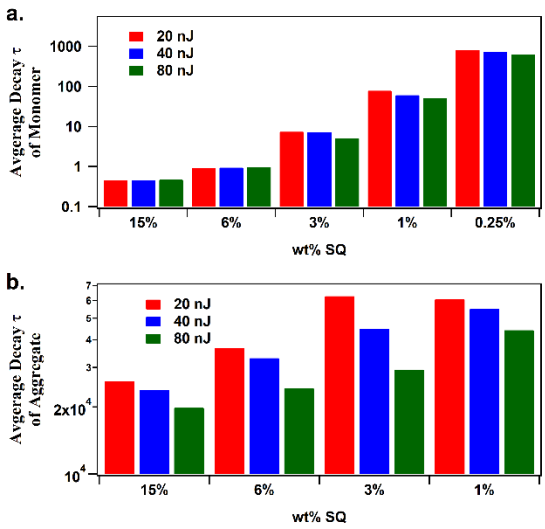

Figure 7.6 The weighted average decay rate constants for TA signals at (**a**) 500 nm (monomer ESA) and (**b**) at 600 nm (CC-aggregate GSB). The decay kinetics are weighted by the TA signal amplitudes to minimize the influence of overlapping spectra from monomers and aggregates.

7.3.2 Singlet-singlet annihilation in PMMA films

Singlet-singlet (S-S) annihilation occurs when two excitons interact with each other at short distances (typically within one polymer chain or between closely stacked molecules or aggregates). Under a high-power excitation pump, the excitons may exist in high densities (especially for molecules with high extinction coefficient) such that inter-exciton distance is within the exciton diffusion length. Thus, S-S annihilation is often observed for many conjugated polymers and molecular aggregates where the generated excitons are highly mobile.[203–206] Here, the decay kinetics associated principally with the monomer as well as with the CC-aggregates were studied for different excitation powers: 20, 40 and 80 nJ/pulse. The decay rate constants for monomers and aggregates were obtained by fitting the decay curves at 500 nm (monomer ESA) and 600 nm (CC-aggregate GSB).

For decay kinetics of the monomer ESA at 500 nm (Figure 7.6a), there is a noticeable

decrease in time constant for higher photon flux (except for 6 wt% and 15 wt% PMMA films) indicating S-S annihilation occurs for monomers in PMMA films. The lack of power dependence in high SQ wt% PMMA films is attributed to the fast energy transfer rate, with time constants of 0.3-1.5 ps, which must outcompete the S-S annihilation process. For PMMA films with low SQ wt%, energy transfer is less likely to occur on a fast time scale (see Table 7.1) as there are fewer aggregates formed. Thus, in those films, S-S annihilation should be the main relaxation mechanism for the monomer excited state and is largely responsible for the short total excited state lifetime (*e.g.* 663 ps for 1 wt% PMMA film) as compared to the 2700 ps decay time of monomer excited state in the least concentrated 0.01 wt% PMMA film. Overall, the SQ monomer excited states quickly depopulate via both energy transfer and S-S annihilation processes, where the former (later) process dominates in higher (lower) concentration PMMA films.

The long-time decays of the GSB signals at 600 nm (corresponding to the aggregate GSB given that monomer is depleted at early times) exhibit a substantial power dependence for all PMMA films as shown in Figure 7.6b. We note that the transfer of excitations from monomer to aggregate has essentially been completed at long time scales. Thus, the observed power dependence indicates that the excitons in the aggregates (formed either by initial excitation or by energy transfer) are highly mobile such that the higher densities of excitons lead to a faster S-S annihilation rate.

The S-S annihilation studies suggest that the excitons formed in both monomers and aggregates of $DBSQ(OH)_2$ are highly mobile. This is beneficial for the exciton diffusion step as the excitons formed in the center of the pure phases can efficiently diffuse to the heterojunction interface and subsequently undergo dissociation. Unfortunately, the exact

S-S annihilation rate for monomers and aggregates cannot be obtained without knowing the initial exciton density in the PMMA films after excitation. This is currently under investigation through our collaboration with Mark and McCamant at University of Rochester.

7.4 Discussion

In this chapter, we have investigated the excited state dynamics of fully solvated $DBSQ(OH)_2$ in chloroform solution, as well as the SQ monomers and CC-aggregates formed in PMMA solid solution films to gain insight on the energy transfer processes and exciton movements in the organic photovoltaic devices.

The monomers in solution exhibit a long excited state lifetime of 2.7 ns which is consistent with reported values of similar SQ molecules in the literature.[198,207] Two ESA peaks are observed at 440 nm and 503 nm, representing $S_1 \rightarrow S_n$ transitions. When $DBSQ(OH)_2$ molecules are dispersed in a rigid PMMA matrix with large intermolecular distances (e.g. 0.01 wt%, $DBSQ(OH)_2$) the SQ molecules exhibit similar photophysical properties as for fully solvated monomers in solution. The intermolecular interaction is negligible; the absorption spectra and the excited state lifetime are wholly consistent with the solution measurements.

The advantages of the PMMA solid solution approach lie in the ability to control the intermolecular distance by changing the SQ weight percent. As calculated in Table 5.2, the molecular separation distance can be tuned from 20 nm in 0.01 wt% film to 1.7 nm in 15 wt% film. At decreasing intermolecular distances, the molecules experience intermolecular interactions of increasing strengths, resulting in different photophysical properties.

For 0.25 wt% PMMA films, the absorption spectrum suggests that there are still few aggregates that have formed. Yet, the excited state lifetime is measured to be significantly shorter than the 0.01 wt% film (i.e. 750 ps vs. 2700 ps). Such differences, based on transient polarization anisotropy decay kinetics, are attributed to the singlet-singlet annihilation process. This annihilation might occur through Förster-type dipole-dipole interactions.[204]

In higher concentration (1-15 wt%) PMMA films, $DBSQ(OH)_2$ molecules exist in both monomer and CC-aggregate forms. Energy transfer from monomer to aggregate is observed in transient absorption spectra at increasing delay times. At longer times (> 100 ps), the negative GSB signals at 600-700 nm feature a higher 0-1 vibronic peak, in excellent agreement with the previous simulated CC-aggregate spectra. This consistency validates the previous Essential-state model approach. For 6 wt% and 15 wt% PMMA films, an isosbestic point was observed (Figure 7.3), evidencing the energy transfer process. The energy transfer rate constant (obtained from the kinetic traces of monomer ESA at 500 nm and CC-aggregate GSB at 600 nm) is measured to be 0.3-3 ps, significantly faster than any other photophysical processes.

At a long-time scale, the excitation energies originating in the monomer excited states have completely been transferred to the CC-aggregates (given that the energy transfer rate outcompetes other photophysical processes). The decay of the CC-aggregate excited state (GSB signals at 600 nm) was also found to be power dependent, indicating that the excitations undergo S-S annihilation in the CC-aggregates as well. Overall, we found that the excitations are mobile in both SQ monomers and CC-aggregates (due to the observations of S-S annihilation in both species), and when the population of CC-aggregates is large, the energy transfer from monomer to aggregate is faster than the S-S

annihilation rate in monomers.

The highly mobile excitations and the energy transfer from monomers to CC-aggregates are considered beneficial for the exciton diffusion step in OPVs. Since the absorption spectra of the 15 wt% PMMA films (Figure 5.4) are similar to those of $DBSQ(OH)_2$:PCBM bulk heterojunction films (Figure 5.3), we argue that there is a similar monomer and CC-aggregates population; the 15 wt% PMMA is a good analogue for $DBSQ(OH)_2$ in a working device. Thus, we think the photophysical processes in the BHJ films are similar to those in the PMMA films, except that charge dissociation can of course occur at the donor-acceptor interface. Highly mobile excitations in SQ phases (both monomer and CC-aggregates) will enable an efficient exciton diffusion to the SQ-PCBM interface and subsequently an efficient charge dissociation. This may explain the high efficiency achieved with the amorphous, as-cast devices, where previously we thought the exciton diffusion may have been substantially hindered by the disordered and amorphous domains.

Upon annealing the BHJ films, SQ monomers and CC-aggregates transform into ICT-aggregates with a double-hump absorption profile (see Figure 4.4b). We note that the annealed devices yield a lower external quantum efficiency and a decreased PCE. Here, we think the TA experiments for annealed SQ neat films might give some insight to the photophysics of the ICT-aggregates that could explain the inferior performance of such aggregates in OPVs. This is highlighted as a future direction that is beyond the scope of this dissertation.

Chapter 8. SUMMARY AND CONCLUSIONS

In this dissertation, we have investigated the effect of squaraine aggregation on organic photovoltaic device efficiencies, with development of a deeper understanding of the intermolecular interactions and excited state structures and dynamics of the squaraine aggregates. The aim has been to provide guidance for developing future squaraine chromophores with desirable aggregation properties for efficient organic photovoltaics. For this purpose, both experimental and theoretical results have been provided in this dissertation.

In the experiments, the solar cell devices have been fabricated to study the effect of donor-acceptor blend ratio, post-annealing treatment, and squaraine molecular structures. In Chapter 3, the parent squaraine molecule $DHSQ(OH)_2$, was tested for its potential in OPV devices. In Section 3.2, comprehensive absorption studies have been carried out and we have recognized a mixed SQ monomer and aggregate population in the bulk heterojunction films when blended with PCBM. In particular, the $DHSQ(OH)_2$ monomer in a "solid solution" of PCBM exhibits an absorption peak at 678 nm, slightly red shifted from the monomer peak at 650 nm in chloroform solution. On the other hand, the $DHSQ(OH)_2$ aggregate showed two-peak absorption at 550 nm and 660 nm, resulting in a significantly broadened absorption spectrum as compared to the monomer. The overlapping absorption of the monomer and aggregates at 660-680 nm poses some difficulties when considering the relative populations of these two species. However, qualitative estimation the relative population can nevertheless be drawn based on the ratio of the two peaks of the aggregate (Figure 3.3). Our work thus clarifies the debate within the literature[59,126,131,132,146,149] over the nature and relative population of aggregates formed

in SQ:PCBM systems. For neat films, $DHSQ(OH)_2$ demonstrates a fast aggregation upon spin casting with little monomer population present in the films. The presence of PCBM induces a disruption of $DHSQ(OH)_2$ aggregation, leading to an increasing population of SQ monomers as the PCBM weight ratio is increased. Thus, the donor-acceptor blend ratio strongly impacts the relative monomer-aggregation population in the OPV devices. When thermally annealed, the movement of molecules in the bulk heterojunction has been activated, leading to SQ aggregation (Figure 3.3) and phase separation.

In Section 3.3, through thin film XRD studies, we further confirmed that the $DHSQ(OH)_2$ aggregates are crystalline while monomers are amorphous. This suggests that the exciton diffusion and charge transport *might* be more efficient in the aggregated domains. The crystallinity of the film was shown to depend on the relative populations, which can be altered by the blend ratio. The phase-separated domain sizes have been characterized by TEM. We have found that thermal annealing can induce extensive phase separation between $DHSQ(OH)_2$ and PCBM, leading to a formation of domains that are as large as 100-200 nm, more than 10 times larger than the measured exciton diffusion length of a similar squaraine.[121] Our analysis of annealed films demonstrates a delicate trade-off between increased crystallinity and larger domain sizes.

Organic solar cell efficiencies can be well correlated with the BHJ morphology and the $DHSQ(OH)_2$ aggregation. The optimized efficiency was achieved by first blending SQ with high fullerene content to disrupt the aggregation and thus to reach a finely mixed morphology, and then thermally annealing the BHJ films to activate SQ aggregation while preventing extensive phase separation. In order to find the "sweet spot" for annealing temperature, thermal behavior of the BHJ was characterized and we discovered a phase-

separation onset temperature of 137 ^{0}C for DHSQ(OH)$_2$:PCBM blends. Thus, a guideline for device optimization for small squaraine molecular donor and fullerene acceptor BHJ solar cells has been provided.

Then, the solar cell fabrication is improved by patterning ITO substrates, use of a better absorbing $PC_{71}BM$ acceptor and by replacing acidic PEDOT:PSS with MoO_3 as the transport layer. The efficiencies of the devices were significantly improved.

In Chapter 4, a series of SQ molecules with changing alkyl side groups were investigated for OPV applications. These molecules have very similar photophysical properties in solution as well as in neat films, as expected for their shared conjugation backbones and similar crystal structure (adopting a slip-stack packing geometry). However, when they were blended with fullerenes, significant differences in aggregation, film crystallinity and BHJ morphology became apparent. The absorption spectra of SQ:PCBM blend films demonstrated the disruption of aggregation in the presence of fullerene. For DHSQ(OH)$_2$, less disruption was observed than for DPSQ(OH)$_2$ and DBSQ(OH)$_2$. Such differences in aggregation disruption correlate with changes in film crystallinity and BHJ morphology, both of which drive the efficiency of OPV devices.

In XRD studies in Section 4.4, we found that the neat films are crystalline with a diffraction peak corresponding to the crystal (001) plane. The extent of crystallinity of the blend films were found to be in the order of DBSQ(OH)$_2$ > DPSQ(OH)$_2$ > DHSQ(OH)$_2$, corresponding well with the aggregate population in the films, observed through absorption spectroscopy. The hole mobilities of SQ neat films were measured to be on the order of 10^{-4} ~ 10^{-5} cm^2/V·s, with DBSQ(OH)$_2$ taking a higher value. Nevertheless, the mobility dropped when SQ aggregation (and crystal packing) was disrupted in blends. In particular,

the mobility dropped by over 10-folds for $DBSQ(OH)_2$:PCBM blends, while the SQ with longer side chains were able to retain a higher mobility in blend films. As a result, the hole carrier mobilities of SQ:PCBM blend films were in the order $DHSQ(OH)_2$ > $DPSQ(OH)_2$ > $DBSQ(OH)_2$, the exact reversed order when compared to that in neat films. This trend was observed due to the higher crystallinity associated with the $DHSQ(OH)_2$:PCBM blends when the aggregation of $DHSQ(OH)_2$, through decreased SQ-Fullerene chemical compatibility, was less disrupted by the fullerene.

Charge mobility is a critical factor for the solar cell efficiency. Previous studies[70,208,209] have suggested a required threshold mobility of electrons and holes on the order of 10^{-4} $cm^2/V{\cdot}s$ for efficient OPV devices with high fill factor. While high electron mobility in fullerenes has been reported by many groups, on the order of $10^{-3} \sim 10^{-4}$ $cm^2/V{\cdot}s$,[57,210,211] the hole mobility in the donor phase is often measured to be the lower limit of the bipolar charge transport in small molecule donor-fullerene bulk heterojunction solar cells.[36,70,97,165] Thus, based on the mobility results, $DHSQ(OH)_2$ was expected to be a better performing donor materials for OPV devices.

However, the OPV efficiencies from these three SQ molecules contradicted the mobility results. $DBSQ(OH)_2$ yielded the best OPV efficiency of 5.6% even though its mobility dropped by almost 10-fold upon blending with fullerene, with that hole mobility being the lowest among the three SQ molecules studied. This could only be explained by the BHJ morphology. For longer side chain SQs, the phase separation must have occured during the spin casting (even without thermal annealing, see Chapter 3). The extensive phase separation reduced the interfacial area between donor and acceptor, limiting the exciton diffusion and charge dissociation efficiency. $DBSQ(OH)_2$, on the other hand,

mixed well with fullerene and the finely mixed, amorphous blends can efficiently convert excitons to free charges.

These results culminated in an ongoing strategy to inhibit phase separation between SQs and fullerenes. One might think that the SQ-fullerene mixing can be further improved by continually reducing the length of the alkyl side groups. Nevertheless, we found that the SQ with propyl alkyl groups (i.e. DPrSQ(OH)$_2$) was quite insoluble in conventional organic solvents. The quality of spin cast films was significantly affected by the solubility, resulting in a lower efficiency as compared to DBSQ(OH)$_2$.

Wei *et al*. have studied OPV devices employing DiBSQ(OH)$_2$,[40,41,121] a similar squaraine. When comparing the iso-butyl to the linear butyl groups (in DBSQ(OH)$_2$), the optimized solar cell devices exhibited similar efficiency, ~ 5%. Different from DBSQ(OH)$_2$, thermal or solvent annealing was a necessary step to achieve such solar cell performances for DiBSQ(OH)$_2$, and the unannealed BHJ devices only yielded ~ 2% with a significantly lower Jsc.[41] For our DBSQ(OH)$_2$-based devices, the optimized efficiency was achieved without any additional post-treatment step. Furthermore, we obtained an immediate decrease in device efficiency when our devices were mildly annealed (Table 4.5). This different response of device performance to annealing treatment is attributed to the different aggregation propensities of these two SQs. There would be more steric hindrance induced by the bulkier isobutyl chains to hinder the aggregation of DiBSQ(OH)$_2$. We found that our DBSQ(OH)$_2$:PC$_{71}$BM BHJ films showed a more dramatic change in absorption spectra upon annealing due to the SQ aggregation than that of DiBSQ(OH)$_2$:PC$_{71}$BM films. Nevertheless, the marked differences between these two very similar squaraine molecules is interesting and is worth further investigation.

In the second half of this dissertation (Chapter 5 and 6), we performed a theoretical investigation on $DBSQ(OH)_2$ aggregates that are relevant to OPV. Specifically, we identified two types of aggregates in as-cast and annealed BHJ films, each associated with different absorption spectra. The absorption spectrum of the first type of aggregate was described as a broader monomer spectrum with a higher 0-1 vibronic transition peak. The second type of aggregates has a unique "double-hump" absorption spectra, which is often mentioned in this dissertation. The difference in optical spectra was shown to originate from the changes in the electronic state configurations of the aggregates. Therefore, even for the simple SQ:PCBM binary system, there will exist multiple types of donor acceptor interface. The exciton dissociation is largely controlled by the energetics at the interface, as therefore would the OPV efficiency.

Here, we constructed a theoretical model to extract the information about the excited state structures of different types of aggregates. For theoretical work in Chapter 5 and 6, an essential-state model has been developed with a full consideration of both Coulombic coupling (CC) as well as intermolecular charge transfer (ICT) coupling. The essential-state model, has recently been intensely studied and expanded by Painelli *et al.*[107–114,184,212] It uses a minimum number of diabatic states to represent the charge resonant structures of the multipolar chromophore. Low-energy physical descriptions (*i.e.* absorption, fluorescence, *etc*.) can be obtained by transforming the diabatic states into adiabatic vertical states via Hamiltonian diagonalization. The ESM realized an accurate description of symmetry breaking, solvatochromism effects and other puzzling problems associated with these multipolar molecules (including squaraines[107,108]) that were previously difficult to obtain via the widely used exciton model.

Beyond Painelli's work, our model focused on the intermolecular interactions in the SQ aggregates. The model has not only accounted for the Coulombic interactions in the aggregates, but also recognized the contribution from the intermolecular charge transfer (ICT) states. In particular, we found that the Coulombic coupling dominates the intermolecular interactions in the first type of aggregate (hence this is referred to the CC-aggregate). In the second type of aggregate (*i.e.* the ICT-aggregate), additional charge-separated diabatic states have been incorporated due to the intermolecular charge transfer from the donor moiety (i.e. nitrogen atom) of one molecule to the acceptor moiety (i.e. squarylium) of the neighboring molecule.

Chapter 5 focused on constructing the ESM for the $DBSQ(OH)_2$ CC-aggregate. In SQ:PCBM blend films, the non-negligible interactions between SQ and PCBM can induce a shift in absorption spectra (as illustrated in Figure 3.3). Thus, in order to selectively investigate SQ-SQ interactions, we blended an inert polymethylmethacrylate (PMMA) polymer, instead of PCBM, with SQ to control its aggregation. By changing the SQ weight percent with respect to PMMA, we controlled the average inter-squaraine distance, which dictates the coupling strength in the aggregate. The absorption spectra of SQ in PMMA solid solution films demonstrated a gradual change from monomer-like spectra to CC-aggregate spectra similar to those in the SQ:PCBM blends (Figure 5.4).

The Hamiltonian of the CC-aggregate was constructed based on squaraine monomers. A trio of diabatic states describes the neutral and zwitterionic charge resonant structures for a single molecule. The Coulombic interactions were calculated by the point charges residing on the nitrogen atoms or the central squarylium rings between zwitterionic molecules in the aggregates. By assuming a similar aggregate geometry as the single crystal

structure, with enlarged intermolecular distances (as would be expected in such PMMA films), the absorption spectra of $DBSQ(OH)_2$ in PMMA films can be well reproduced with the model with all simulation parameters taken from the monomer, and from the literature.[107,108] The calculations of fluorescence spectra indicated that these CC-aggregates are analogous to the H-aggregates of the exciton model. The vibronic progression in the calculated spectra also exhibited an oscillator strength gain (loss) in the 0-1 (0-0) vibronic peak. This redistribution of vibronic peak intensities was also seen in the H-aggregate modeled using the exciton model. It is also consistent with the experimental observation of the increasing 0-1 vibronic shoulder in the absorption spectra of PMMA films with increasing SQ weight percent.

The Coulombic ESM reproduced the PMMA-film absorption spectra very well. Yet, it failed to do so for the neat or annealed blended films (Figure 5.7). This is because the intermolecular charge transfer occurs in the closely packed SQ ICT-aggregates which mostly exist in neat or annealed blended films. Four ionic diabatic states, in addition to the original three charge neutral diabatic states, needed to be considered when the ICT is enabled, which necessitated two additional simulation parameters, η_{CT} and t_{CT}. These two adjustable parameters were set to best reproduce the absorption spectra. By using the new and complete Hamiltonian in Equation (6.1) for ICT-aggregates, we achieved an excellent consistency between simulated and experimental spectra, as shown in Figure 6.3.

The origin of the "double-hump" absorption lineshape is well understood through this new model. Each of the two broad absorption peaks consisted of several sub vibronic peaks as shown in Figure 6.3. By taking out the vibrational and vibronic Hamiltonians, we found two electronic states that are "bright" to the ground state. These two states were

qualitatively understood to be the product of the coupling between $|gc\rangle^{AS}$ and $|ac_1\rangle^{AS}$ states. Of note, the $|gc\rangle^{AS}$ state is the original optically allowed Frenkel state in the CC-aggregate. The $|ac_1\rangle^{AS}$ state, on the other hand, is a "dark" state that cannot be populated by the transition from the ground state. The coupling (with a matrix element of $\tau = 2t_{CT}t_Z/\sqrt{\eta_Z^2 + 8t_Z^2}$) between the Frenkel state and the dark $|ac_1\rangle^{AS}$ state resulted in two new states that both contain the $|gc\rangle^{AS}$ state components. Hence, both new states are optically allowed.

Finally, in Chapter 7, the excited state dynamics of $DBSQ(OH)_2$ in chloroform solution and in PMMA solid solutions were investigated using femtosecond transient absorption spectroscopy. The monomer in extremely dilute PMMA films showed the same excited decay dynamics as that in fully solvated monomers in chloroform solution. Two excited state absorption peaks were found at 440 nm and 503 nm. The excited state absorption, ground state bleach and stimulated emission signals decayed with the same time constant, indicating that only monomer excited states are populated upon photoexcitation. As soon as the concentration of SQs was increased, the excited state lifetime was measured to be significantly shorter than the 0.01 wt%. The fast decay of the monomer excited state lifetime was attributed to the transfer of excitation from monomer to CC-aggregate formed in those PMMA films, as well as to a singlet-singlet annihilation process. At a longer time scale, the transient absorption spectra evolved from that of the monomer to the CC-aggregate, with an excited state absorption peak at 460 nm and a ground state bleach at 600-700 nm featuring a higher 0-1 vibronic peak, in excellent agreement with the previously simulated CC-aggregate spectra (Figure 5.5).

Singlet-singlet annihilation is observed in both monomer and CC-aggregate,

indicating that the excitons formed in those systems are highly mobile. The mobile excitations and the energy transfer from monomer to CC-aggregate are considered beneficial for the exciton diffusion step in OPVs. This explained the high efficiency achieved with as-cast amorphous $DBSQ(OH)_2$:$PC_{71}BM$ bulk heterojunctions.

Both theoretical and experimental works in this dissertation have led to some promising future directions. In the theory part, we have identified two types of intermolecular interactions: Coulomb coupling (CC) and intermolecular charge transfer (ICT) coupling. We have also developed a deep understanding of the impact of ICT states on excited state structures of SQ aggregates. Yet, the effect of ICT coupling on the excited state dynamics is unclear. Nicholas Hestand *et al*.[29] have theoretically shown that the exciton mobility can be dramatically altered by the interference between Coulombic coupling and intermolecular charge transfer coupling in the molecular aggregates. Specifically, when these two intermolecular interactions constructively (destructively) interfere, the exciton movement is significantly enhanced (hindered). Here, in order to explore the impact of ICT on exciton mobility in SQ aggregates, one method is to link the essential-state model to the exciton model (which was used for exciton transfer efficiency calculations in the literature[29]).

In addition, the ESM contains three diabatic electronic states and N^2 vibronic states (where N-1 is the maximum vibrational quanta on each molecular arm). Thus, the basis set becomes large when considering aggregates. Due to computational restraints, any aggregate with a size larger than a trimer cannot be effectively modeled with acceptable computational time. A vibronic exciton model has advantages in this regard since the modeled chromophore consists of just two electronic levels with the ground and excited

state nuclear potentials represented by shifted harmonic wells. Thus, by linking the ESM to the exciton model, we can potentially increase the aggregate size.

To accomplish this, the critical first step is to link the ESM parameters to the parameters in the exciton model. Since the ESM is constructed based on diabatic states, the parameters are effectively diabatic in nature, which is different from the adiabatic parameters in the exciton model. Thus, these parameters need to be "translated" to the effective parameters in the exciton model.

For the transient absorption experiment, the excited state dynamics in SQ ICT-aggregates is of particular interest as a comparison with the dynamics of the CC-aggregates. In the solar cell devices, we observed that the power conversion efficiency of the devices immediately decreased when $DBSQ(OH)_2$ formed ICT-aggregates. This decrease in efficiency cannot be fully explained without knowing the exciton dynamics in these ICT-aggregates. Thus, a transient absorption investigation of the $DBSQ(OH)_2$ ICT-aggregates in annealed neat films might provide additional insight of the inferior performance of such aggregates in OPV devices.

REFERENCE

(1) Two-layer Organic Photovoltaic Cell. *Appl. Phys. Lett.* **1986**, *48* (2), 183–185.

(2) Sariciftci, N. S.; Smilowitz, L.; Heeger, A. J.; Wudl, F. Photoinduced Electron Transfer from a Conducting Polymer to Buckminsterfullerene. *Science* **1992**, *258* (5087), 1474–1476.

(3) Kraabel, B.; Lee, C. H.; McBranch, D.; Moses, D.; Sariciftci, N. S.; Heeger, A. J. Ultrafast Photoinduced Electron Transfer in Conducting Polymer—Buckminsterfullerene Composites. *Chem. Phys. Lett.* **1993**, *213* (3), 389–394.

(4) Krebs, F. C. Fabrication and Processing of Polymer Solar Cells: A Review of Printing and Coating Techniques. *Sol. Energy Mater. Sol. Cells* **2009**, *93* (4), 394–412.

(5) Krebs Frederik C.; Espinosa Nieves; Hösel Markus; Søndergaard Roar R.; Jørgensen Mikkel. 25th Anniversary Article: Rise to Power – OPV-Based Solar Parks. *Adv. Mater.* **2013**, *26* (1), 29–39.

(6) A. dos Reis Benatto Gisele; Espinosa Nieves; Krebs Frederik C. Life-Cycle Assessment of Solar Charger with Integrated Organic Photovoltaics. *Adv. Eng. Mater.* **2017**, *19* (8), 1700124.

(7) Landerer Dominik; Bahro Daniel; Röhm Holger; Koppitz Manuel; Mertens Adrian; Manger Felix; Denk Fabian; Heidinger Michael; Windmann Thomas; Colsmann Alexander. Solar Glasses: A Case Study on Semitransparent Organic Solar Cells for Self-Powered, Smart, Wearable Devices. *Energy Technol.* **2017**, *5* (11), 1936–1945.

(8) Lunt, R. R.; Bulovic, V. Transparent, near-Infrared Organic Photovoltaic Solar Cells for Window and Energy-Scavenging Applications. *Appl. Phys. Lett.* **2011**, *98* (11), 113305.

(9) Cutting, C. L.; Bag, M.; Venkataraman, D. Indoor Light Recycling: A New Home for Organic Photovoltaics. *J. Mater. Chem. C* **2016**, *4* (43), 10367–10370.

(10) Park, S. H.; Roy, A.; Beaupre, S.; Cho, S.; Coates, N.; Moon, J. S.; Moses, D.; Leclerc, M.; Lee, K.; Heeger, A. J. Bulk Heterojunction Solar Cells with Internal Quantum Efficiency Approaching 100%. *Nat Photon* **2009**, *3* (5), 297–302.

(11) Sun, Y.; Welch, G. C.; Leong, W. L.; Takacs, C. J.; Bazan, G. C.; Heeger, A. J. Solution-Processed Small-Molecule Solar Cells with 6.7% Efficiency. *Nat. Mater.* **2012**, *11* (1), 44–48.

(12) Long, Y.; Wenchao, Z.; Sunsun, L.; Subhrangsu, M.; H, C. J.; Omar, A.; Xuechen, J.; Jianhui, H.; Harald, A. High-Efficiency Nonfullerene Organic Solar Cells: Critical Factors That Affect Complex Multi-Length Scale Morphology and Device Performance. *Adv. Energy Mater. 7* (7), 1602000.

(13) Li, G.; Yao, Y.; Yang, H.; Shrotriya, V.; Yang, G.; Yang, Y. "Solvent Annealing" Effect in Polymer Solar Cells Based on Poly(3-Hexylthiophene) and Methanofullerenes. *Adv. Funct. Mater.* **2007**, *17* (10), 1636–1644.

(14) Salim, T.; Wong, L. H.; Bräuer, B.; Kukreja, R.; Foo, Y. L.; Bao, Z.; Lam, Y. M. Solvent Additives and Their Effects on Blend Morphologies of Bulk Heterojunctions. *J. Mater. Chem.* **2010**, *21* (1), 242–250.

(15) Love, J. A.; Nagao, I.; Huang, Y.; Kuik, M.; Gupta, V.; Takacs, C. J.; Coughlin, J. E.; Qi, L.; van der Poll, T. S.; Kramer, E. J.; et al. Silaindacenodithiophene-Based Molecular Donor: Morphological Features and Use in the Fabrication of Compositionally Tolerant, High-Efficiency Bulk Heterojunction Solar Cells. *J. Am. Chem. Soc.* **2014**, *136* (9), 3597–3606.

(16) Ameri, T.; Li, N.; J. Brabec, C. Highly Efficient Organic Tandem Solar Cells: A Follow up Review. *Energy Environ. Sci.* **2013**, *6* (8), 2390–2413.

(17) Kawano, K.; Pacios, R.; Poplavskyy, D.; Nelson, J.; Bradley, D. D. C.; Durrant, J. R. Degradation of Organic Solar Cells Due to Air Exposure. *Sol. Energy Mater. Sol. Cells* **2006**, *90* (20), 3520–3530.

(18) Penmetcha, A. R.; Zheng, C.; Collison, C. J. Water Based Inkjet Material Deposition of Donor-Acceptor Nanocomposites for Usage in Organic Photovoltaics. *MRS Online Proc. Libr. Arch.* **2015**, *1761*.

(19) Rand, B. P.; Burk, D. P.; Forrest, S. R. Offset Energies at Organic Semiconductor Heterojunctions and Their Influence on the Open-Circuit Voltage of Thin-Film Solar Cells. *Phys. Rev. B* **2007**, *75* (11), 115327.

(20) Forrest, S. R. The Limits to Organic Photovoltaic Cell Efficiency. *MRS Bull.* **2005**, *30* (1), 28–32.

(21) Godovsky, D. Modeling the Ultimate Efficiency of Polymer Solar Cell Using Marcus Theory of Electron Transfer. *Org. Electron.* **2011**, *12* (1), 190–194.

(22) V. Mikhnenko, O.; M. Blom, P. W.; Nguyen, T.-Q. Exciton Diffusion in Organic Semiconductors. *Energy Environ. Sci.* **2015**, *8* (7), 1867–1888.

(23) A. Lin, J. D.; V. Mikhnenko, O.; Chen, J.; Masri, Z.; Ruseckas, A.; Mikhailovsky, A.; P. Raab, R.; Liu, J.; M. Blom, P. W.; Antonietta Loi, M.; et al. Systematic

Study of Exciton Diffusion Length in Organic Semiconductors by Six Experimental Methods. *Mater. Horiz.* **2014**, *1* (2), 280–285.

(24) Lunt, R. R.; Giebink, N. C.; Belak, A. A.; Benziger, J. B.; Forrest, S. R. Exciton Diffusion Lengths of Organic Semiconductor Thin Films Measured by Spectrally Resolved Photoluminescence Quenching. *J. Appl. Phys.* **2009**, *105* (5), 053711.

(25) Shaw, P. E.; Ruseckas, A.; Samuel, I. D. W. Exciton Diffusion Measurements in Poly(3-Hexylthiophene). *Adv. Mater.* **2008**, *20* (18), 3516–3520.

(26) Lunt, R. R.; Benziger, J. B.; Forrest, S. R. Relationship between Crystalline Order and Exciton Diffusion Length in Molecular Organic Semiconductors. *Adv. Mater.* **2010**, *22* (11), 1233–1236.

(27) Rim, S.-B.; Fink, R. F.; Schöneboom, J. C.; Erk, P.; Peumans, P. Effect of Molecular Packing on the Exciton Diffusion Length in Organic Solar Cells. *Appl. Phys. Lett.* **2007**, *91* (17), 173504.

(28) A. Siebbeles, L. D.; Huijser, A.; J. Savenije, T. Effects of Molecular Organization on Exciton Diffusion in Thin Films of Bioinspired Light-Harvesting Molecules. *J. Mater. Chem.* **2009**, *19* (34), 6067–6072.

(29) Hestand, N. J.; Tempelaar, R.; Knoester, J.; Jansen, T. L. C.; Spano, F. C. Exciton Mobility Control through Sub-Å Packing Modifications in Molecular Crystals. *Phys. Rev. B* **2015**, *91* (19), 195315.

(30) Menke, S. M.; Luhman, W. A.; Holmes, R. J. Tailored Exciton Diffusion in Organic Photovoltaic Cells for Enhanced Power Conversion Efficiency. *Nat. Mater.* **2013**, *12* (2), 152–157.

(31) Coffey, D. C.; Larson, B. W.; Hains, A. W.; Whitaker, J. B.; Kopidakis, N.; Boltalina, O. V.; Strauss, S. H.; Rumbles, G. An Optimal Driving Force for Converting Excitons into Free Carriers in Excitonic Solar Cells. *J. Phys. Chem. C* **2012**, *116* (16), 8916–8923.

(32) Cowan, S. R.; Roy, A.; Heeger, A. J. Recombination in Polymer-Fullerene Bulk Heterojunction Solar Cells. *Phys. Rev. B* **2010**, *82* (24), 245207.

(33) Street, R. A.; Cowan, S.; Heeger, A. J. Experimental Test for Geminate Recombination Applied to Organic Solar Cells. *Phys. Rev. B* **2010**, *82* (12), 121301.

(34) Credgington, D.; Jamieson, F. C.; Walker, B.; Nguyen, T.-Q.; Durrant, J. R. Quantification of Geminate and Non-Geminate Recombination Losses within a Solution-Processed Small-Molecule Bulk Heterojunction Solar Cell. *Adv. Mater.* **2012**, *24* (16), 2135–2141.

(35) Alexander, F.; Juliane, K.; Markus, G.; Thomas, B.; Vladimir, D.; Dieter, N.; Carsten, D. Nongeminate and Geminate Recombination in PTB7:PCBM Solar Cells. *Adv. Funct. Mater. 24* (9), 1306–1311.

(36) Proctor, C. M.; Kim, C.; Neher, D.; Nguyen, T.-Q. Nongeminate Recombination and Charge Transport Limitations in Diketopyrrolopyrrole-Based Solution-Processed Small Molecule Solar Cells. *Adv. Funct. Mater.* **2013**, *23* (28), 3584–3594.

(37) Proctor, C. M.; Albrecht, S.; Kuik, M.; Neher, D.; Nguyen, T.-Q. Overcoming Geminate Recombination and Enhancing Extraction in Solution-Processed Small Molecule Solar Cells. *Adv. Energy Mater.* **2014**, *4* (10), 1400230.

(38) Park, Y.; Choong, V.; Gao, Y.; Hsieh, B. R.; Tang, C. W. Work Function of Indium Tin Oxide Transparent Conductor Measured by Photoelectron Spectroscopy. *Appl. Phys. Lett.* **1996**, *68* (19), 2699–2701.

(39) Song, Q. L.; Li, F. Y.; Yang, H.; Wu, H. R.; Wang, X. Z.; Zhou, W.; Zhao, J. M.; Ding, X. M.; Huang, C. H.; Hou, X. Y. Small-Molecule Organic Solar Cells with Improved Stability. *Chem. Phys. Lett.* **2005**, *416* (1–3), 42–46.

(40) Wei, G.; Wang, S.; Renshaw, K.; Thompson, M. E.; Forrest, S. R. Solution-Processed Squaraine Bulk Heterojunction Photovoltaic Cells. *ACS Nano* **2010**, *4* (4), 1927–1934.

(41) Wei, G.; Wang, S.; Sun, K.; Thompson, M. E.; Forrest, S. R. Solvent-Annealed Crystalline Squaraine: PC70BM (1:6) Solar Cells. *Adv. Energy Mater.* **2011**, *1* (2), 184–187.

(42) Chan, M. Y.; Lee, C. S.; Lai, S. L.; Fung, M. K.; Wong, F. L.; Sun, H. Y.; Lau, K. M.; Lee, S. T. Efficient Organic Photovoltaic Devices Using a Combination of Exciton Blocking Layer and Anodic Buffer Layer. *J. Appl. Phys.* **2006**, *100* (9), 094506.

(43) Brabec, C. J.; Shaheen, S. E.; Winder, C.; Sariciftci, N. S.; Denk, P. Effect of LiF/Metal Electrodes on the Performance of Plastic Solar Cells. *Appl. Phys. Lett.* **2002**, *80* (7), 1288–1290.

(44) Yu, W.; Huang, L.; Yang, D.; Fu, P.; Zhou, L.; Zhang, J.; Li, C. Efficiency Exceeding 10% for Inverted Polymer Solar Cells with a ZnO/Ionic Liquid Combined Cathode Interfacial Layer. *J. Mater. Chem. A* **2015**, *3* (20), 10660–10665.

(45) Liang, Z.; Zhang, Q.; Wiranwetchayan, O.; Xi, J.; Yang, Z.; Park, K.; Li, C.; Cao, G. Effects of the Morphology of a ZnO Buffer Layer on the Photovoltaic

Performance of Inverted Polymer Solar Cells. *Adv. Funct. Mater.* **2012**, *22* (10), 2194–2201.

(46) Wang, M.; Li, Y.; Huang, H.; Peterson, E. D.; Nie, W.; Zhou, W.; Zeng, W.; Huang, W.; Fang, G.; Sun, N.; et al. Thickness Dependence of the MoO3 Blocking Layers on ZnO Nanorod-Inverted Organic Photovoltaic Devices. *Appl. Phys. Lett.* **2011**, *98* (10).

(47) Girotto, C.; Voroshazi, E.; Cheyns, D.; Heremans, P.; Rand, B. P. Solution-Processed MoO3 Thin Films As a Hole-Injection Layer for Organic Solar Cells. *ACS Appl. Mater. Interfaces* **2011**, *3* (9), 3244–3247.

(48) Zilberberg, K.; Trost, S.; Schmidt, H.; Riedl, T. Solution Processed Vanadium Pentoxide as Charge Extraction Layer for Organic Solar Cells. *Adv. Energy Mater.* **2011**, *1* (3), 377–381.

(49) Shrotriya, V.; Li, G.; Yao, Y.; Chu, C.-W.; Yang, Y. Transition Metal Oxides as the Buffer Layer for Polymer Photovoltaic Cells. *Appl. Phys. Lett.* **2006**, *88* (7), 073508.

(50) Ameri, T.; Dennler, G.; Lungenschmied, C.; J. Brabec, C. Organic Tandem Solar Cells: A Review. *Energy Environ. Sci.* **2009**, *2* (4), 347–363.

(51) Moritz, R.; Christian, U.; Johannes, W.; Ronny, T.; David, W.; Gregor, S.; Wolf-Michael, G.; Dirk, H.; Andre, W.; Jaehyung, H.; et al. Efficient Organic Tandem Solar Cells Based on Small Molecules. *Adv. Funct. Mater. 21* (16), 3019–3028.

(52) Zhao, W.; Li, S.; Yao, H.; Zhang, S.; Zhang, Y.; Yang, B.; Hou, J. Molecular Optimization Enables over 13% Efficiency in Organic Solar Cells. *J. Am. Chem. Soc.* **2017**.

(53) Tress, W. *Organic Solar Cells: Theory, Experiment, and Device Simulation*; Springer Series in Materials Science; Springer International Publishing, 2014.

(54) Hoppe, H.; Sariciftci, N. S. Organic Solar Cells: An Overview. *J. Mater. Res.* **2004**, *19* (7), 1924–1945.

(55) Yang, X.; Loos, J.; Veenstra, S. C.; Verhees, W. J. H.; Wienk, M. M.; Kroon, J. M.; Michels, M. A. J.; Janssen, R. A. J. Nanoscale Morphology of High-Performance Polymer Solar Cells. *Nano Lett.* **2005**, *5* (4), 579–583.

(56) Brabec, C. J.; Cravino, A.; Meissner, D.; Sariciftci, N. S.; Fromherz, T.; Rispens, M. T.; Sanchez, L.; Hummelen, J. C. Origin of the Open Circuit Voltage of Plastic Solar Cells. *Adv. Funct. Mater.* **2001**, *11* (5), 374–380.

(57) Koster, L. J. A.; Mihailetchi, V. D.; Blom, P. W. M. Ultimate Efficiency of Polymer/Fullerene Bulk Heterojunction Solar Cells. *Appl. Phys. Lett.* **2006**, *88* (9), 093511.

(58) Gong, X. Toward High Performance Inverted Polymer Solar Cells. *Polymer* **2012**, *53* (24), 5437–5448.

(59) Chen, G.; Sasabe, H.; Sasaki, Y.; Katagiri, H.; Wang, X.-F.; Sano, T.; Hong, Z.; Yang, Y.; Kido, J. A Series of Squaraine Dyes: Effects of Side Chain and the Number of Hydroxyl Groups on Material Properties and Photovoltaic Performance. *Chem. Mater.* **2014**, *26* (3), 1356–1364.

(60) Zhou, J.; Wan, X.; Liu, Y.; Zuo, Y.; Li, Z.; He, G.; Long, G.; Ni, W.; Li, C.; Su, X.; et al. Small Molecules Based on Benzo[1,2-b:4,5-B′]Dithiophene Unit for High-Performance Solution-Processed Organic Solar Cells. *J. Am. Chem. Soc.* **2012**, *134* (39), 16345–16351.

(61) Spano, F. C. The Spectral Signatures of Frenkel Polarons in H- and J-Aggregates. *Acc. Chem. Res.* **2010**, *43* (3), 429–439.

(62) Mizes, H. A.; Conwell, E. M. Polarons and Their Stability in Poly(Phenylenevinylene). *Synth. Met.* **1995**, *68* (2), 145–151.

(63) Hennebicq, E.; Pourtois, G.; Scholes, G. D.; Herz, L. M.; Russell, D. M.; Silva, C.; Setayesh, S.; Grimsdale, A. C.; Müllen, K.; Brédas, J.-L.; et al. Exciton Migration in Rigid-Rod Conjugated Polymers: An Improved Förster Model. *J. Am. Chem. Soc.* **2005**, *127* (13), 4744–4762.

(64) Főrster, T. 10th Spiers Memorial Lecture. Transfer Mechanisms of Electronic Excitation. *Discuss. Faraday Soc.* **1959**, *27* (0), 7–17.

(65) Brabec, C. J.; Zerza, G.; Cerullo, G.; De Silvestri, S.; Luzzati, S.; Hummelen, J. C.; Sariciftci, S. Tracing Photoinduced Electron Transfer Process in Conjugated Polymer/Fullerene Bulk Heterojunctions in Real Time. *Chem. Phys. Lett.* **2001**, *340* (3), 232–236.

(66) Marcus, R. A. Electron Transfer Reactions in Chemistry. Theory and Experiment. *Rev. Mod. Phys.* **1993**, *65* (3), 599–610.

(67) Clarke, T. M.; Durrant, J. R. Charge Photogeneration in Organic Solar Cells. *Chem. Rev.* **2010**, *110* (11), 6736–6767.

(68) Carsten, D.; Thomas, S.; Vladimir, D. Role of the Charge Transfer State in Organic Donor–Acceptor Solar Cells. *Adv. Mater. 22* (37), 4097–4111.

(69) Spencer, S.; Cody, J.; Misture, S.; Cona, B.; Heaphy, P.; Rumbles, G.; Andersen, J.; Collison, C. Critical Electron Transfer Rates for Exciton Dissociation Governed

by Extent of Crystallinity in Small Molecule Organic Photovoltaics. *J. Phys. Chem. C* **2014**, *118* (27), 14840–14847.

(70) Proctor, C. M.; Love, J. A.; Nguyen, T.-Q. Mobility Guidelines for High Fill Factor Solution-Processed Small Molecule Solar Cells. *Adv. Mater.* **2014**, *26* (34), 5957–5961.

(71) Rose, A. Space-Charge-Limited Currents in Solids. *Phys. Rev.* **1955**, *97* (6), 1538–1544.

(72) Blom, P. W. M.; de Jong, M. J. M.; Vleggaar, J. J. M. Electron and Hole Transport in Poly(p-Phenylene Vinylene) Devices. *Appl. Phys. Lett.* **1996**, *68* (23), 3308.

(73) Heeger Alan J. 25th Anniversary Article: Bulk Heterojunction Solar Cells: Understanding the Mechanism of Operation. *Adv. Mater.* **2013**, *26* (1), 10–28.

(74) Sharenko Alexander; Kuik Martijn; Toney Michael F.; Nguyen Thuc-Quyen. Crystallization-Induced Phase Separation in Solution-Processed Small Molecule Bulk Heterojunction Organic Solar Cells. *Adv. Funct. Mater.* **2014**, *24* (23), 3543–3550.

(75) Brabec, C. J.; Heeney, M.; McCulloch, I.; Nelson, J. Influence of Blend Microstructure on Bulk Heterojunction Organic Photovoltaic Performance. *Chem. Soc. Rev.* **2011**, *40* (3), 1185–1199.

(76) Lee, C.; Li, Y.; Lee, W.; Lee, Y.; Choi, J.; Kim, T.; Wang, C.; Gomez, E. D.; Woo, H. Y.; Kim, B. J. Correlation between Phase-Separated Domain Sizes of Active Layer and Photovoltaic Performances in All-Polymer Solar Cells. *Macromolecules* **2016**, *49* (14), 5051–5058.

(77) Takacs, C. J.; Sun, Y.; Welch, G. C.; Perez, L. A.; Liu, X.; Wen, W.; Bazan, G. C.; Heeger, A. J. Solar Cell Efficiency, Self-Assembly, and Dipole–Dipole Interactions of Isomorphic Narrow-Band-Gap Molecules. *J. Am. Chem. Soc.* **2012**, *134* (40), 16597–16606.

(78) Kyaw Aung Ko Ko; Wang Dong Hwan; Luo Chan; Cao Yong; Nguyen Thuc-Quyen; Bazan Guillermo C.; Heeger Alan J. Effects of Solvent Additives on Morphology, Charge Generation, Transport, and Recombination in Solution-Processed Small-Molecule Solar Cells. *Adv. Energy Mater.* **2014**, *4* (7), 1301469.

(79) Kozub, D. R.; Vakhshouri, K.; Orme, L. M.; Wang, C.; Hexemer, A.; Gomez, E. D. Polymer Crystallization of Partially Miscible Polythiophene/Fullerene Mixtures Controls Morphology. *Macromolecules* **2011**, *44* (14), 5722–5726.

(80) Wienk, M. M.; Kroon, J. M.; Verhees, W. J. H.; Knol, J.; Hummelen, J. C.; van Hal, P. A.; Janssen, R. A. J. Efficient Methano[70]Fullerene/MDMO-PPV Bulk

Heterojunction Photovoltaic Cells. *Angew. Chem. Int. Ed.* **2003**, *42* (29), 3371–3375.

(81) Nguyen, L. H.; Hoppe, H.; Erb, T.; Günes, S.; Gobsch, G.; Sariciftci, N. S. Effects of Annealing on the Nanomorphology and Performance of Poly(Alkylthiophene):Fullerene Bulk-Heterojunction Solar Cells. *Adv. Funct. Mater.* **2007**, *17* (7), 1071–1078.

(82) Gadisa, A.; Oosterbaan, W. D.; Vandewal, K.; Bolsée, J.-C.; Bertho, S.; D'Haen, J.; Lutsen, L.; Vanderzande, D.; Manca, J. V. Effect of Alkyl Side-Chain Length on Photovoltaic Properties of Poly(3-Alkylthiophene)/PCBM Bulk Heterojunctions. *Adv. Funct. Mater.* **2009**, *19* (20), 3300–3306.

(83) Min, J.; Luponosov, Y. N.; Gasparini, N.; Richter, M.; Bakirov, A. V.; Shcherbina, M. A.; Chvalun, S. N.; Grodd, L.; Grigorian, S.; Ameri, T.; et al. Effects of Alkyl Terminal Chains on Morphology, Charge Generation, Transport, and Recombination Mechanisms in Solution-Processed Small Molecule Bulk Heterojunction Solar Cells. *Adv. Energy Mater.* **2015**, *5* (17), 1500386.

(84) Marrocchi, A.; Lanari, D.; Facchetti, A.; Vaccaro, L. Poly(3-Hexylthiophene): Synthetic Methodologies and Properties in Bulk Heterojunction Solar Cells. *Energy Environ. Sci.* **2012**, *5* (9), 8457–8474.

(85) Li, G.; Shrotriya, V.; Huang, J.; Yao, Y.; Moriarty, T.; Emery, K.; Yang, Y. High-Efficiency Solution Processable Polymer Photovoltaic Cells by Self-Organization of Polymer Blends. *Nat. Mater.* **2005**, *4*, 864–868.

(86) Ma, W.; Yang, C.; Gong, X.; Lee, K.; Heeger, A. J. Thermally Stable Efficient Polymer Solar Cells with Nanoscale Control of the Interpenetrating Network Morphology. *Adv. Funct. Mater.* **2005**, *15* (Copyright (C) 2014 American Chemical Society (ACS). All Rights Reserved.), 1617–1622.

(87) Song, Y.; Clafton, S. N.; Pensack, R. D.; Kee, T. W.; Scholes, G. D. Vibrational Coherence Probes the Mechanism of Ultrafast Electron Transfer in Polymer–Fullerene Blends. *Nat Commun* **2014**, *5*.

(88) Xu, Z.; Chen, L.-M.; Yang, G.; Huang, C.-H.; Hou, J.; Wu, Y.; Li, G.; Hsu, C.-S.; Yang, Y. Vertical Phase Separation in Poly(3-Hexylthiophene): Fullerene Derivative Blends and Its Advantage for Inverted Structure Solar Cells. *Adv. Funct. Mater.* **2009**, *19* (8), 1227–1234.

(89) Panzer, F.; Bässler, H.; Lohwasser, R.; Thelakkat, M.; Köhler, A. The Impact of Polydispersity and Molecular Weight on the Order–Disorder Transition in Poly(3-Hexylthiophene). *J. Phys. Chem. Lett.* **2014**, *5* (15), 2742–2747.

(90) Ballantyne, A. M.; Chen, L.; Nelson, J.; Bradley, D. D. C.; Astuti, Y.; Maurano, A.; Shuttle, C. G.; Durrant, J. R.; Heeney, M.; Duffy, W.; et al. Studies of Highly Regioregular Poly(3-Hexylselenophene) for Photovoltaic Applications. *Adv. Mater.* **2007**, *19* (24), 4544–4547.

(91) Liang, Y.; Feng, D.; Wu, Y.; Tsai, S.-T.; Li, G.; Ray, C.; Yu, L. Highly Efficient Solar Cell Polymers Developed via Fine-Tuning of Structural and Electronic Properties. *J. Am. Chem. Soc.* **2009**, *131* (22), 7792–7799.

(92) Zhu, Z.; Waller, D.; Gaudiana, R.; Morana, M.; Mühlbacher, D.; Scharber, M.; Brabec, C. Panchromatic Conjugated Polymers Containing Alternating Donor/Acceptor Units for Photovoltaic Applications. *Macromolecules* **2007**, *40* (6), 1981–1986.

(93) Zou, Y.; Holmes, R. J. Influence of a MoOx Interlayer on the Open-Circuit Voltage in Organic Photovoltaic Cells. *Appl. Phys. Lett.* **2013**, *103* (5), 053302.

(94) You, J.; Chen, C.-C.; Hong, Z.; Yoshimura, K.; Ohya, K.; Xu, R.; Ye, S.; Gao, J.; Li, G.; Yang, Y. 10.2% Power Conversion Efficiency Polymer Tandem Solar Cells Consisting of Two Identical Sub-Cells. *Adv. Mater.* **2013**, *25* (29), 3973–3978.

(95) Kumar, C. V.; Cabau, L.; Viterisi, A.; Biswas, S.; Sharma, G. D.; Palomares, E. Solvent Annealing Control of Bulk Heterojunction Organic Solar Cells with 6.6% Efficiency Based on a Benzodithiophene Donor Core and Dicyano Acceptor Units. *J. Phys. Chem. C* **2015**, *119* (36), 20871–20879.

(96) Mikhnenko, O. V.; Lin, J.; Shu, Y.; Anthony, J. E.; Blom, P. W. M.; Nguyen, T.-Q.; Loi, M. A. Effect of Thermal Annealing on Exciton Diffusion in a Diketopyrrolopyrrole Derivative. *Phys. Chem. Chem. Phys.* **2012**, *14* (41), 14196–14201.

(97) Liu, Y.; Chen, C.-C.; Hong, Z.; Gao, J.; (Michael) Yang, Y.; Zhou, H.; Dou, L.; Li, G.; Yang, Y. Solution-Processed Small-Molecule Solar Cells: Breaking the 10% Power Conversion Efficiency. *Sci. Rep.* **2013**, *3*, 3356.

(98) Jiang, B.; Yao, J.; Zhan, C. Modulating PCBM-Acceptor Crystallinity and Organic Solar Cell Performance by Judiciously Designing Small-Molecule Mainchain End-Capping Units. *ACS Appl. Mater. Interfaces* **2016**, *8* (39), 26058–26065.

(99) Liu, X.; Sun, Y.; Hsu, B. B. Y.; Lorbach, A.; Qi, L.; Heeger, A. J.; Bazan, G. C. Design and Properties of Intermediate-Sized Narrow Band-Gap Conjugated Molecules Relevant to Solution-Processed Organic Solar Cells. *J. Am. Chem. Soc.* **2014**, *136* (15), 5697–5708.

(100) Welch, G. C.; Perez, L. A.; Hoven, C. V.; Zhang, Y.; Dang, X.-D.; Sharenko, A.; Toney, M. F.; Kramer, E. J.; Nguyen, T.-Q.; Bazan, G. C. A Modular Molecular

Framework for Utility in Small-Molecule Solution-Processed Organic Photovoltaic Devices. *J. Mater. Chem.* **2011**, *21* (34), 12700–12709.

(101) Walker, B.; Kim, C.; Nguyen, T.-Q. Small Molecule Solution-Processed Bulk Heterojunction Solar Cells. *Chem. Mater.* **2011**, *23* (3), 470–482.

(102) Deing, K. C.; Mayerhoffer, U.; Wurthner, F.; Meerholz, K. Aggregation-Dependent Photovoltaic Properties of Squaraine/PC61BM Bulk Heterojunctions. *Phys. Chem. Chem. Phys.* **2012**, *14* (23), 8328–8334.

(103) Arjona-Esteban, A.; Krumrain, J.; Liess, A.; Stolte, M.; Huang, L.; Schmidt, D.; Stepanenko, V.; Gsänger, M.; Hertel, D.; Meerholz, K.; et al. Influence of Solid-State Packing of Dipolar Merocyanine Dyes on Transistor and Solar Cell Performances. *J. Am. Chem. Soc.* **2015**, *137* (42), 13524–13534.

(104) Chen, G.; Sasabe, H.; Lu, W.; Wang, X.-F.; Kido, J.; Hong, Z.; Yang, Y. J-Aggregation of a Squaraine Dye and Its Application in Organic Photovoltaic Cells. *J. Mater. Chem. C* **2013**, *1* (40), 6547–6552.

(105) Kasha, M.; Rawls, H.; El-Bayoumi, A. The Exciton Model in Molecular Spectroscopy. *Pure Appl. Chem.* **1965**, *11* (3–4), 371–392.

(106) Spano, F. C.; Silva, C. H- and J-Aggregate Behavior in Polymeric Semiconductors. *Annu. Rev. Phys. Chem.* **2014**, *65* (1), 477–500.

(107) Terenziani, F.; Painelli, A.; Katan, C.; Charlot, M.; Blanchard-Desce, M. Charge Instability in Quadrupolar Chromophores: Symmetry Breaking and Solvatochromism. *J. Am. Chem. Soc.* **2006**, *128* (49), 15742–15755.

(108) Shafeekh, K. M.; Das, S.; Sissa, C.; Painelli, A. Asymmetric Squaraine Dyes: Spectroscopic and Theoretical Investigation. *J. Phys. Chem. B* **2013**, *117* (28), 8536–8546.

(109) Boldrini, B.; Cavalli, E.; Painelli, A.; Terenziani, F. Polar Dyes in Solution: A Joint Experimental and Theoretical Study of Absorption and Emission Band Shapes. *J. Phys. Chem. A* **2002**, *106* (26), 6286–6294.

(110) Grisanti, L.; D'Avino, G.; Painelli, A.; Guasch, J.; Ratera, I.; Veciana, J. Essential State Models for Solvatochromism in Donor−Acceptor Molecules: The Role of the Bridge. *J. Phys. Chem. B* **2009**, *113* (14), 4718–4725.

(111) Liu, T.; Liu, X.; Wang, W.; Luo, Z.; Liu, M.; Zou, S.; Sissa, C.; Painelli, A.; Zhang, Y.; Vengris, M.; et al. Systematic Molecular Engineering of a Series of Aniline-Based Squaraine Dyes and Their Structure-Related Properties. *J. Phys. Chem. C* **2018**, *122* (7), 3994–4008.

(112) Kurhuzenkau, S. A.; Colon Gomez, M. Y.; Belfield, K. D.; Shaydyuk, Y. O.; Hagan, D. J.; Van Stryland, E. W.; Sissa, C.; Bondar, M. V.; Painelli, A. Electronic Nature of Nonlinear Optical Properties of a Symmetrical Two-Photon Absorbing Fluorene Derivative: Experimental Study and Theoretical Modeling. *J. Phys. Chem. C* **2018**, *122* (10), 5664–5672.

(113) D'Avino, G.; Terenziani, F.; Painelli, A. Aggregates of Quadrupolar Dyes: Giant Two-Photon Absorption from Biexciton States. *J. Phys. Chem. B* **2006**, *110* (51), 25590–25592.

(114) Sanyal, S.; Painelli, A.; Pati, S. K.; Terenziani, F.; Sissa, C. Aggregates of Quadrupolar Dyes for Two-Photon Absorption: The Role of Intermolecular Interactions. *Phys. Chem. Chem. Phys.* **2016**, *18* (40), 28198–28208.

(115) Dirk, C. W.; Herndon, W. C.; Cervantes-Lee, F.; Selnau, H.; Martinez, S.; Kalamegham, P.; Tan, A.; Campos, G.; Velez, M. Squarylium Dyes: Structural Factors Pertaining to the Negative Third-Order Nonlinear Optical Response. *J. Am. Chem. Soc.* **1995**, *117* (8), 2214–2225.

(116) Law, K.-Y. Squaraine Chemistry. Absorption, Fluorescence Emission, and Photophysics of Unsymmetrical Squaraines. *J. Phys. Chem.* **1995**, *99* (24), 9818–9824.

(117) Law, K. Y. Squaraine Chemistry. A Study of the Solute-Solvent Complexation of Squaraine in Solvents by Proton NMR Spectroscopy. *J. Phys. Chem.* **1989**, *93* (15), 5925–5930.

(118) Silvestri, F.; Irwin, M. D.; Beverina, L.; Facchetti, A.; Pagani, G. A.; Marks, T. J. Efficient Squaraine-Based Solution Processable Bulk-Heterojunction Solar Cells. *J. Am. Chem. Soc.* **2008**, *130* (52), 17640–17641.

(119) Bagnis, D.; Beverina, L.; Huang, H.; Silvestri, F.; Yao, Y.; Yan, H.; Pagani, G. A.; Marks, T. J.; Facchetti, A. Marked Alkyl- vs Alkenyl-Substitutent Effects on Squaraine Dye Solid-State Structure, Carrier Mobility, and Bulk-Heterojunction Solar Cell Efficiency. *J. Am. Chem. Soc.* **2010**, *132* (12), 4074–4075.

(120) Wang, S.; Mayo, E. I.; Perez, M. D.; Griffe, L.; Wei, G.; Djurovich, P. I.; Forrest, S. R.; Thompson, M. E. High Efficiency Organic Photovoltaic Cells Based on a Vapor Deposited Squaraine Donor. *Appl. Phys. Lett.* **2009**, *94* (23), 233304.

(121) Wei, G.; Lunt, R. R.; Sun, K.; Wang, S.; Thompson, M. E.; Forrest, S. R. Efficient, Ordered Bulk Heterojunction Nanocrystalline Solar Cells by Annealing of Ultrathin Squaraine Thin Films. *Nano Lett.* **2010**, *10* (9), 3555–3559.

(122) Wang, S.; Hall, L.; Diev, V. V.; Haiges, R.; Wei, G.; Xiao, X.; Djurovich, P. I.; Forrest, S. R.; Thompson, M. E. N,N-Diarylanilinosquaraines and Their Application to Organic Photovoltaics. *Chem. Mater.* **2011**, *23* (21), 4789–4798.

(123) Xiao, X.; Wei, G.; Wang, S.; Zimmerman, J. D.; Renshaw, C. K.; Thompson, M. E.; Forrest, S. R. Small-Molecule Photovoltaics Based on Functionalized Squaraine Donor Blends. *Adv. Mater.* **2012**, *24* (15), 1956–1960.

(124) Wei, G.; Xiao, X.; Wang, S.; Sun, K.; Bergemann, K. J.; Thompson, M. E.; Forrest, S. R. Functionalized Squaraine Donors for Nanocrystalline Organic Photovoltaics. *ACS Nano* **2012**, *6* (1), 972–978.

(125) Wei, G.; Xiao, X.; Wang, S.; Zimmerman, J. D.; Sun, K.; Diev, V. V.; Thompson, M. E.; Forrest, S. R. Arylamine-Based Squaraine Donors for Use in Organic Solar Cells. *Nano Lett.* **2011**, *11* (10), 4261–4264.

(126) Chen, G.; Sasabe, H.; Wang, Z.; Wang, X.; Hong, Z.; Kido, J.; Yang, Y. Solution-Processed Organic Photovoltaic Cells Based on a Squaraine Dye. *Phys. Chem. Chem. Phys.* **2012**, *14* (42), 14661–14666.

(127) Chen, G.; Sasabe, H.; Wang, Z.; Wang, X.-F.; Hong, Z.; Yang, Y.; Kido, J. Co-Evaporated Bulk Heterojunction Solar Cells with >6.0% Efficiency. *Adv. Mater.* **2012**, *24* (20), 2768–2773.

(128) Yang, D.; Jiao, Y.; Yang, L.; Chen, Y.; Mizoi, S.; Huang, Y.; Pu, X.; Lu, Z.; Sasabe, H.; Kido, J. Cyano-Substitution on the End-Capping Group: Facile Access toward Asymmetrical Squaraine Showing Strong Dipole–Dipole Interactions as a High Performance Small Molecular Organic Solar Cells Material. *J. Mater. Chem. A* **2015**, *3* (34), 17704–17712.

(129) Yang, L.; Yang, D.; Chen, Y.; Luo, Q.; Zhang, M.; Huang, Y.; Lu, Z.; Sasabe, H.; Kido, J. Unsymmetrical Squaraines with New Linkage Manner for High-Performance Solution-Processed Small-Molecule Organic Photovoltaic Cells. *RSC Adv.* **2015**, *6* (3), 1877–1884.

(130) Yang, D.; Jiao, Y.; Huang, Y.; Zhuang, T.; Yang, L.; Lu, Z.; Pu, X.; Sasabe, H.; Kido, J. Two Different Donor Subunits Substituted Unsymmetrical Squaraines for Solution-Processed Small Molecule Organic Solar Cells. *Org. Electron.* **2016**, *32*, 179–186.

(131) Yang, D.; Yang, Q.; Yang, L.; Luo, Q.; Huang, Y.; Lu, Z.; Zhao, S. Novel High Performance Asymmetrical Squaraines for Small Molecule Organic Solar Cells with a High Open Circuit Voltage of 1.12 V. *Chem. Commun.* **2013**, *49* (89), 10465–10467.

(132) Yang, D.; Yang, Q.; Yang, L.; Luo, Q.; Chen, Y.; Zhu, Y.; Huang, Y.; Lu, Z.; Zhao, S. A Low Bandgap Asymmetrical Squaraine for High-Performance Solution-Processed Small Molecule Organic Solar Cells. *Chem. Commun.* **2014**, *50* (66), 9346–9348.

(133) Spencer, S. D.; Bougher, C.; Heaphy, P. J.; Murcia, V. M.; Gallivan, C. P.; Monfette, A.; Andersen, J. D.; Cody, J. A.; Conrad, B. R.; Collison, C. J. The Effect of Controllable Thin Film Crystal Growth on the Aggregation of a Novel High Panchromaticity Squaraine Viable for Organic Solar Cells. *Sol. Energy Mater. Sol. Cells* **2013**, *112*, 202–208.

(134) Spencer, S.; Hu, H.; Li, Q.; Ahn, H.-Y.; Qaddoura, M.; Yao, S.; Ioannidis, A.; Belfield, K.; Collison, C. J. Controlling J-Aggregate Formation for Increased Short-Circuit Current and Power Conversion Efficiency with a Squaraine Donor. *Prog. Photovolt. Res. Appl.* **2012**, n/a–n/a.

(135) Bigelow, R. W.; Freund, H.-J. An MNDO and CNDO / S(S + DES CI) Study on the Structural and Electronic Properties of a Model Squaraine Dye and Related Cyanine. *Chem. Phys.* **1986**, *107* (2), 159–174.

(136) Hestand, N. J.; Zheng, C.; Penmetcha, A. R.; Cona, B.; Cody, J. A.; Spano, F. C.; Collison, C. J. Confirmation of the Origins of Panchromatic Spectra in Squaraine Thin Films Targeted for Organic Photovoltaic Devices. *J. Phys. Chem. C* **2015**, *119* (33), 18964–18974.

(137) McKerrow, A. J.; Buncel, E.; Kazmaier, P. M. Aggregation of Squaraine Dyes: Structure–Property Relationships and Solvent Effects. *Can. J. Chem.* **1995**, *73* (10), 1605–1615.

(138) Cerullo, G.; Nisoli, M.; Stagira, S.; Silvestri, S. D. Sub-8-Fs Pulses from an Ultrabroadband Optical Parametric Amplifier in the Visible. *Opt. Lett.* **1998**, *23* (16), 1283–1285.

(139) Cerullo, G.; De Silvestri, S. Ultrafast Optical Parametric Amplifiers. *Rev. Sci. Instrum.* **2003**, *74* (1), 1–18.

(140) Su, Y.-W.; Lan, S.-C.; Wei, K.-H. Organic Photovoltaics. *Mater. Today* **2012**, *15* (12), 554–562.

(141) Lu, L.; Zheng, T.; Wu, Q.; Schneider, A. M.; Zhao, D.; Yu, L. Recent Advances in Bulk Heterojunction Polymer Solar Cells. *Chem. Rev.* **2015**, *115* (23), 12666–12731.

(142) Mukherjee, S.; Proctor, C. M.; Tumbleston, J. R.; Bazan, G. C.; Nguyen, T.-Q.; Ade, H. Importance of Domain Purity and Molecular Packing in Efficient Solution-Processed Small-Molecule Solar Cells. *Adv. Mater.* **2015**, *27* (6), 1105–1111.

(143) Müller, C.; Ferenczi, T. A. M.; Campoy-Quiles, M.; Frost, J. M.; Bradley, D. D. C.; Smith, P.; Stingelin-Stutzmann, N.; Nelson, J. Binary Organic Photovoltaic Blends: A Simple Rationale for Optimum Compositions. *Adv. Mater.* **2008**, *20* (18), 3510–3515.

(144) Kozub, D. R.; Vakhshouri, K.; Orme, L. M.; Wang, C.; Hexemer, A.; Gomez, E. D. Polymer Crystallization of Partially Miscible Polythiophene/Fullerene Mixtures Controls Morphology. *Macromolecules* **2011**, *44* (14), 5722–5726.

(145) Zheng, C.; Penmetcha, A. R.; Cona, B.; Spencer, S. D.; Zhu, B.; Heaphy, P.; Cody, J. A.; Collison, C. J. Contribution of Aggregate States and Energetic Disorder to a Squaraine System Targeted for Organic Photovoltaic Devices. *Langmuir* **2015**, *31* (28), 7717–7726.

(146) Chen, G.; Sasabe, H.; Igarashi, T.; Hong, Z.; Kido, J. Squaraine Dyes for Organic Photovoltaic Cells. *J. Mater. Chem. A* **2015**, *3* (28), 14517–14534.

(147) Yang, D.; Sasabe, H.; Jiao, Y.; Zhuang, T.; Huang, Y.; Pu, X.; Sano, T.; Lu, Z.; Kido, J. An Effective π-Extended Squaraine for Solution-Processed Organic Solar Cells with High Efficiency. *J. Mater. Chem. A* **2016**, *4* (48), 18931–18941.

(148) Sasabe, H.; Igrashi, T.; Sasaki, Y.; Chen, G.; Hong, Z.; Kido, J. Soluble Squaraine Derivatives for 4.9% Efficient Organic Photovoltaic Cells. *RSC Adv.* **2014**, *4* (81), 42804–42807.

(149) Bruck, S.; Krause, C.; Turrisi, R.; Beverina, L.; Wilken, S.; Saak, W.; Lutzen, A.; Borchert, H.; Schiek, M.; Parisi, J. Structure-Property Relationship of Anilino-Squaraines in Organic Solar Cells. *Phys. Chem. Chem. Phys.* **2014**, *16* (3), 1067–1077.

(150) Spano, F. C.; Clark, J.; Silva, C.; Friend, R. H. Determining Exciton Coherence from the Photoluminescence Spectral Line Shape in Poly(3-Hexylthiophene) Thin Films. *J. Chem. Phys.* **2009**, *130* (7), 074904.

(151) Benson-Smith, J. J.; Goris, L.; Vandewal, K.; Haenen, K.; Manca, J. V.; Vanderzande, D.; Bradley, D. D. C.; Nelson, J. Formation of a Ground-State Charge-Transfer Complex in Polyfluorene//[6,6]-Phenyl-C61 Butyric Acid Methyl Ester (PCBM) Blend Films and Its Role in the Function of Polymer/PCBM Solar Cells. *Adv. Funct. Mater.* **2007**, *17* (3), 451–457.

(152) Lakowicz, J. *Principles of Fluorescence Spectroscopy*; Principles of Fluorescence Spectroscopy; Kluwer Academic/Plenum Publishers: New York, Boston, Dordrecht, London, Moscow, 1999.

(153) Brück, S.; Krause, C.; Turrisi, R.; Beverina, L.; Wilken, S.; Saak, W.; Lützen, A.; Borchert, H.; Schiek, M.; Parisi, J. Structure–Property Relationship of Anilino-

Squaraines in Organic Solar Cells. *Phys. Chem. Chem. Phys.* **2013**, *16* (3), 1067–1077.

(154) Viterisi, A.; Montcada, N. F.; Kumar, C. V.; Gispert-Guirado, F.; Martin, E.; Escudero, E.; Palomares, E. Unambiguous Determination of Molecular Packing in Crystalline Donor Domains of Small Molecule Solution Processed Solar Cell Devices Using Routine X-Ray Diffraction Techniques. *J. Mater. Chem. A* **2014**, *2* (10), 3536–3542.

(155) Vandewal, K.; Himmelberger, S.; Salleo, A. Structural Factors That Affect the Performance of Organic Bulk Heterojunction Solar Cells. *Macromolecules* **2013**, *46* (16), 6379–6387.

(156) Scharber, M. C.; Mühlbacher, D.; Koppe, M.; Denk, P.; Waldauf, C.; Heeger, A. J.; Brabec, C. J. Design Rules for Donors in Bulk-Heterojunction Solar Cells—Towards 10 % Energy-Conversion Efficiency. *Adv. Mater.* **2006**, *18* (6), 789–794.

(157) Dennler, G.; Scharber, M. C.; Brabec, C. J. Polymer-Fullerene Bulk-Heterojunction Solar Cells. *Adv. Mater.* **2009**, *21* (13), 1323–1338.

(158) Tian, M.; Furuki, M.; Iwasa, I.; Sato, Y.; Pu, L. S.; Tatsuura, S. Search for Squaraine Derivatives That Can Be Sublimed without Thermal Decomposition. *J. Phys. Chem. B* **2002**, *106* (17), 4370–4376.

(159) Bulle-Lieuwma, C. W. T.; van Gennip, W. J. H.; van Duren, J. K. J.; Jonkheijm, P.; Janssen, R. A. J.; Niemantsverdriet, J. W. Characterization of Polymer Solar Cells by TOF-SIMS Depth Profiling. *Appl. Surf. Sci.* **2003**, *203–204*, 547–550.

(160) Geens, W.; Martens, T.; Poortmans, J.; Aernouts, T.; Manca, J.; Lutsen, L.; Heremans, P.; Borghs, S.; Mertens, R.; Vanderzande, D. Modelling the Short-Circuit Current of Polymer Bulk Heterojunction Solar Cells. *Thin Solid Films* **2004**, *451–452*, 498–502.

(161) McCulloch, B.; Ho, V.; Hoarfrost, M.; Stanley, C.; Do, C.; Heller, W. T.; Segalman, R. A. Polymer Chain Shape of Poly(3-Alkylthiophenes) in Solution Using Small-Angle Neutron Scattering. *Macromolecules* **2013**, *46* (5), 1899–1907.

(162) Leem, J. W.; Yu, J. S. Glancing Angle Deposited ITO Films for Efficiency Enhancement of A-Si:H/Mc-Si:H Tandem Thin Film Solar Cells. *Opt. Express* **2011**, *19* (103), A258–A269.

(163) Shin, C.-K.; Lee, H. Effect of Alkyl Side-Chain Length and Solvent on the Luminescent Characteristics of Poly(3-n-Alkylthiophene). *Synth. Met.* **2004**, *140* (2–3), 177–181.

(164) Proctor, C. M.; Kuik, M.; Nguyen, T.-Q. Charge Carrier Recombination in Organic Solar Cells. *Prog. Polym. Sci.* **2013**, *38* (12), 1941–1960.

(165) Walker, B.; Tamayo, A. B.; Dang, X.-D.; Zalar, P.; Seo, J. H.; Garcia, A.; Tantiwiwat, M.; Nguyen, T.-Q. Nanoscale Phase Separation and High Photovoltaic Efficiency in Solution-Processed, Small-Molecule Bulk Heterojunction Solar Cells. *Adv. Funct. Mater.* **2009**, *19* (19), 3063–3069.

(166) Mott, N. F.; Gurney, R. W. *Electronic Processes in Ionic Crystals*; 1940.

(167) Zheng, C.; Jalan, I.; Cost, P.; Oliver, K.; Gupta, A.; Misture, S.; Cody, J. A.; Collison, C. J. Impact of Alkyl Chain Length on Small Molecule Crystallization and Nanomorphology in Squaraine-Based Solution Processed Solar Cells. *J. Phys. Chem. C* **2017**, *121* (14), 7750–7760.

(168) Schwenn, P. E.; Gui, K.; Zhang, Y.; Burn, P. L.; Meredith, P.; Powell, B. J. Kinetics of Charge Transfer Processes in Organic Solar Cells: Implications for the Design of Acceptor Molecules. *Org. Electron.* **2012**, *13* (11), 2538–2545.

(169) Coffey, D. C.; Larson, B. W.; Hains, A. W.; Whitaker, J. B.; Kopidakis, N.; Boltalina, O. V.; Strauss, S. H.; Rumbles, G. An Optimal Driving Force for Converting Excitons into Free Carriers in Excitonic Solar Cells. *J. Phys. Chem. C* **2012**, *116* (16), 8916–8923.

(170) Spencer, S.; Cody, J.; Misture, S.; Cona, B.; Heaphy, P.; Rumbles, G.; Andersen, J.; Collison, C. Critical Electron Transfer Rates for Exciton Dissociation Governed by Extent of Crystallinity in Small Molecule Organic Photovoltaics. *J. Phys. Chem. C* **2014**, *118* (27), 14840–14847.

(171) Spencer, S. D.; Bougher, C.; Heaphy, P. J.; Murcia, V. M.; Gallivan, C. P.; Monfette, A.; Andersen, J. D.; Cody, J. A.; Conrad, B. R.; Collison, C. J. The Effect of Controllable Thin Film Crystal Growth on the Aggregation of a Novel High Panchromaticity Squaraine Viable for Organic Solar Cells. *Sol. Energy Mater. Sol. Cells* **2013**, *112*, 202–208.

(172) Zhang, Y.; Kim, B.; Yao, S.; Bondar, M. V.; Belfield, K. D. Controlled Aggregation and Enhanced Two-Photon Absorption of a Water-Soluble Squaraine Dye with a Poly(Acrylic Acid) Template. *Langmuir* **2013**, *29* (35), 11005–11012.

(173) Gräf, K.; Rahim, M. A.; Das, S.; Thelakkat, M. Complementary Co-Sensitization of an Aggregating Squaraine Dye in Solid-State Dye-Sensitized Solar Cells. *Dyes Pigments* **2013**, *99* (3), 1101–1106.

(174) Pisoni, D. dos S.; de Abreu, M. P.; Petzhold, C. L.; Rodembusch, F. S.; Campo, L. F. Synthesis, Photophysical Study and BSA Association of Water-Insoluble Squaraine Dyes. *J. Photochem. Photobiol. Chem.* **2013**, *252*, 77–83.

(175) Deing, K. C.; Mayerhöffer, U.; Würthner, F.; Meerholz, K. Aggregation-Dependent Photovoltaic Properties of Squaraine/PC61BM Bulk Heterojunctions. *Phys. Chem. Chem. Phys.* **2012**, *14* (23), 8328.

(176) Spano, F. C. The Spectral Signatures of Frenkel Polarons in H- and J-Aggregates. *Acc. Chem. Res.* **2010**, *43* (3), 429–439.

(177) Spano, F. C. Analysis of the UV/Vis and CD Spectral Line Shapes of Carotenoid Assemblies: Spectral Signatures of Chiral H-Aggregates. *J. Am. Chem. Soc.* **2009**, *131* (12), 4267–4278.

(178) Richard W. Bigelow, H.-J. F. An MNDO and CNDO / S(S DES CI) Study on the Structural and Electronic Properties of a Model Squaraine Dye and Related Cyanine. *Chem. Phys.* **1986**, *107* (2–3), 159–174.

(179) Turro, N. J.; Ramamurthy, V.; Scaiano, J. C. Modern Molecular Photochemistry of Organic Molecules. *Photochem. Photobiol.* **2012**, *88* (4), 1033–1033.

(180) Spano, F. C. Analysis of the UV/Vis and CD Spectral Line Shapes of Carotenoid Assemblies: Spectral Signatures of Chiral H-Aggregates. *J. Am. Chem. Soc.* **2009**, *131* (12), 4267–4278.

(181) Más-Montoya Miriam; Janssen René A. J. The Effect of H- and J-Aggregation on the Photophysical and Photovoltaic Properties of Small Thiophene–Pyridine–DPP Molecules for Bulk-Heterojunction Solar Cells. *Adv. Funct. Mater.* **2017**, *27* (16), 1605779.

(182) Tristani-Kendra, M.; Eckhardt, C. J. Influence of Crystal Fields on the Quasimetallic Reflection Spectra of Crystals: Optical Spectra of Polymorphs of a Squarylium Dye. *J. Chem. Phys.* **1984**, *81* (3), 1160–1173.

(183) Tanaka, J.; Tanaka, M.; Hayakawa, M. Electronic Spectra of Single Crystals of 1,1′-Diethyl-2,2′-Cyanine Iodide, Bromide, and Chloride. *Bull. Chem. Soc. Jpn.* **1980**, *53* (11), 3109–3119.

(184) Guasch, J.; Grisanti, L.; Souto, M.; Lloveras, V.; Vidal-Gancedo, J.; Ratera, I.; Painelli, A.; Rovira, C.; Veciana, J. Intra- and Intermolecular Charge Transfer in Aggregates of Tetrathiafulvalene-Triphenylmethyl Radical Derivatives in Solution. *J. Am. Chem. Soc.* **2013**, *135* (18), 6958–6967.

(185) Hestand, N. J.; Spano, F. C. Interference between Coulombic and CT-Mediated Couplings in Molecular Aggregates: H- to J-Aggregate Transformation in Perylene-Based π-Stacks. *J. Chem. Phys.* **2015**, *143* (24), 244707.

(186) Collison, C. J.; Rothberg, L. J.; Treemaneekarn, V.; Li, Y. Conformational Effects on the Photophysics of Conjugated Polymers: A Two Species Model for

MEH−PPV Spectroscopy and Dynamics. *Macromolecules* **2001**, *34* (7), 2346–2352.

(187) Tamai, Y.; Matsuura, Y.; Ohkita, H.; Benten, H.; Ito, S. One-Dimensional Singlet Exciton Diffusion in Poly(3-Hexylthiophene) Crystalline Domains. *J. Phys. Chem. Lett.* **2014**, *5* (2), 399–403.

(188) Valleau, S.; Saikin, S. K.; Yung, M.-H.; Guzik, A. A. Exciton Transport in Thin-Film Cyanine Dye J-Aggregates. *J. Chem. Phys.* **2012**, *137* (3), 034109.

(189) Sung, J.; Kim, P.; Fimmel, B.; Würthner, F.; Kim, D. Direct Observation of Ultrafast Coherent Exciton Dynamics in Helical π-Stacks of Self-Assembled Perylene Bisimides. *Nat. Commun.* **2015**, *6*, 8646.

(190) Hestand, N. J.; Spano, F. C. Molecular Aggregate Photophysics beyond the Kasha Model: Novel Design Principles for Organic Materials. *Acc. Chem. Res.* **2017**, *50* (2), 341–350.

(191) Hestand, N. J.; Spano, F. C. Expanded Theory of H- and J-Molecular Aggregates: The Effects of Vibronic Coupling and Intermolecular Charge Transfer. *Chem. Rev.* **2018**.

(192) Verma, S.; Ghosh, A.; Das, A.; Ghosh, H. N. Ultrafast Exciton Dynamics of J- and H-Aggregates of the Porphyrin-Catechol in Aqueous Solution. *J. Phys. Chem. B* **2010**, *114* (25), 8327–8334.

(193) Spencer, S.; Hu, H.; Li, Q.; Ahn, H.-Y.; Qaddoura, M.; Yao, S.; Ioannidis, A.; Belfield, K.; Collison, C. J. Controlling J-Aggregate Formation for Increased Short-Circuit Current and Power Conversion Efficiency with a Squaraine Donor. *Prog. Photovolt. Res. Appl.* **2014**, *22* (4), 488–493.

(194) Zheng, C.; Bleier, D.; Jalan, I.; Pristash, S.; Penmetcha, A. R.; Hestand, N. J.; Spano, F. C.; Pierce, M. S.; Cody, J. A.; Collison, C. J. Phase Separation, Crystallinity and Monomer-Aggregate Population Control in Solution Processed Small Molecule Solar Cells. *Sol. Energy Mater. Sol. Cells* **2016**, *157*, 366–376.

(195) Zheng, C.; Jalan, I.; Cody, J. A.; Collison, C. J. Small Molecule with Extended Alkyl Side Substituents for Organic Solar Cells. *MRS Adv.* **2016**, 1–7.

(196) Verma, S.; Ghosh, H. N. Exciton Energy and Charge Transfer in Porphyrin Aggregate/Semiconductor (TiO2) Composites. *J. Phys. Chem. Lett.* **2012**, *3* (14), 1877–1884.

(197) Zheng, C. Spectral Properties of Squaraines and Their Aggregates, Targeted for Use in Bulk Hetero-Junction Solar Cells. M.S., Rochester Institute of Technology: United States -- New York, 2015.

(198) Miguel, G. de; Marchena, M.; Zitnan, M.; Pandey, S. S.; Hayase, S.; Douhal, A. Femto to Millisecond Observations of Indole-Based Squaraine Molecules Photodynamics in Solution. *Phys. Chem. Chem. Phys.* **2012**, *14* (5), 1796–1805.

(199) Feron, K.; Belcher, W. J.; Fell, C. J.; Dastoor, P. C. Organic Solar Cells: Understanding the Role of Förster Resonance Energy Transfer. *Int. J. Mol. Sci.* **2012**, *13* (12), 17019–17047.

(200) Conrad, S.; Uli, W.; Markus, Z.; Heiner, G.; Jochen, H.-E.; Andreas, H.; Rainer, H. Overcoming Kinetic Limitations of Electron Injection in the Dye Solar Cell via Coadsorption and FRET. *ChemPhysChem 9* (5), 793–798.

(201) Zaushitsyn, Y.; Jespersen, K. G.; Valkunas, L.; Sundström, V.; Yartsev, A. Ultrafast Dynamics of Singlet-Singlet and Singlet-Triplet Exciton Annihilation in Poly(3-2-Methoxy-5 Octylphenyl)Thiophene Films. *Phys. Rev. B* **2007**, *75* (19), 195201.

(202) Martini, I. B.; Smith, A. D.; Schwartz, B. J. Exciton-Exciton Annihilation and the Production of Interchain Species in Conjugated Polymer Films: Comparing the Ultrafast Stimulated Emission and Photoluminescence Dynamics of MEH-PPV. *Phys. Rev. B* **2004**, *69* (3), 035204.

(203) Cook, S.; Liyuan, H.; Furube, A.; Katoh, R. Singlet Annihilation in Films of Regioregular Poly(3-Hexylthiophene): Estimates for Singlet Diffusion Lengths and the Correlation between Singlet Annihilation Rates and Spectral Relaxation. *J. Phys. Chem. C* **2010**, *114* (24), 10962–10968.

(204) Völker, S. F.; Schmiedel, A.; Holzapfel, M.; Renziehausen, K.; Engel, V.; Lambert, C. Singlet–Singlet Exciton Annihilation in an Exciton-Coupled Squaraine-Squaraine Copolymer: A Model toward Hetero-J-Aggregates. *J. Phys. Chem. C* **2014**, *118* (31), 17467–17482.

(205) Lewis, A. J.; Ruseckas, A.; Gaudin, O. P. M.; Webster, G. R.; Burn, P. L.; Samuel, I. D. W. Singlet Exciton Diffusion in MEH-PPV Films Studied by Exciton–Exciton Annihilation. *Org. Electron.* **2006**, *7* (6), 452–456.

(206) D, B. S.; A, B. V.; I, G. V.; G, L. A.; P, T. V. Singlet Exciton Annihilation in Anthracene Crystals. *Phys. Status Solidi B 45* (1), 91–97.

(207) Kamat, P. V.; Das, S.; Thomas, K. G.; George, M. V. Photochemistry of Squaraine Dyes. 1. Excited Singlet, Triplet, and Redox States of Bis[4-(Dimethylamino)Phenyl]Squaraine and Bis[4-(Dimethylamino)-2-Hydroxyphenyl]Squaraine. *J. Phys. Chem.* **1992**, *96* (1), 195–199.

(208) Bartelt, J. A.; Lam, D.; Burke, T. M.; Sweetnam, S. M.; McGehee, M. D. Charge-Carrier Mobility Requirements for Bulk Heterojunction Solar Cells with High Fill

Factor and External Quantum Efficiency >90%. *Adv. Energy Mater.* **2015**, *5* (15), n/a-n/a.

(209) Andersson, L. M.; Müller, C.; Badada, B. H.; Zhang, F.; Würfel, U.; Inganäs, O. Mobility and Fill Factor Correlation in Geminate Recombination Limited Solar Cells. *J. Appl. Phys.* **2011**, *110* (2), 024509.

(210) Wöbkenberg, P. H.; Bradley, D. D. C.; Kronholm, D.; Hummelen, J. C.; de Leeuw, D. M.; Cölle, M.; Anthopoulos, T. D. High Mobility N-Channel Organic Field-Effect Transistors Based on Soluble C60 and C70 Fullerene Derivatives. *Synth. Met.* **2008**, *158* (11), 468–472.

(211) Koster, L. J. A.; Smits, E. C. P.; Mihailetchi, V. D.; Blom, P. W. M. Device Model for the Operation of Polymer/Fullerene Bulk Heterojunction Solar Cells. *Phys. Rev. B* **2005**, *72* (8), 085205.

(212) Terenziani, F.; D'Avino, G.; Painelli, A. Multichromophores for Nonlinear Optics: Designing the Material Properties by Electrostatic Interactions. *Chemphyschem Eur. J. Chem. Phys. Phys. Chem.* **2007**, *8* (17), 2433–2444.

(213) Varma, P. C. R.; Namboothiry, M. A. G. Squaraine Based Solution Processed Inverted Bulk Heterojunction Solar Cells Processed in Air. *Phys. Chem. Chem. Phys.* **2016**, *18* (5), 3438–3443.

Appendix A. SUPPORTING FIGURES

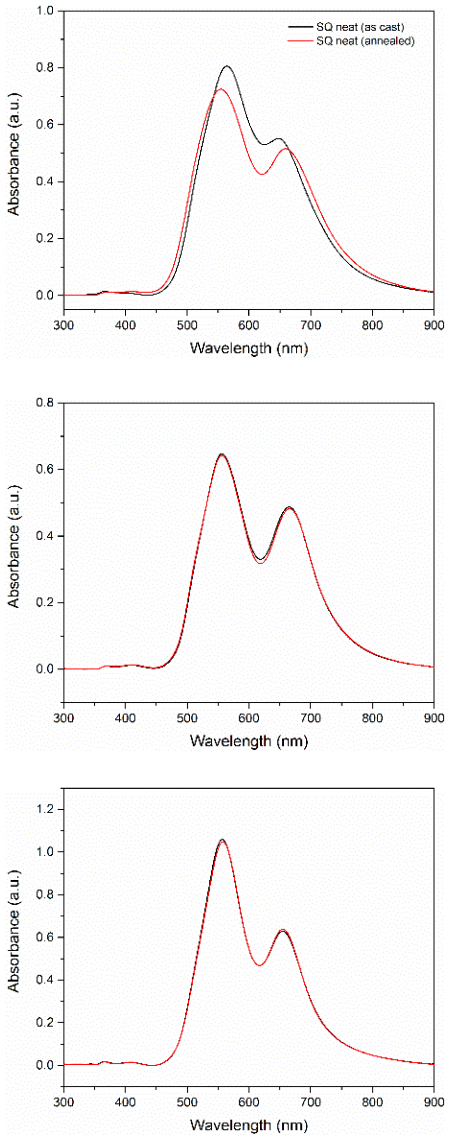

Figure A1 Absorbance spectra of $DBSQ(OH)_2$ (top), $DPSQ(OH)_2$ (middle) and $DHSQ(OH)_2$ (bottom) neat films before and after annealing at 90 ^{0}C. Films are spin cast from chloroform solution ([SQ] = 12 mg/mL) at a spin speed of 1500 RPM. For $DPSQ(OH)_2$ and $DHSQ(OH)_2$ neat films, there is little change in absorbance spectra after thermal annealing; for $DBSQ(OH)_2$ neat film, the two absorbance peaks at 565 nm and 648 nm further split to 555 nm and 660 nm, respectively, after 5 min annealing at 90 ^{0}C.

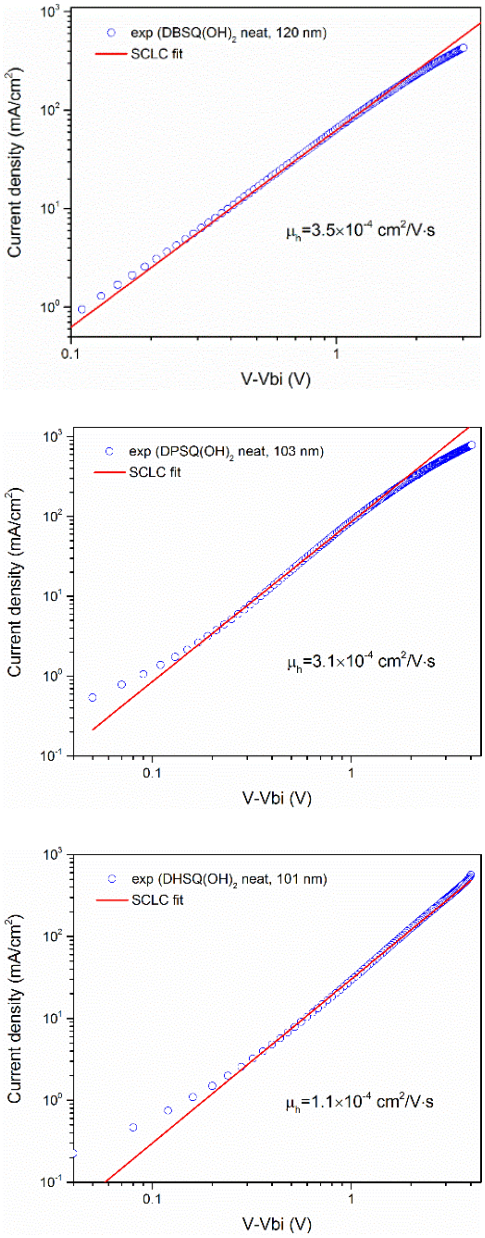

Figure A2 Representative J-V curves (blue dots) as well as the space-charge limited current (SCLC) model fitting lines (red line) for $DBSQ(OH)_2$, $DPSQ(OH)_2$ and $DHSQ(OH)_2$ neat film hole-only devices. The device structure is ITO/MoO_3 (8 nm)/SQ/MoO_3 (8 nm)/Al (100 nm). The thickness of the SQ neat layers and the mobility values are indicated.

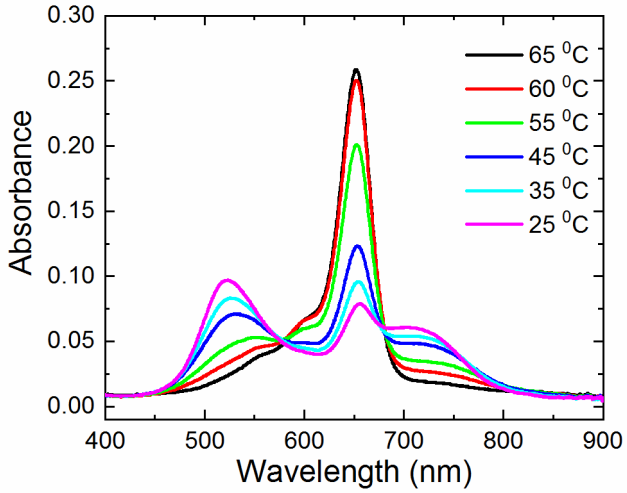

Figure A3 Absorption spectra of 80% DMSO:20% H_2O (by volume) for $DBSQ(OH)_2$, as a function of temperature. Two isosbestic points are found at 595 nm and 672 nm, confirming the interrelation between monomer and aggregate, with the double hump feature associated with squaraine aggregate.

Appendix B. STABILITY STUDY OF SQ-BASED OPV DEVICES

For real application of OPV, the stability of the devices is, without a doubt, an important factor. SQ materials are known for their stability against moisture and oxygen, allowing the active layer to be solution processed in ambient condition.[213] In this section, we test the stability and thermal behavior of our SQ molecules using thermogravimetric analysis (TGA) and differential scanning calorimetry (DSC). We also tested the stability of our solar cell devices with encapsulation.

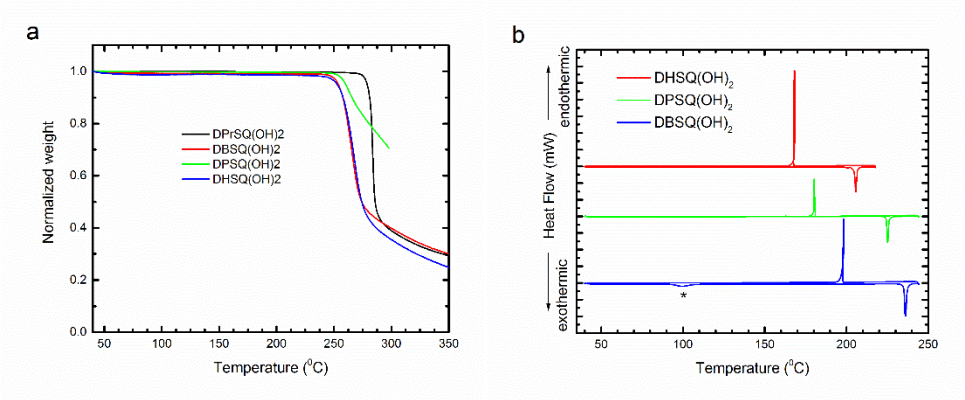

Figure B.1 **a**) Thermogravimetric analysis and **b**) differential scanning calorimetry results of SQ materials. The asterisks highlight a unique endothermic peak at 100 0C of $DBSQ(OH)_2$ powder solids.

For TGA results in Figure B.1a, the onset degradation temperature is measured to be 260-265 ^{0}C for $DBSQ(OH)_2$, $DPSQ(OH)_2$ and $DHSQ(OH)_2$. $DPrSQ(OH)_2$ exhibits a slightly higher onset degradation temperature of 283 ^{0}C. A higher onset degradation temperature would be more advantageous for device stability, yet the solubility limitation associated with $DPrSQ(OH)_2$ is a drawback.

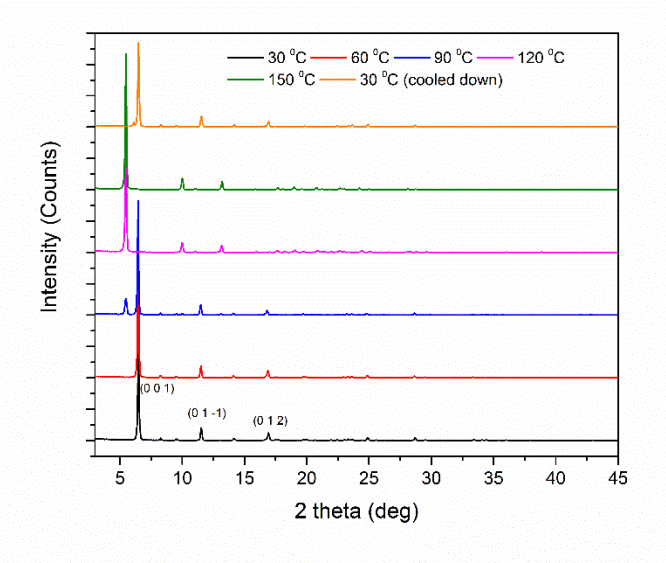

Figure B.2 *In-situ* high temperature X-ray diffraction (XRD) patterns of $DBSQ(OH)_2$ powders during a thermal ramping from 30 ^{0}C to 150 ^{0}C, then cooled back down to 30 ^{0}C.The powder XRD pattern at 30 ^{0}C matches well with the calculation based on the single crystal structure (data not shown). The crystal planes corresponding to different peaks are indicated in initial 30 ^{0}C films.

The melting and crystallization temperatures of SQ materials decrease as the side chain length is increased. The onset melting temperatures are 235 ^{0}C, 225 ^{0}C and 205 ^{0}C respectively, and the onset crystallization temperatures are 198 ^{0}C, 181 ^{0}C and 178 ^{0}C respectively for $DBSQ(OH)_2$, $DPSQ(OH)_2$ and $DHSQ(OH)_2$ respectively. We consider that as the side chain length is increased, the overall rigidity of the molecule is reduced. Thus, an enhanced flexibility towards diffusion of molecules in the BHJ films is expected when the molecule has longer side groups.

Another interesting observation is that there is an endothermic peak at ~ 100 ^{0}C for $DBSQ(OH)_2$ powders. This suggests that the solids may undergo a phase transition process that absorbs energy. Indeed, we also observed a peak shift in *in situ* high temperature XRD (Figure B.2). In the *in situ* X-ray diffractograms, $DBSQ(OH)_2$ powders exhibit three major

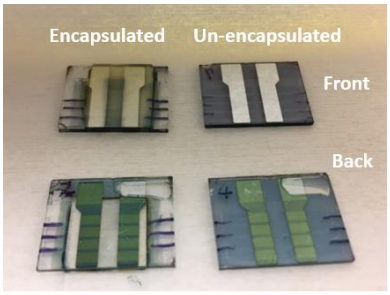

Figure B.3 A photo of organic photovoltaic devices with and without encapsulation by epoxy and coverslips. It is seen that for cells with encapsulation, the organic layer is dissolved when exposed to the epoxy, but the organic layer underneath the aluminum cathode is intact as demonstrated by the comparison of the back side of the devices.

peaks: $2\theta = 6.5^0$, $2\theta = 11.4^0$ and $2\theta = 14.3^0$, corresponding to (0 0 1), (0 1 $\bar{1}$) and (0 1 2) plane of the crystal structure. When temperature is raised to 90 ^{0}C, new diffraction peaks are emerging at $2\theta = 5.5^0$, $2\theta = 10.3^0$ and $2\theta = 13.3^0$. Although the corresponding crystal planes cannot be determined due to the lack of single crystal structure, the decreased 2θ values suggest the unit cell spacing is larger for this new polymorph. When temperature is raised to 120 ^{0}C, the entire material seems to have completed the phase transition. After the material is cooled down from 150 ^{0}C to room temperature, the DBSQ(OH)$_2$ powder has changed back to its original phase. These data suggest that DBSQ(OH)$_2$ can undergo a phase transition at 90-120 ^{0}C, which is fully consistent with the DSC data shown in Figure B.1.

To improve the stability of solar cell devices, we used a light curable epoxy and glass coverslips (Ossila Inc.) to encapsulate DBSQ(OH)$_2$:PC$_{71}$BM bulk heterojunction solar cells (see Figure B.3). This way, the solar materials are sealed from oxygen and moisture, which can react with organic materials as an oxidation reaction.[17] The device stabilities with and without encapsulation are shown in Figure B.3.

The detailed investigation steps are as follows. The fabrication and testing of solar cells are conducted in a nitrogen-filled glove box to minimize the material degradation due to the reaction with oxygen or moisture. After we have fabricated the devices, we test them immediately (i.e. "freshly made" in Table B.1). Then we encapsulate it with the epoxy and glass coverslips and test them right after encapsulation (i.e. "Encap" in Table B.1). For aging of the encapsulated devices, the cells are tested 1 day, 2 days and 2 weeks after being stored in ambient condition. For comparison, devices without encapsulation are also tested after 1 day of storage in ambient condition (the efficiency dropped so dramatically that the subsequent testing was determined to be unnecessary).

The freshly made devices have the highest averaged efficiency of 5.13% (note that it is slightly higher than previously obtained in Table 4.4 due to the use of a slightly lower active layer solution concentration of 12 mg mL^{-1}). We have noticed that the UV-curable epoxy used for encapsulation can actually dissolve the SQ:PCBM active layer films. Immediately after the solar cells are encapsulated, we see a drop in efficiency from 5.13% to 4.39% (see Table B.1). We noticed that the drop in efficiency only comes from the

Table B.1 The device stability investigation of $DBSQ(OH)_2$:$PC_{71}BM$ BHJ solar cells with encapsulation.

Conditions	Jsc, mA/cm^2	Voc, V	FF	PCE, %
Freshly made	10.47 (±0.31)	0.84 (±0.01)	0.58 (±0.01)	5.13 (±0.17)
Encap	10.05 (±0.19)	0.79 (±0.01)	0.55 (±0.01)	4.39 (±0.08)
1 day	9.97 (±0.20)	0.80 (±0.01)	0.54 (±0.01)	4.35 (±0.12)
2 days	9.77 (±0.23)	0.79 (±0.01)	0.54 (±0.01)	4.20 (±0.13)
2 weeks	9.67 (±0.27)	0.79 (±0.01)	0.54 (±0.01)	4.15 (±0.19)
1 day	3.77 (±0.64)	0.81 (±0.01)	0.31 (±0.02)	0.96 (±0.22)

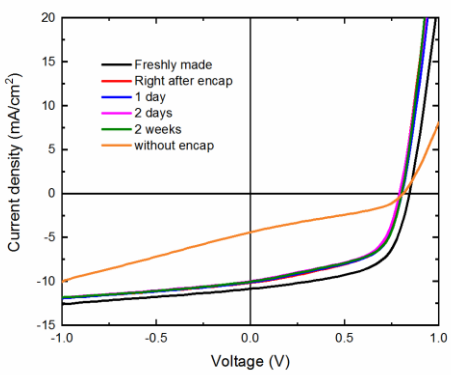

Figure B.4 Representative current-voltage curves of the DBSQ(OH)$_2$:PC$_{71}$BM BHJ devices aged for 2 weeks with and without encapsulation.

decreased short circuit current from 10.05 mA cm^{-2} to 9.67 mA cm^{-2}, while open circuit voltage and fill factor remains unchanged. A slower efficiency drop is expected as the devices age for a longer time. As a comparison, the un-encapsulated solar cells show dramatic deterioration in efficiency from 5.13% to 0.96% only after 1 day at ambient condition. The representative J-V curves after aging the devices are shown in Figure B.4.

In a short summary, we have investigated the stability of the SQ materials and SQ-based OPV devices. According to TGA results, the SQ materials are stable when heated to 260 ^{0}C in inert nitrogen environment (see Chapter 2 for experimental details). When exposed to air, the solar cell devices show dramatic degradation as shown in Figure B.4. Nevertheless, the solar cell devices show long-time stability after encapsulation, demonstrating that SQ materials have potentials for real world OPV applications.